Searching for Helium in the Extended Atmosphere of the Hot Jupiter WASP-48b

by

Katherine Bennett
Class of 2022

A thesis submitted to the
faculty of Wesleyan University
in partial fulfillment of the requirements for the
Degree of Master of Arts

Middletown, Connecticut   April, 2022

My dear Boys and Girls:

I am delighted to receive your letter and to know that you are studying the moon and eclipses...I cannot easily tell you about the moon at this distance, but if you can induce Mrs. Eaton to sew some wings on your shoulders so you can all fly up here, I will show you the moon through the telescope, and tell you all I know about it while you are looking.

—Frederick Slocum

First Director of Van Vleck Observatory

In response to a letter received from Mrs. Eaton's fifth grade class in Franklin, NC. Dated December 15, 1934.

Acknowledgements

I would like to first and foremost thank my advisor, Professor Seth Redfield, without whom this thesis would be just a few scattered thoughts. I am incredibly grateful for his mentorship and guidance along every step of the process. He taught me to become a true problem-solver, to plug along even if we do not have all the answers, and to always get excited when looking at plots. I could not have asked for a better mentor, and I hope we can continue to work together in the future.

Thank you to the Astronomy Department at Wesleyan University. Thank you for admitting me to this program and giving me the chance to become an astronomer. I am so lucky to have found such a supportive and welcoming community here, and I will dearly miss coming to work at the observatory every day. I would like to thank Professors Ed Moran, Roy Kilgard, Meredith Hughes, and Bill Herbst for always having their doors open and making the department feel like a family. I am deeply grateful to Stef Dinneen, who gets tasks accomplished faster than I would have thought possible. I also must thank Cheryl Hagner, who I am certain does an inordinate number of tasks behind the scenes every day to keep the graduate program running.

I am so glad that I went through this program with Miriam Eleazer. They made work feel like home, and I am forever grateful that we were able to share an office and work in person our second year together. I cannot express how much I will miss working in the observatory basement with them. Thank you to Megan Delamer and Manny Perez, who provided me with many calming words through my first year. Thank you Alaina Einsig, Sara Negussie, Anna Fehr, Seth Larner, Kyle McGregor, and countless others for helping us rebuild the observatory base-

Contents

Chapter 1

Exoplanets: The New Frontier

1.1   Beginnings: Exoplanetary Science Emerges

The notion that a multitude of other planets outside our own Solar System exist is not new. As far back as the fourth century B.C.E., the Greek philosopher Epicurus speculated that "there are infinite worlds both like and unlike this world of ours". Before his untimely imprisonment and execution as a heretic, Giordano Bruno wrote in *De l'infinito universo et mondi (On the Infinite Universe and Worlds)* in 1584, "There are countless suns and countless Earths all rotating around their suns in exactly the same way as the seven planets of our system."

Today, we know there is on average one or more planet for every star in the Milky Way galaxy (Cassan et al. 2012). The study of these extrasolar planets, or exoplanets, as they are more commonly known, has exploded in the last three decades. As of April 19, 2022, we know of 5014 confirmed exoplanets (courtesy of the NASA Exoplanet Archive[1]). The astronomical community is on the precipice of a new era of planetary discovery and characterization, with the goal of answering big questions such as "How common is Earth?" and "Is there life on other planets?". Answering these questions for the first time allows us to establish an understanding of the Earth's place, not only in the Solar System, but in

---

[1] https://exoplanetarchive.ipac.caltech.edu

the broader context of all planetary systems. For this reason, exoplanet science is poised to have profound implications in not just the astronomy community, but in fields as wide-ranging as geology, biology, and philosophy.

1.1.1 Hints of Exoplanets

The possible existence of exoplanets first transitioned from the realm of philosophical inquiries and science fiction writing to astronomical searches in the nineteenth century. One of the earliest claims of detections came from Jacob (1855), in which William Stephen Jacob stated that the orbital anomalies seen in the binary star system 70 Ophiuchi were likely due to a third "dark body" in the system. However, this was later refuted by Moulton (1899), who stated that such a three-body system would be unstable.

The first planet-hunting technique employed by Jacob (1855) was astrometry, the measure of the proper motion of stars and other bodies. If a planet is orbiting a host star, the common center of mass of the system will alter the star's orbital motions. This technique continued to be favored by exoplanet enthusiasts and led to several claims of planet detections in the mid-twentieth century (e.g., Reuyl & Holmberg 1943; Strand 1943; van de Kamp & Lippincott 1951), but all these were eventually discarded as illegitimate. The most famous example is that of Barnard's Star, which was found to have a planetary companion 1.6 times the mass of Jupiter (van de Kamp 1963), but it was later determined that this detection was in fact simply a result of systematic error of the telescope used (Gatewood & Eichhorn 1973; Hershey 1973)[2].

While the observational astronomy community was struggling to find true signatures of exoplanets, a theoretical paper was published during this period that

---

[2]This realization was made using data collected right here at the Van Vleck Observatory.

predicted what would come to be the two most common detection techniques: the radial velocity and transit methods. Struve (1952) was the first to postulate that Jupiter-mass exoplanets need not be at a distance of one or more astronomical units (au) from their host stars. Instead, it is perfectly possible that, similar to stars in close binary systems, there exist Jupiter-mass planets at distances of 0.02 au. These close-in exoplanets would then be detectable using Doppler spectroscopy (the radial velocity technique) or by measuring the loss of stellar light during eclipses (the transit technique).

Subsequent to this paper, the radial velocity technique was the first to gain traction in the observational community. This technique is similar to astrometry in that it relies on measuring the motion of the star around a common center of mass. Unlike astrometry, however, which measures the motion of stars in the plane of the sky (proper motion), the radial velocity technique takes into account radial motion toward and away from the observer, which is determined by measuring periodic variations in Doppler spectroscopy. By finding known atomic absorption lines in stellar spectra and comparing their observed wavelengths to their rest wavelengths (taken from laboratory data), the star's radial velocity can be determined. A sinosoidal fluctuation in radial velocity over time suggests that a star and its planet(s) are orbiting about a common center of mass.

Prior to the first confirmed detections, there were postulated exoplanet discoveries into the 1980s and early 1990s using the radial velocity technique. These included the radial velocity variations seen in γ Cephei (Campbell et al. 1988), which hinted at a substellar companion orbiting at approximately 2 au, but it was unclear whether this companion was likely to be a brown dwarf or planet. It was not until 2002 that it was confirmed that the companion is likely a giant planet with a projected mass of about 1.25 M_J (Cochran et al. 2002). Another "probable

brown dwarf" was detected around the solar-type star HD 114762 (Latham et al. 1989) and indeed, it was later confirmed to be a brown dwarf and not an exoplanet using data from the *Gaia* space observatory (Kiefer 2019).

Besides radial velocity searches, pulsar timing became the next unlikely technique of exoplanetary discovery. Pulsars, which are rotating neutron stars, display pulses of radio waves at incredibly precise intervals. Any irregularities in these intervals suggest the pulsar has some motion to it. If a pulsar and its planet are orbiting around a common center of mass, this motion (and thus the parameters of the planetary system) can be derived using pulsar timing studies. This is a promising technique because it can detect planets much smaller than can be found using the radial velocity, astrometric, or transit techniques, although the scarcity of pulsar planets detected suggests pulsars may not be prime targets for exoplanet studies (Miller & Hamilton 2001). Indeed, prior to the 1990s, few astronomers expected to find planets orbiting stars outside the main sequence. Still, this technique first led to the tentative discovery of a planet around the pulsar PSR1829-10 (Bailes et al. 1991), but this claim was redacted only a year later (Lyne & Bailes 1992) when it was realized that the signal was due to an artifact that arose from improper barycentric corrections. It was in this same year, however, that the first confirmed detection of an exoplanet was published, and this forever changed the future of exoplanet science.

1.1.2 The First Confirmed Exoplanet Discoveries

However surprising we may find it to this day, the first planet discovered outside our Solar System was not orbiting another Sun-like star, or even a main sequence star. It was orbiting a pulsar. Wolszczan & Frail (1992) found that

the timing variations of the millisecond pulsar PSR1257+12 were due not to a stellar companion, but to two or more planets. These were interpreted to be most likely a "second generation" of planets that formed around the evolved star after its supernova explosion. The notion that planets could be detected around dead stars was novel, and made many scientists realize that the story of planetary formation and evolution was much more diverse and complex than previously thought.

Just a few years later, in 1995, an approximately 0.5 M_J planet was discovered orbiting at 0.05 au around the Sun-like star 51-Pegasi (Mayor & Queloz 1995). This was the first planet to be detected and confirmed using the radial velocity technique after more than a decade of searching, and it was the first exoplanet detected orbiting a main sequence star. Still, like the pulsar planet detection in 1992, this discovery offered its own surprise. At the time, gas giants were not expected to be in such close proximity to their host stars, and so this revelation signified that our understanding of planetary formation was by no means complete. Thus, the study of "hot Jupiters" began.

For the next five years, the radial velocity technique dominated exoplanet discoveries. However, in 2000 the transit method was used for the first time to confirm the radial velocity detection of HD 209458b (Charbonneau et al. 2000). This technique measures the decrease of stellar flux that occurs when a planet transits in front of its host star, as shown in Figure 1.1. While transit photometry had in the past been used to study everything from Venus to stellar binaries, the introduction of this technique to exoplanet detection was important because by coupling radial velocity and transit observations, a planet's radius could be estimated in addition to its mass, allowing for constraints on planetary surface gravity and density (Charbonneau et al. 2000).
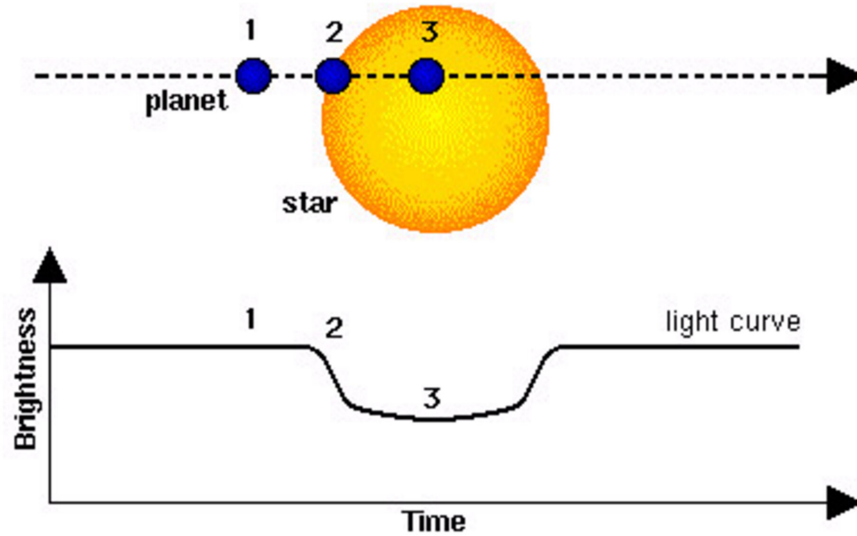
Figure 1.1: The transit technique for discovering exoplanets. As a planet transits between Earth and its host star, the amount of stellar flux received decreases. Courtesy of ESA[3], figure adapted from Deeg & Alonso (2018).

The relative decrease in flux seen when a planet passes between Earth and its host star, known as transit depth (δ), is due to the ratio of the stellar and planetary areas and is given by

$$\delta = \left(\frac{R_P}{R_\star} \right)^2 , \tag{1.1}$$

where $R_\star$ is the radius of the host star and R_P is the radius of the exoplanet. Typically, $R_P << R_\star$ and therefore $\delta << 1$. Large gas giants cause a transit depth of about 0.01, while smaller rocky planets have a transit depth of only approximately 0.0001. Because of this larger threshold of detection for gas giants, these planets are more easily detected and characterized. Furthermore, the shorter

---

[3]https://www.esa.int/Science_Exploration/Space_Science/How_to_find_an_extrasolar_planet

the planet's period, the more frequently transits occur, meaning this field is biased toward detecting larger, close-in planets (i.e., hot Jupiters). Other factors also bias findings, most notably the fact that the planetary system must be aligned close to edge-on in order to have the appropriate viewing geometry to detect transits. Assuming a random inclination, the probability of a close-in hot Jupiter transiting along our line of sight is approximately 10% (Seager & Sasselov 2000). In spite of these biases, astronomers have embraced the partnership between the transit and radial velocity techniques, and these two detection methods dominate the field today.

1.1.3 Exoplanet Science Today

Since 1992, exoplanet detections have increased exponentially, as shown in Figure 1.2. In 2000, eight years after the first confirmed detections, only 11 candidates were known (Charbonneau et al. 2000). Today, 5014 planets have been found. Though the radial velocity method was the most common technique used early on, it was surpassed by the transit technique in 2014 following a large data release by NASA's *Kepler* space mission. By 2018, 78% of detections had been made using the transit method (Deeg & Alonso 2018), and this trend continues today. This can be seen in Figure 1.2. The reason for this trend is partly due to dedicated space missions such as *Kepler*, launched in 2009, and *Transiting Exoplanet Survey Satellite (TESS)*, launched in 2018, and partly due to ground-based surveys. These include the Wide Angle Search for Planets (WASP) as well as the Hungarian-made Automated Telescope Network (HATNet). These searches have been quite successful, with hundreds of exoplanets discovered.
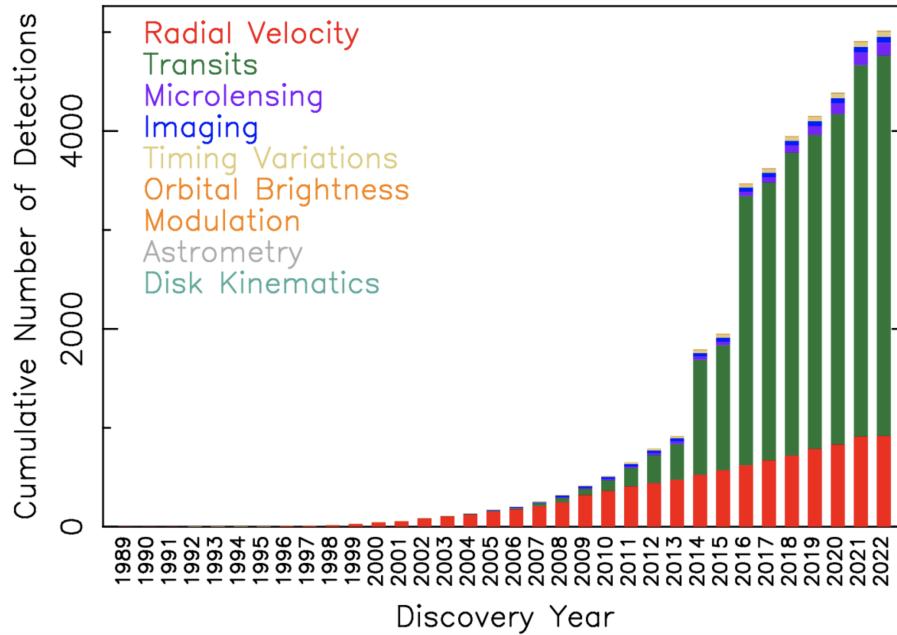
Figure 1.2: Cumulative exoplanet detections per year delineated by detection methods. The number of detections has grown exponentially, with the vast majority being detected using the transit and radial velocity techniques. Courtesy of NASA Exoplanet Archive.

It is critical to keep in mind that every detection method is biased in some way. This is demonstrated by the mass-period relationship of confirmed exoplanets, seen in Figure 1.3. Both the transit technique and the radial velocity method are biased toward finding large, short period planets, and it is for this reason that exoplanet science to date has largely been guided by the study of hot Jupiters. These techniques have also uncovered a so-called "Neptune desert," or an under-representation of detected exoplanets between about 2 $R_\oplus$ and 8 $R_\oplus$ (Zhu & Dong 2021), and this has important implications in our understanding of planetary evolution. This will be discussed further in Section 1.3.
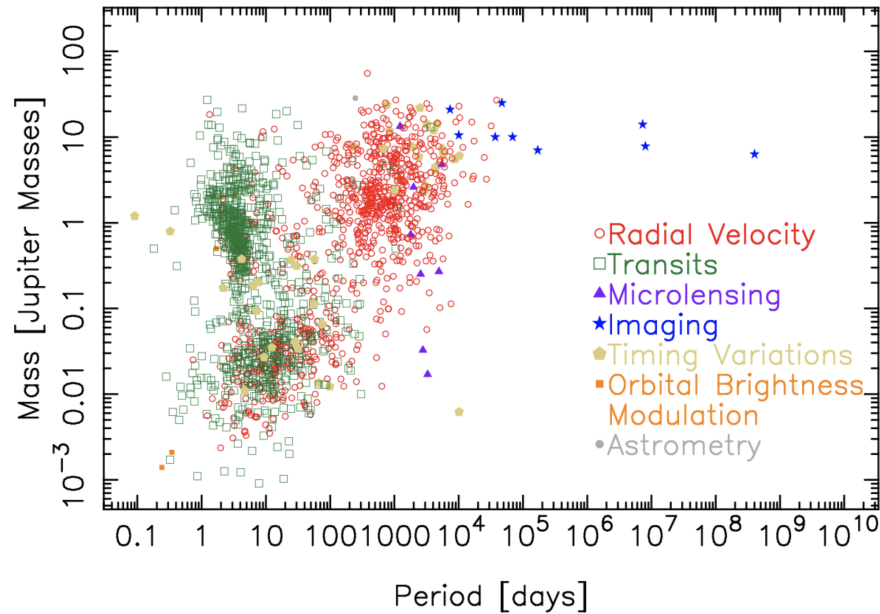
Figure 1.3: Mass-period relationship of confirmed exoplanets by detection method. Most detections have been of close-in, high-mass exoplanets, although the transit technique is more sensitive to lower mass planets than the radial velocity technique. Courtesy of NASA Exoplanet Archive.

1.2 Beyond Detections: Transmission Spectroscopy and Atmospheric Characterization

Even as exoplanet detections were still in their nascent phase, astronomers were already predicting how to glean more information about exoplanets. The first logical mechanism of characterization was to couple information about the radius (through the transit method) and the mass (through the radial velocity technique). This mass-radius relation would then be plotted on a figure such as Figure 1.4, which depicts mass-radius curves based on internal structure models of planets with uniform composition. This allows for some constraint on the structure of observed exoplanets; for example, Kepler-10b lies between the iron and magnesium silicate curves, suggesting that its internal structure is composed
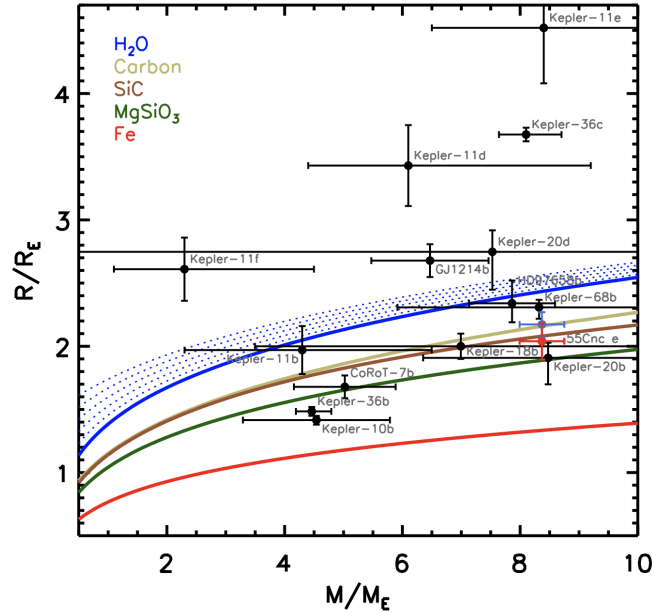
Figure 1.4: Mass versus radius relations for observed exoplanets plotted with theoretical mass-radius curves based on various internal structure models. This allows researchers to gain some insight into the structure of an exoplanet from only its mass and radius. Figure 1 from Madhusudhan & Redfield (2015).

of some combination of metal and rock. However, there is still a large amount of degeneracy and uncertainty surrounding structure when only the mass and radius of the planet are known.

In pursuing a more robust way to characterize exoplanets, astronomers focus on the detection of the atoms and molecules that make up the exoplanet's atmosphere using a technique called transmission spectroscopy. When a planet transits its star, some of the starlight filters through the planet's atmosphere, seen in Figure 1.5. At certain wavelengths, this light will be absorbed by the atoms in the planet's atmosphere, enlarging the planet's effective radius as it transits the star. This means that transit depth is in reality wavelength-dependent. One can measure the spectrum of the star while the planet is transiting and compare that to the stellar spectrum when the planet is not transiting. If there is an
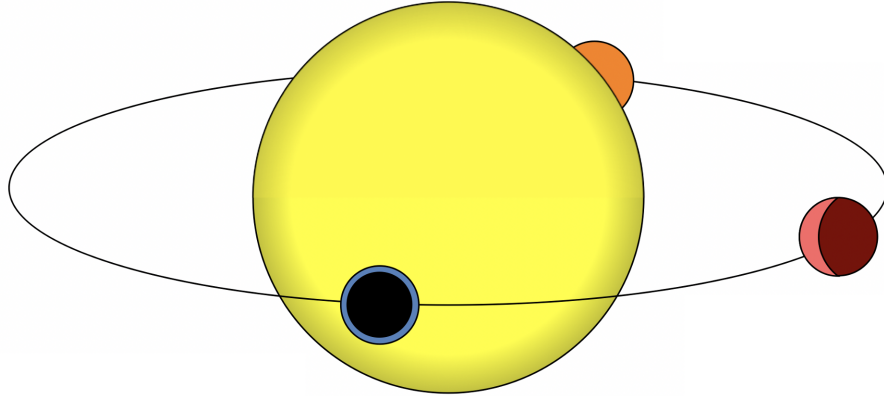
Figure 1.5: Transit and secondary eclipse of an exoplanet transiting host star. As the planet transits the star, some of the starlight passes through the planetary atmosphere (depicted as the blue rim around the planet). Adapted from Seager & Deming (2010).

increase in absorption line depth during the in-transit spectra, this suggests the atom or molecule responsible for that absorption line is present in the planet's atmosphere. The transmission spectrum, the difference between the in-transit and out-of-transit spectra, is defined as:

$$\frac{F_{\text{in}} - F_{\text{out}}}{F_{\text{out}}} = \frac{F_{\text{in}}}{F_{\text{out}}} - 1, \tag{1.2}$$

where F_{in} and F_{out} are the in-transit flux and out-of-transit flux, respectively. In this definition, absorption is negative and emission is positive.

Early postulations of this technique include Schneider (1994), which investigated the feasibility of detecting optical O_2 lines and presciently noted that this could be of importance for astrobiology studies. Rauer et al. (2000) searched for absorption features in the infrared spectrum of 51 Peg b, the first exoplanet detected around a main sequence star, but did not detect any significant difference between the in-transit and out-of-transit spectra. Even Charbonneau et al. (2000), in the first published paper on a transit detection, predicted that atmo-

spheric features could be observed while a planet transited its host star.

The seminal work by Seager & Sasselov (2000) was the first to quantify and predict specific spectral features that could be detectable in hot Jupiters. The predicted transmission spectra were based on models of planetary spectra derived from Seager et al. (2000), and the results predicted observable features from alkali metals (particularly the Na I and K I resonance doublets) as well as the 10830 Å helium triplet, which is the focus of this work and will be discussed in detail in Section 1.4. Seager & Sasselov (2000) predicted that transmission spectroscopy can constrain the column density, temperature, and pressure of the planet's upper atmosphere, as well as the cloud top depth, which would further our understanding of atmospheric models. Other early theoretical transmission spectroscopy papers include Hubbard et al. (2001). This paper attempted to expand on the work done by Seager & Sasselov (2000) to predict the wavelength-dependent changes in the radius of a hot Jupiter, and found that in the infrared regime, which is dominated by H_2O opacity, the radius change is on the order of 1%. Brown (2001) predicted expected features on HD 209458b and anticipated that clouds would be the most dominant factor in inhibiting absorption features. This paper noted the need for high-resolution spectrographs (with at least $R = 10,000$) in order to resolve these features.

Indeed, the first observed absorption feature attributable to a planetary atmosphere was of Na I in HD 209458b (Charbonneau et al. 2002). Previous attempts had been made to identify atoms in this planet's optical spectrum using ground-based telescopes without success (e.g., Bundy & Marcy 2000; Moutou et al. 2001), likely due to insufficient precision; these studies could only resolve differences between in-transit and out-of-transit spectra of about 1% or greater. Charbonneau et al. (2002) used data from the *Hubble Space Telescope's (HST)* Space Tele-

scope Imaging Spectrograph (STIS), and notes that though Na I was detected, its measured absorption was lower than predicted. This could be due to atomic Na I reacting with other atmospheric constituents to form Na-based molecules, photoionization of Na I, a lower Na I abundance than predicted, or signal attenuation due to the presence of clouds. Thus, this paper offered the first attempt to constrain atmospheric characteristics of an exoplanet, and the field would only explode from here. Controversies, however, abound to this day. A recent paper by Casasayas-Barris et al. (2021b) revealed that the Na I feature in HD 209458b could be explained by changes in the stellar Na I line and is not in fact a planetary signal. This demonstrates how conclusions from transmission spectroscopy can so often be inconclusive at worst and tenuous at best.

While *HST*'s STIS instrument avoided contamination from Earth's telluric lines in the study by Charbonneau et al. (2002), its medium resolution hindered its detection threshold. In 2008, Redfield et al. (2008) was the first paper to report the detection of planetary absorption of Na I from the ground using the High Resolution Spectrograph (HRS) of the Hobby-Eberly Telescope. This opened the floodgates of a new era of exoplanet atmospheric characterization. Today, ground-based observations are often coupled with space-based observations (typically using *HST*), and this will continue with the *James Webb Space Telescope (JWST)*. Many *JWST* observations are planned based on information gained from ground-based and HST studies of well-known exoplanets, including HD 189733b (Gasman et al. 2022) and 55 Cnc e (Zilinskas et al. 2020). Today, astronomers are glimpsing the environments of exoplanets and gaining meaningful insight into atmospheric structure, wind patterns, evolution, and more.

1.3 Atmospheric Mass Loss and Planetary Evolution

An intriguing topic that has arisen and can be probed using observational transmission spectroscopy is the question of atmospheric escape for close-in exoplanets. Indeed, as soon as the first hot Jupiter (51 Peg b) was detected around a main sequence star in 1995, astronomers began postulating whether the planet was "on its deathbed, or merely tanning" (Burrows & Lunine 1995). Its proximity to its host star meant that the gas giant was highly irradiated, which suggested it was undergoing atmospheric escape. Possible loss mechanisms were outlined in this very first paper about atmospheric loss and include Roche lobe overflow, classical Jeans evaporation, and energetic atomic/ionic escape due to stellar UV radiation (Burrows & Lunine 1995). The lattermost mechanism was deemed the most promising, and most atmospheric escape research to date has been focused on high-energy stellar flux.

1.3.1 Implications of Atmospheric Escape

High-energy radiation in the UV and X-ray regime causes the upper layers of a close-in exoplanet's atmosphere to heat up on the order of 5,000–10,000 K, allowing some of the gas in these upper layers to escape (Owen 2019). This phenomenon provides a framework for planetary composition and evolution. Early on, astronomers dismissed atmospheric escape as a dominant force in evolution for hot Jupiters, demonstrating that these planets are stable even at close-in orbits (e.g., Guillot et al. 1996). However, Lecavelier Des Etangs (2007) argued that over a planet's lifetime, it receives enough high-energy radiation to account for a signif-

icant fraction of its gravitational potential energy, suggesting that this mechanism of atmospheric escape does in fact affect mass loss and bulk composition over a planet's lifespan. The need to quantify this mass loss became apparent as more super-Earths and sub-Neptunes were discovered, as the density ranges found for these planets allow for a degeneracy in planetary interior and atmospheric modeling. For example, the density of the super-Earth GJ 1214b could be explained assuming a H-He primordial atmosphere, outgassing of rocky material, or sublimation of ice (Rogers & Seager 2010). This ambiguity in atmospheric composition means that the interior structure also cannot be constrained, further limiting the characterization of exoplanets in this mass regime. Understanding the mechanism of mass loss due to high-energy stellar irradiation across exoplanet types can help place constraints on the possible atmospheric composition of these exoplanets. This, in turn, will play a crucial role in determining whether these planets are viable to host life. For this reason, the study of extended atmospheres has a clear astrobiological importance, allowing us to narrow our target list and deepen our understanding of habitability.

Besides improving planetary characterization, quantifying mass loss provides insight into planetary evolution. The bulk of mass loss is thought to occur early on in a planet's lifetime, when a young star is highly active and thus emitting large amounts of high-energy radiation (Sanz-Forcada et al. 2011). By modeling how this plays out over a planet's lifetime, astronomers can determine whether mass loss contributes significantly to how a planet evolves. By calculating the evolutionary tracks of hot Jupiters, Hubbard et al. (2007) showed that these gas giants were stable against atmospheric mass loss and are not likely remnants of even more massive bodies. While atmospheric escape is no longer considered a driving evolutionary factor for hot Jupiters, studies of mass loss in hot Jupiters

has laid the groundwork for studying smaller, sub-Neptune planets.

For these planets, atmospheric escape is thought to be an important contributor in how the planet evolves with its star and provides a possible explanation for the so-called "evaporation valley" or "Neptune desert". This is a phenomenon that has been described observationally (e.g., West et al. 2019; see Figure 1.6) and is broadly defined as a paucity of intermediate-mass planets with periods of 2–4 days (Mazeh et al. 2016). Owen & Lai (2018) argued that the lower boundary (associated with lower mass planets) of this triangular desert is attributable to photoevaporation due to high levels of irradiation. Note that this phenomenon cannot necessarily explain the upper boundary, as planets larger than 0.5 M_J are stable against atmospheric escape and mass loss. Instead, the upper boundary is likely due to tidal circularization of large close-in exoplanets (Owen & Lai 2018).
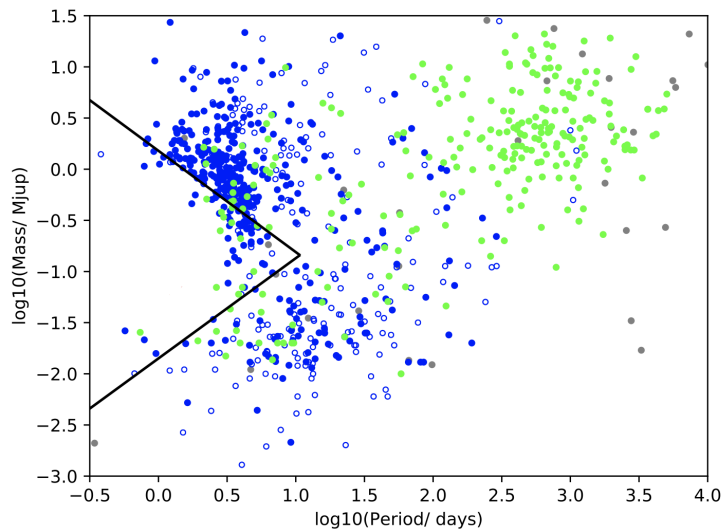
Figure 1.6: Mass vs. period distribution of detected exoplanets with measured mass, as of 2019. The edge of the "Neptune desert" is illustrated by the solid black line. Within this "desert," there is a dearth of discovered exoplanets. Planets discovered using the transit method are shown in blue, and planets detected using the radial velocity method are shown in green. Planets shown in grey were detected with other methods. Adapted from Figure 7 in West et al. (2019).

This dearth of intermediate-mass planets has also been described theoretically (e.g., Lopez & Fortney 2013; Owen & Wu 2013) as an "evaporation valley" of planets around 2 $R_\oplus$ seen when computing evolutionary tracks for planets of varying orbital distances and masses experiencing atmospheric escape (Owen & Wu 2013). This "evaporation valley" can be seen in Figure 1.7, in which planets at a certain minimum radius and separation threshold evolve right over the "evaporation valley", demonstrating that these planets initially had hydrogen and helium atmospheres but experienced enough atmospheric escape to lose them entirely. This further supports the hypothesis that atmospheric escape drives bulk mass loss of intermediate-size planets.
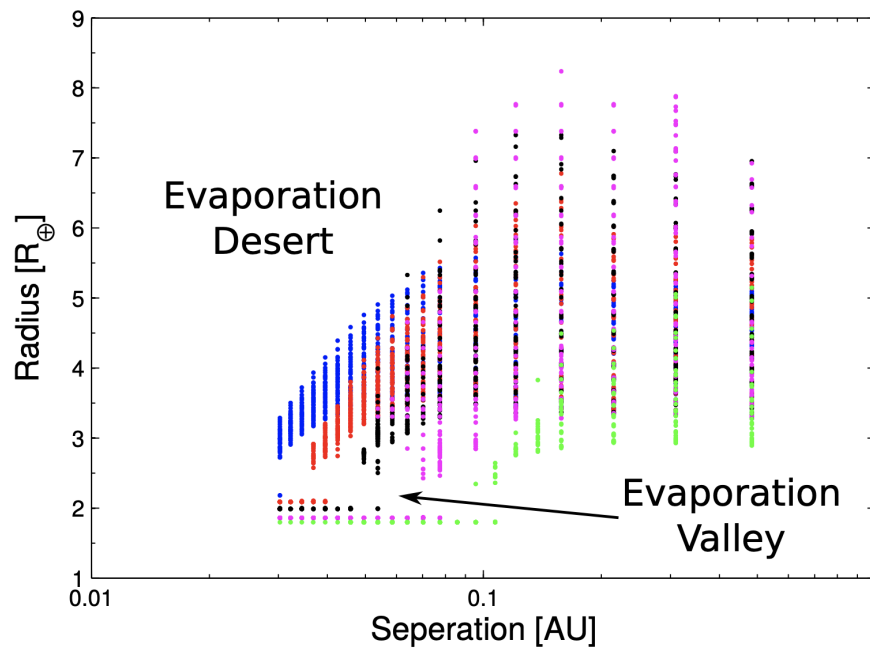
Figure 1.7: Radius versus orbital separation of synthetic planetary populations. Evolutionary tracks of 6.5 to 15 $M_\oplus$ exoplanets at varying semimajor axes experiencing atmospheric escape are shown. The existence of the "evaporation valley" supports the hypothesis that atmospheric escape drives evolution in intermediate-mass planets. Adapted from Figure 8 in Owen & Wu (2013).

1.3.2   Markers and Observations of Atmospheric Escape

The technique of transmission spectroscopy, detailed in Section 1.2, is used to observe indicators of atmospheric escape. The first such indicator used was the Lyman-α line of hydrogen. It was first detected in the atmosphere of HD 209458b (Vidal-Madjar et al. 2003), further adding to the long list of exoplanet research milestones reached by studying this planet. Researchers detected an absorption depth in the Ly-α line of approximately 15%, which was much larger than the optical transit depth of 1.5% found by Charbonneau et al. (2000). By comparing with models, it was determined that this absorption takes place at large radii beyond the planet's Roche limit, signifying that the absorption feature represents escaping hydrogen atoms (Vidal-Madjar et al. 2003).

While Ly-α was the first detection, to date only a handful of detections using this marker have been made (e.g, Lecavelier des Etangs et al. 2012; Ehrenreich et al. 2012; Kulow et al. 2014). Though the line has a large cross section (Owen 2019), the lack of ease of detection is attributable to the fact that the line is in the ultraviolet regime (at 1215 Å) and thus cannot be observed using high-resolution ground-based facilities. The only instrument capable of making Ly-α observations is STIS onboard *HST*. In addition, the core of the line is altered by heavy absorption by the interstellar medium (ISM) and Earth's own geocoronal emission (e.g., Vidal-Madjar et al. 2003). This means that this line can only be used to study close stars with large relative motion (Orell-Miquel et al. 2022), where information can be gained from looking at the wings of the line.

In addition to Ly-α, the Hα line of the Balmer series has also been observed in a handful of exoplanetary atmospheres (e.g., Jensen et al. 2012; Yan & Henning 2018). Jensen et al. (2012) argued that obtaining both Ly-α and Hα measurements

would provide further constraints on the density and temperature of the extended atmosphere. However, there has been speculation that some Hα signatures could be due to stellar activity and not planetary absorption. For example, Barnes et al. (2016) showed that in HD 189733b, Hα absorption does not show any velocity gradient in the stellar rest frame as the planet transits. Assuming the absorption is planetary in nature, this is surprising, because the motion of the planet across the star should affect the wavelength at which the line is observed. This suggests that the absorption is due the planet transiting over varying areas of stellar activity and not due to Hα in the planetary atmosphere. However, Cauley et al. (2017) argued against this hypothesis, showing no relationship between stellar activity level and Hα absorption features. Still, this raised the issue of the sensitivity of hydrogen features to stellar activity. Some astronomers began to turn to a new marker of atmospheric escape, metastable helium, that could circumvent this issue.

1.4   Metastable Helium as a Marker for an Extended Atmosphere

Metastable helium is an attractive tracer of extended atmospheres because it is less susceptible to stellar activity and is not as affected by absorption by the ISM (Oklopčić & Hirata 2018). In addition, a huge advantage of using this line as a marker over Ly-α is that it is in the infrared regime (10830 Å in air wavelengths or 10833 Å in vacuum), meaning it can be observed using ground-based telescopes.

This helium feature was predicted to be a reliable absorption signature early on in the days of theoretical transmission spectroscopy, prior to any observations taking place (Seager & Sasselov 2000). However, it was not actually observed in

an exoplanetary atmosphere for another 18 years. Excess helium absorption was detected for the first time in WASP-107b using narrowband photometry with the Wide Field Camera 3 (WFC3) onboard *HST* (Spake et al. 2018). This detection was quickly confirmed using high-resolution ground-based spectroscopy with the CARMENES spectrograph of the 3.5 m telescope at Calar Alto (Allart et al. 2019). Since then, the number of helium detections has exploded (e.g., Nortmann et al. 2018; Allart et al. 2018; Salz et al. 2018; Ninan et al. 2020; Paragas et al. 2021), with many non-detections (both expected and unexpected) being published as well (e.g., Kasper et al. 2020; Krishnamurthy et al. 2021; Vissapragada et al. 2021). Understanding why excess helium absorption is seen in some systems but not others will be a key question to answer as more and more observations are made.

1.4.1   The Physics of Metastable Helium

The 10833 Å helium line is a good indicator of atmospheric escape because it is a probe of the upper layers (the thermosphere) of an exoplanetary atmosphere, where the atmosphere is being heated by high-energy stellar radiation (Owen 2019). The mechanism works as follows: EUV flux shorter than 504 Å ionizes neutral helium atoms in the upper atmosphere of a close-in exoplanet (Seager & Sasselov 2000). The free electrons that arise from this ionization (as well as the ionization of hydrogen by photons shorter than 912 Å) then cause many collisions with other particles, which heats the atmosphere, causing it to "inflate" and partially escape (Sanz-Forcada et al. 2011). In addition, as the ionized He II recombines to He I, this recombination is stopped at the 2^3S triplet state without decaying all the way to the ground state, from which it is almost entirely radia-

tively decoupled (Seager & Sasselov 2000). This is the reason that this helium line is labeled "metastable".

Note that the singlet and triplet neutral states represent the relative orientation of the spin of the electrons (Oklopčić & Hirata 2018). The electrons' spin is parallel in the triplet state or anti-parallel in the singlet state. The 2^3S triplet state is populated by recombination, as described above, as well through collisional excitations from the 1^1S singlet state (Oklopčić & Hirata 2018). Continued radiation from the star then scatters off the 2^3S neutral helium state, causing it to undergo resonance scattering to the 2^3P state (Oklopčić & Hirata 2018), as shown with the red arrow in Figure 1.8. This is the transition resulting in the metastable helium absorption.
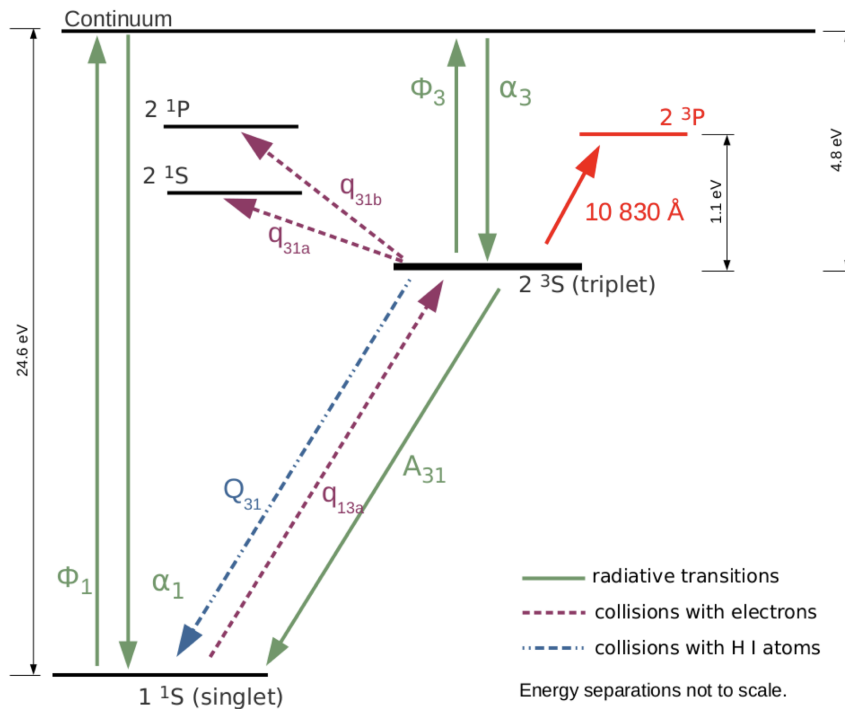
Figure 1.8: Atomic transitions of neutral helium. EUV flux ionizes helium, which then recombines to the 2^3S state. This state does not quickly radiatively decay back to the ground state, but instead can undergo resonance scattering to the 2^3P state, creating the 10830 Å absorption line. Figure 1 from Oklopčić & Hirata (2018).

The helium feature is actually a triplet, because the upper level of the transition, 2^3P, is split into three levels due to fine structure Oklopčić et al. (2020). These three levels correspond to vacuum wavelengths 10832.07, 10833.22, and 10833.31 Å (see Section 3.1). The 10832.07 Å component is considered the "blue component" and is easily spectrally resolved from the 10833.22 and and 10833.31 Å components using most high-resolution spectrographs. The 10833.22 and and 10833.31 Å components are typically indistinguishable, and we refer to these as the "red component". The blue feature is typically much smaller than the red component in a transmission spectrum (see Figure 4.6) and is often not detected.

Because the planetary absorption signal we see in the transmission spectrum is dependent on the amount of helium in the 2^3S state, and there is a correlation between EUV flux and the population of this state (Oklopčić 2019), we would expect that the higher the EUV flux of a host star, the stronger the helium signal. In addition, there is another regime of the stellar spectrum thought to contribute to the population of helium atoms in the metastable state. The mid-ultraviolet (mid-UV) photoionizes the metastable state at 2600 Å, and so the higher the stellar mid-UV flux, the lower the 10833 Å absorption line (Oklopčić 2019). At first, this may seem counterintuitive: to maximize the He I absorption signal, we must have a star with low mid-UV flux but high EUV flux.

To understand why this is so, we must recognize that mid-UV flux is due to stellar effective temperature, and thus decreases with cooler stars according to the Planck function. On the other hand, EUV flux is thought to be due to stellar activity in the corona (Oklopčić 2019), which does not function as a blackbody. EUV flux, therefore, cannot simply be determined using the Planck function but must be determined directly through observations or indirectly through models or correlation measures. In addition, stellar type and age likely play a role in

the amount of stellar activity and EUV flux, so these factors must be taken into account. Therefore, it is possible to have a cool star with low mid-UV flux that simultaneously emits high amounts of EUV radiation, particularly if the star is young and is showing high amounts of activity. This issue of EUV flux and correlation of helium absorption with stellar parameters will be further explored in Chapter 5.

1.5 WASP-48b and its Host Star

In this thesis, we search for absorption in the 10833 Å helium line in the atmosphere of the planet WASP-48b and attempt to understand our results in the broader context of all the helium detections and nondetections to date. WASP-48b is a hot Jupiter discovered in 2011 as part of the WASP consortium, which was established with the goal of discovering as many exoplanets of varying orbital distances and compositions as possible in order to place constraints on exoplanetary models (Enoch et al. 2011).

The star itself is an F-type, slightly evolved star (Enoch et al. 2011). Stellar parameters are given in Table 1.1. In the planetary discovery paper, the transit technique (using a photometric light curve) and the radial velocity technique (using spectroscopic analyses) were used to calculate planetary and stellar parameters using a Markov Chain Monte Carlo (MCMC) code (Enoch et al. 2011). The MCMC results found the star to be larger than expected for the given mass, suggesting the star was not on the main sequence. When a main-sequence constraint was placed on the MCMC code, the results did not match the spectroscopic and photometric data as well, and so the constraint was dropped. Furthermore, no lithium or Ca II H and K lines were detected in the spectrum, supporting the idea

Parameter	Value
Distance (pc)	460 ± 5
Radius ($R_\odot$)	1.75 ± 0.09
Mass ($M_\odot$)	1.19 ± 0.05
T_{eff} (K)	5920 ± 150
Age (Gyr)	$7.9^{+2.0}_{-1.6}$
Spectral Type	F
V magnitude	11.72 ± 0.14
$\log g_\odot$ (cm s^{-2})	4.03 ± 0.04
[Fe/H]	-0.12 ± 0.12
$v \sin i$ (km s^{-1})	12.2 ± 0.7

Table 1.1: Stellar Parameters of WASP-48 from Enoch et al. (2011).

that the star is several gigayears old (Enoch et al. 2011). With the resulting values for density, effective temperature, and metallicity from the MCMC analysis, WASP-48 was found to be $7.9^{+2.0}_{-1.6}$ Gyr old by applying this data to the Padova isochrone fitting technique (Girardi et al. 2002), corroborating the spectroscopic data.

Interestingly, when using gyrochronology to infer the stellar age from its rotation rate ($v \sin i \sim 12.2$ km s^{-1}), the star is predicted to be only $0.6^{+0.4}_{-0.2}$ Gyr old, suggesting that it is rapidly rotating for a star of its age. This is thought to possibly be attributable to its close-in exoplanet, which may have "spun up" the star's rotation rate as the planetary orbital period synchronizes with the stellar rotational period (Enoch et al. 2011). An increased rotation rate is suggestive of a higher level of stellar activity, which in turn is associated with higher levels of EUV flux (Ribas et al. 2005). Therefore, though the star is old (which typically means stellar activity is lower), its higher rotation rate may suggest larger-than-expected stellar activity rates, and thus higher EUV flux and helium absorption. To the best of our knowledge, this is only the second time a star off the main sequence has been targeted in the metastable helium search. The first was for WASP-12b

(Kriedberg & Oklopčić 2018), in which helium was not detected. Therefore, our results will provide interesting constraints on how atmospheric escape plays out over the course of a star's lifetime.

The planet itself is an inflated hot Jupiter with a period of 2.14 days (Enoch et al. 2011), making it a prime target for transit and transmission spectroscopy studies. Planetary parameters are shown in Table 1.2. As stated above, in the discovery paper, both spectroscopic and photometric measurements were applied to an MCMC code to derive these planetary parameters, which were then refined using data collected by the Kuiper Telescope (in multiple photometric bands) at the Steward Observatory (Turner et al. 2016). These authors were also the first to search for wavelength dependencies in the transit depths across all the photometric bands used (which ranged from the near-UV to optical). They found a constant transit depth for WASP-48b, suggesting that a cloud deck could exist in its atmosphere that blocks spectral signatures.

Murgas et al. (2017) was the first to examine a true spectrum of WASP-48b using the OSIRIS spectrograph of the Gran Telescopio Canarias. These authors also found a flat optical spectrum, which, unlike Turner et al. (2016), they believe agrees with a model of a cloudless atmosphere with TiO and VO, although they were not able to confirm the presence of these molecules due to their broad profiles and low amplitudes. This is important because the presence of TiO in an exoplanet atmosphere is thought to drive atmospheric temperature inversions (Seager & Sasselov 1998). In turn, temperature inversions may be more likely to occur in planets orbiting stars with lower stellar activity (and UV flux), because the high-energy flux can destroy molecules such as TiO responsible for these inversions (Knutson et al. 2010). This means that an absence of a temperature inversion is related to larger amounts of high-energy radiation, which we know to be correlated

Parameter	Value
Radius (R_J)	1.67 ± 0.10
Mass (M_J)	0.984 ± 0.085
T_{eff} (K)	2035 ± 52
a (au)	0.0344 ± 0.0026
P (days)	2.14363592 ± 0.0000046
$\log g_P$ (cm s^{-2})	2.91 ± 0.06
Transit Duration (min)	192.20 ± 1.73
$T_c(0)$ (BJD$_{\text{TDB}}$)	$2455364.55217 \pm 0.00020$
Inclination (degrees)	80.09 ± 0.55

Table 1.2: Planetary Parameters of WASP-48b from Enoch et al. (2011) and Turner et al. (2016).

with atmospheric escape. O'Rourke et al. (2014) measured the secondary transit of WASP-48b and indeed found a weak to absent temperature inversion. They were perplexed by this result because they presumed WASP-48 was a quiet star based on its low log R$'_{\text{HK}}$ value of -5.135 (described and defined in Section 5.4.1).

This further lays the groundwork for the intriguing juxtaposition that is WASP-48. It is an old star, which indeed hints at lower activity, but at the same time has a higher-than-anticipated rotation rate and shows no temperature inversion, both of which are correlated with higher levels of stellar activity and high-energy radiation. Therefore, a search for helium on its sole exoplanet will provide insight into whether evolved stars can indeed show high levels of EUV flux and thus drive atmospheric escape beyond the time frame accepted in our current models.

Chapter 2

Observing WASP-48 and Preparing the Data

In order to search for metastable helium in WASP-48b's extended atmosphere, we will be comparing "in-transit" spectral observations of WASP-48, when the hot Jupiter is passing between us and the star, to "out-of-transit" spectral observations. An increase in absorption at the 10833 Å helium line for the in-transit spectrum would suggest the presence of helium in its metastable state. Because helium likely only forms in this state as a result of high-energy radiation from the host star, detecting it suggests the presence of an escaping atmosphere.

High resolution is required to investigate this narrow atomic feature, and because it is in the near-infrared (NIR), it can be observed using ground-based facilities. We will be using data collected from the Habitable-Zone Planet Finder spectrograph on the Hobby-Eberly Telescope in western Texas. In this chapter, we detail the observations and initial examination of the data, including the identification of the helium lines, calculating the signal-to-noise ratio, and determining which exposures were taken in-transit.

2.1   The Habitable-Zone Planet Finder Spectrograph

The Habitable-Zone Planet Finder (HPF) is a fiber-fed NIR spectrograph on the 10 m Hobby-Eberly Telescope at the McDonald Observatory. Though it was originally designed to detect low-mass planets around M dwarfs using precision radial velocity techniques (Mahadevan et al. 2012), it has become widely used in the search for metastable helium in various exoplanets (e.g., Ninan et al. 2020; Krishnamurthy et al. 2021; Vissapragada et al. 2021). It covers the wavelength range of 8079–12786 Å (Ninan et al. 2020) and thus has proven a useful probe of the 10833 Å helium line.

The resolving power of the spectrograph is R∼55,000 (Ninan et al. 2020). We can calculate the wavelength resolution at the 10833 Å line using the formula given in Chromey (2016),

$$R = \frac{\lambda}{\Delta\lambda}, \qquad (2.1)$$

where λ is the wavelength of observation and $\Delta\lambda$ is the wavelength resolution. We calculate $\Delta\lambda \approx 0.20\,\text{Å}$, which means that the HPF can spatially resolve a helium line of width $0.20\,\text{Å}$ or greater. From planetary models of helium absorption (discussed in much greater detail in Chapter 4), we expect the full width at zero intensity of the helium line for WASP-48b to be $\sim 1.3\,\text{Å}$. Therefore, we can expect HPF to be able to resolve any planetary helium feature we may find.

The spectrograph is a Teledyne Hawaii-2RG (H2RG) NIR detector sensitive to the Y (0.98-1.1 μm) and J (1.1–1.4 μm) bands. These bands were chosen because those are the wavelength ranges in which the flux from M dwarfs peaks (Mahadevan et al. 2012). The spectrograph is made up of 2040×2040 active pixels

surrounded by 4 reference pixels on all sides, for a total of 2048×2048 pixels. It uses an echelle grating (Mahadevan et al. 2012), which is a type of diffraction grating that utilizes low groove frequencies and a high order to produce large angular dispersion (Chromey 2016). The detector is made up of 28 orders, each one containing three fibers, or "beams". This is depicted in Figure 2.1.

The three separate fibers that feed the detector are the science fiber, sky fiber, and calibration fiber (see Figures 2.1 and 2.4). The science fiber is pointed at the target and contains the spectrum of the target star: in our case, WASP-48. The sky fiber is pointed at a location offset from the target and simply reads in the telluric spectrum from the sky. It is used in order to be able to subtract telluric emission lines from the target spectrum. Finally, the calibration fiber for the HPF is a laser frequency comb (Metcalf et al. 2019), which is used for simultaneous wavelength calibration of the science target.
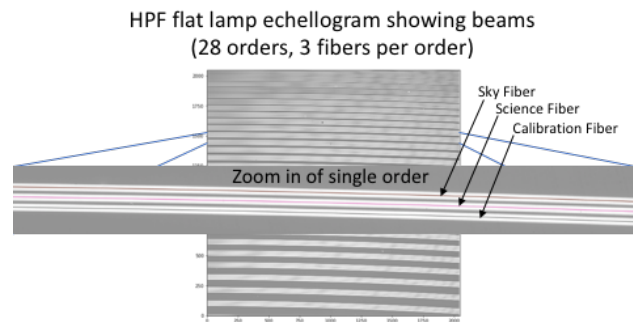
Figure 2.1: Illustration of the HPF echelle orders and beams. Each order consists of a science, sky, and calibration fiber. There are 28 orders that cover the wavelength range 8079–12786 Å. This image is taken from the HPF First Data Release Documentation[1].

As a NIR detector, the HPF operates in a fundamentally different manner than a CCD. For our purposes, the biggest difference is that charge is not transferred from pixel to pixel. Instead, each pixel is read individually, and the charge can

---

[1] https://psuastro.github.io/HPF/HPF-First-Data-Release-Documentation/

be read without affecting the total accumulating charge. These so-called "nonde-structive reads" allow the charge to be read at any give time. Because there is still some baseline thermal noise, the difference between two consecutive reads gives the total charge accumulation. This can be done in an "up-the-ramp" fashion, with a read occurring during a set interval over a given exposure. On the HPF, reads are taken every 10.65 seconds, giving a total integration time of

$$T = (10.65 \text{ s}) \times N, \tag{2.2}$$

where T is the integration time and N is the number of reads.

At this point, the pixels undergo bias removal, nonlinearity correction, and cosmic ray correction using the HPF pipeline (Ninan et al. 2018). Each pixel contains information about the counts of electrons per unit of time, as shown in Figure 2.2. At this stage, the data are designated the 3D "up-the-ramp" data. The slope of the ramp in Figure 2.2 represents the accumulated charge between each consecutive read and is used to derive the flux. By calculating the slope across each pixel, the 3D "up-the-ramp" data are collapsed into 2D flux images, with flux in units of electrons per second. Because only the slope of the ramp is taken into account, if a given ramp has a longer exposure time, this should not affect the data reduction or processing, as the slope should be constant across integration time once the nonlinearity correction is applied (Ninan et al. 2018).

Finally, the 2D spectra are extracted into 1D spectra using the HPF data reduction pipeline (Kaplan et al. 2019). To correct for pixel-to-pixel quantum efficiency variations, the beams are first flat-fielded. In addition, "bad" pixels must be masked. Next, the beams are rectified (or straightened) using polygon clipping, a type of 2D interpolation (Sutherland & Hodgman 1974). Since the beams
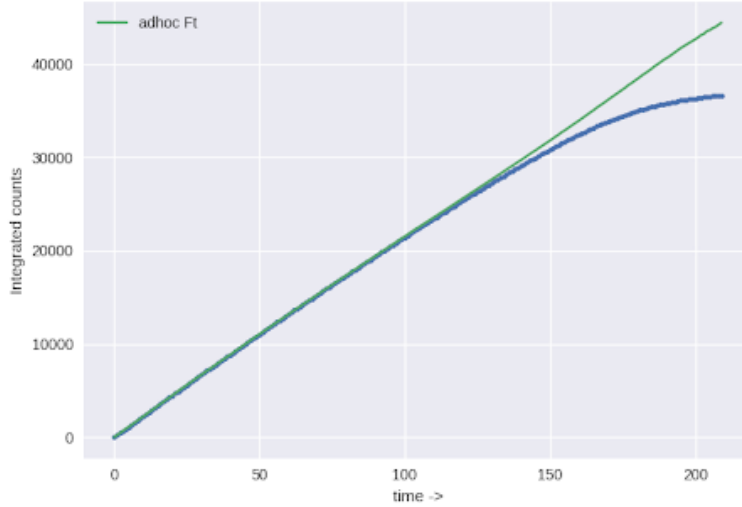
Figure 2.2: An example of an "up-the-ramp" readout of a single pixel on the H2RG detector. Counts of electrons per time (blue line) are read out every 10.65 seconds, and a best fit line (green line) is used to apply the nonlinearity correction. Each of the 2040×2040 pixels contains this information, making this the 3D "up-the-ramp" data, which will be collapsed into 2D flux images. Courtesy of the HPF First Data Release Documentation.

typically curve across the detector, this technique must be applied to maintain resolution and minimize loss of information. Finally, an optimal extraction algorithm (Horne 1986) is then used to weight the data by its uncertainty and cross-dispersion profile and collapse it into a 1D spectrum.

The HPF is a new and rather unique instrument. Since its conception in 2012 (Mahadevan et al. 2012), it has undergone a rigorous testing phase in order to establish the reduction pipeline detailed in this section. While we did not conduct any independent data reduction for this thesis, we collaborated with members of the HPF instrument team to be sure we understood the reduction process before beginning the data analysis.

The final 1D spectra that were used for this work contain the following FITS files. Note that all wavelengths are reported in vacuum.

1. Science Flux (e^- s^{-1})

2. Sky Flux (e^- s^{-1})

3. Calibration Flux (e^- s^{-1})

4. Science Variance (e^- s^{-1})^2

5. Sky Variance (e^- s^{-1})^2

6. Calibration Variance (e^- s^{-1})^2

7. Science Wavelength per pixel (Å)

8. Sky Wavelength per pixel (Å)

9. Calibration Wavelength per pixel (Å)

2.2 Observations Taken

Observations were taken on seven nights between 2019 May 16 UT and 2019 June 29 UT, with multiple exposures taken each night, for a total of 34 exposures. During each night, the target star WASP-48 was observed first, followed by a comparison star, HR7740. Data on the comparison star were obtained in the event that the sky fiber and/or telluric modeling proved insufficient to characterize the spectrum. However, we did not end up utilizing the comparison star data.

Due to the design of the HET, observations can only take place over a limited time span each night, so observing a full transit (from ingress to egress) in one night is not possible. Instead, observations are taken on multiple nights to piece together as much of the transit as possible. Across these seven nights of observations, three transits were observed: on 2019 May 19 UT, 2019 June 16 UT, and 2019 June 18 UT. Together, these observations covered the most phases of the transit, as shown in Figure 2.3. We use the `batman` package from Kreidberg (2015) to plot a model of WASP-48's light curve during a transit, on which we

then overplot the time of our observations in phase space. From Figure 2.3, we can see that the first night, 2019 May 19 UT, examined the first half of the transit, while the other two nights (2019 June 16 UT and 2019 June 18 UT) covered mostly the second half. Therefore, though the entire transit was not observed in one night, most of the phases are accounted for.

Table 2.1 details the individual exposures taken for WASP-48. We include date and time of observation, whether the observation is in or out of transit (detailed in Section 2.5) and the average signal-to-noise ratio (detailed in Section 2.4).
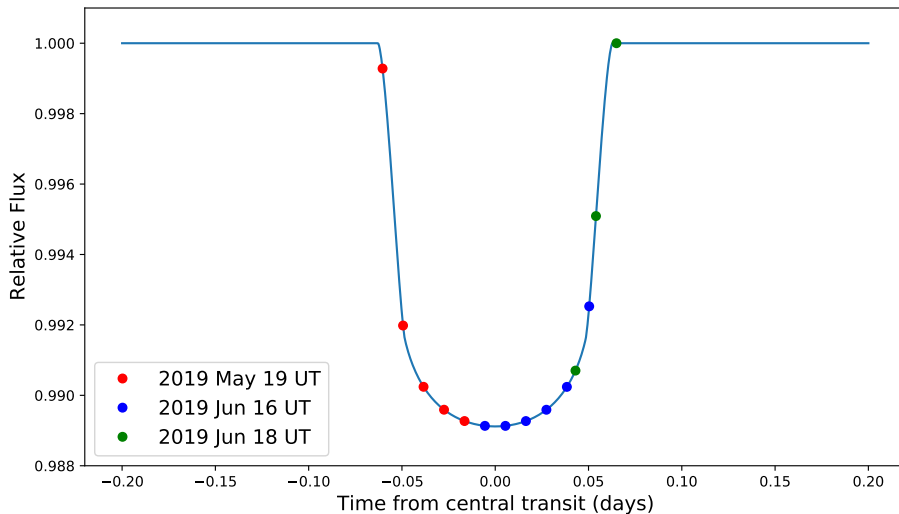
Figure 2.3: Phase plot of observed WASP-48b transits across the three nights in which a transit was observed. Most phases of the transit are covered by the three nights. Transit model done using the `batman` package from Kreidberg (2015).

2.3   Examining the 10830 Å Order

As detailed in Section 2.1, the H2RG detector of HPF has 28 echelle orders spanning a wavelength range of 8079–12786 Å. Thus, our first order of business was to determine which order housed the 10833 Å helium line. The minimum

Date (UT)	Time (UT)	In vs. Out of Transit	Average SNR
2019 May 16	08:06:44	out	112.3
2019 May 16	08:22:33	out	112.9
2019 May 16	08:38:21	out	105.4
2019 May 17	07:55:23	out	66.2
2019 May 17	08:11:11	out	84.0
2019 May 17	08:27:00	out	90.0
2019 May 19	07:21:18	out	92.8
2019 May 19	07:37:07	in	110.2
2019 May 19	07:52:56	in	121.8
2019 May 19	08:08:45	in	120.5
2019 May 19	08:24:33	in	108.1
2019 May 19	08:40:22	in	105.0
2019 Jun 16	05:44:02	in	59.1
2019 Jun 16	05:59:50	in	61.1
2019 Jun 16	06:15:39	in	98.3
2019 Jun 16	06:31:28	in	92.0
2019 Jun 16	06:47:17	in	88.0
2019 Jun 16	07:04:31	in	74.1
2019 Jun 18	05:56:08	out	94.3
2019 Jun 18	06:11:57	out	91.9
2019 Jun 18	06:27:46	out	79.8
2019 Jun 18	06:43:34	out	73.4
2019 Jun 18	10:20:41	in	78.6
2019 Jun 18	10:36:30	in	92.2
2019 Jun 18	10:52:19	in	31.7
2019 Jun 18	11:08:08	out	49.5
2019 Jun 19	05:38:12	out	62.2
2019 Jun 19	05:54:01	out	75.6
2019 Jun 19	06:09:50	out	82.2
2019 Jun 19	06:25:39	out	76.2
2019 Jun 29	09:56:16	out	105.1
2019 Jun 29	10:12:05	out	98.2
2019 Jun 29	10:27:54	out	90.1
2019 Jun 29	10:43:43	out	86.6

Table 2.1: HPF Spectrographic Observations of WASP-48 between 2019 May 16 UT and 2019 Jun 29 UT. Date and time of observation are listed with the average signal-to-noise ratio of each exposure and whether the exposure was taken in or out of transit.

and maximum wavelengths for each order were found, and it was determined the helium line resides in the 20th order. For the remainder of this work, we focus solely on this order and ignore the others.
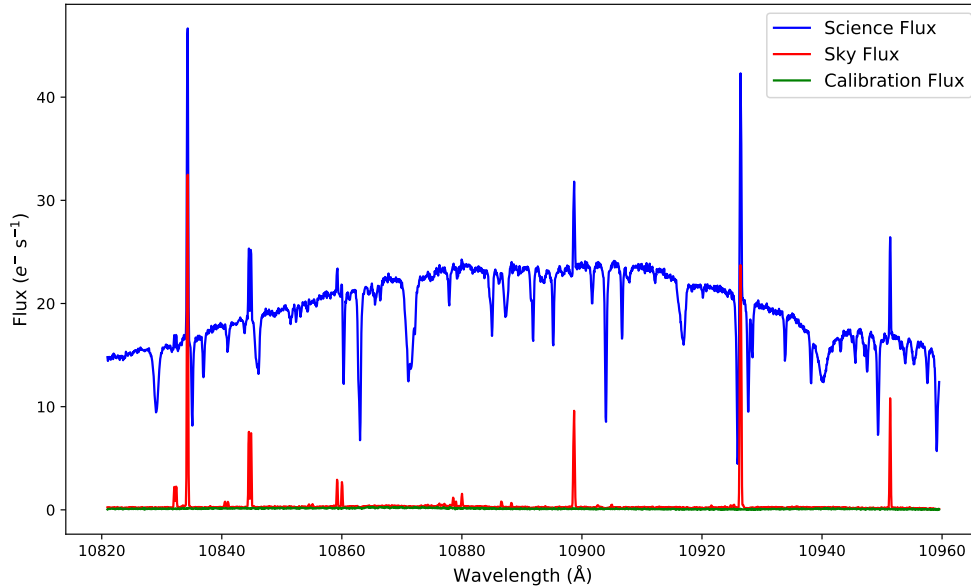
Figure 2.4: Spectrum of WASP-48 on 2019 May 19 08:08 UT. Includes science (blue line), sky (red line), and calibration (green line) fibers. Note that the flux from the calibration fiber is very low. The sky flux is also low except for bright sky ("telluric") emission lines. The science fiber contains the stellar spectrum as well as telluric emission and absorption lines.

In Figure 2.4, we see a first glimpse of the data, which shows us the spectrum from a single exposure on 2019 May 16 08:06:44 UT. The science, sky, and calibration data are all visible in this figure. The sky fiber (red line) has very low flux except for several sharp peaks, which reveal telluric emission lines. These are emission lines from molecules in the Earth's atmosphere and must be subtracted in the data analysis process (see Chapter 3). The green line represents the calibration fiber and has very low flux throughout the entire order. The blue line is the science flux and represents incoming flux from WASP-48. The continuum

emission can be seen from the overall shape of the flux, and many absorption and emission lines are present. Some are stellar in nature, but many are from the Earth's own atmosphere. Notice that each sharp peak from the sky fiber coincides with a sharp peak from the science fiber, demonstrating how molecules in Earth's atmosphere imprint themselves on the stellar spectrum.

2.4   Evaluating the SNR

We next evaluate the signal-to-noise ratio (SNR) across each individual exposure to determine whether any data should be discarded. The SNR is a standard metric in astronomy that compares the measured signal (typically, incoming flux) with background noise. It is defined as:

$$\text{SNR} = \frac{\text{signal}}{\text{noise}} = \frac{\text{flux}}{\sqrt{\text{variance}}}. \tag{2.3}$$

We use Equation 2.3 to determine a pixel-by-pixel value of the SNR for each exposure, using the given flux and variance values. This is shown in Figure 2.5. One can see that the shape of the SNR correlates with the shape of the science spectrum.

Using these data, we calculate a mean SNR for each exposure, which is shown in Table 2.1. We decide to only include in our analysis exposures with an average SNR of greater than 50, which excludes the exposures from 2019 Jun 18 10:52 UT (mean SNR of 31.7) and 2019 Jun 18 11:08 UT (mean SNR of 49.5). This decision was made after conducting an initial examination of each individual exposure. After normalizing each spectrum (detailed in Chapter 3) these two exposures did not appear congruous with the rest of the data. Our biggest indicator that something was amiss came from examining a strong stellar silicon line that occurs

just blue-ward of the helium triplet, at a rest vacuum wavelength of 10830.06 Å. This feature was absent from these two exposures, suggesting that WASP-48 was not successfully observed in these two cases. This, in combination with low SNR values, provided justification to discard these exposures.
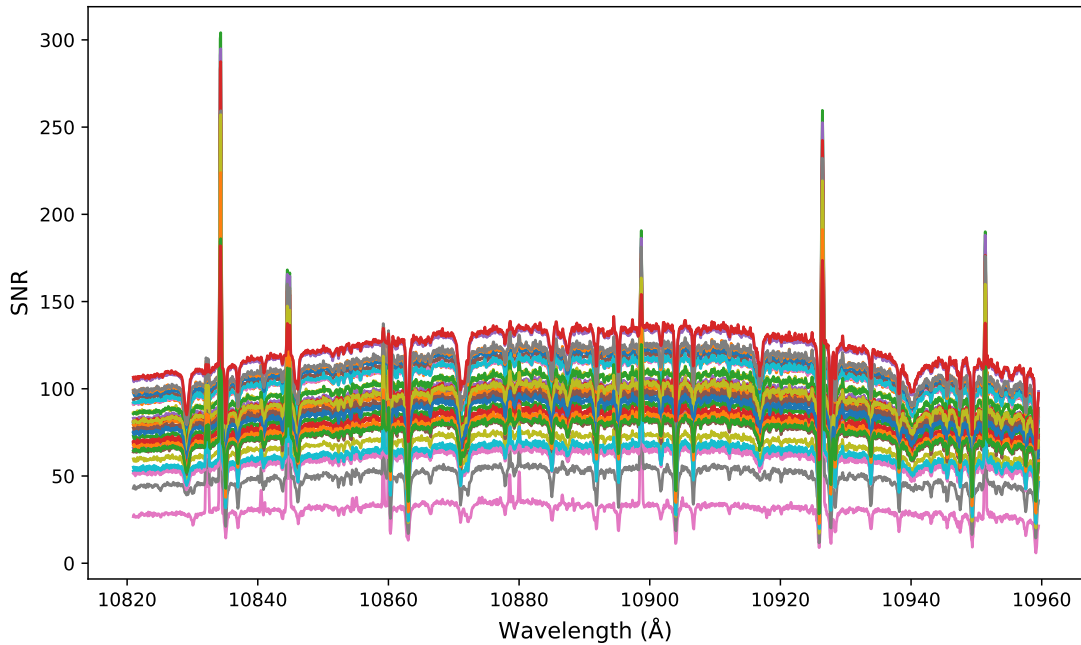
Figure 2.5: Pixel-by-pixel SNR of the 20th echelle order for all 34 exposures. SNR ranges from about 40 to over 100. The two exposures with the lowest SNR (pink and brown lines) end up being discarded in our analysis.

Two more exposures, those from 2019 Jun 16 05:44 UT and 2019 Jun 16 05:59 UT were also eventually discarded. Though their SNR values were relatively low (59.1 and 61.1, respectively), this was not enough to remove them outright. Instead, our data analysis process ultimately proved to be imperfect and particularly errant for these exposures. They were erroneously causing apparent emission in the 10833 Å region, and so were discarded. More details on this realization and justification are provided in Sections 3.6 and 4.2.1.

2.5   Determining In-Transit and Out-of-Transit Observations

The final step before beginning the data analysis is to determine which exposures took place during a transit of WASP-48b and which took place out of transit. To do this, we convert the UT date in the header of each FITS file into its corresponding Barycentric Julian Date in the Barycentric Dynamical Time $(\mathrm{BJD_{TDB}})$ using the `barycorrpy` package (Kanodia & Wright 2018). We will also use this package to apply a barycentric correction to our data, as described in Section 3.1.

We then calculate a series of transit windows using the known period (P), transit duration (d), and the BJD mid-transit discovery time $(T_c(0))$ from Turner et al. (2016). These parameters are listed in Table 1.2. To calculate transit windows, we determine a series of mid-transit times through the equation

$$T = T_c(0) + P \times E, \tag{2.4}$$

where T is the mid-transit time in $(\mathrm{BJD_{TDB}})$ and E is an integer number of cycles after discovery. Next, we calculate the transit window for each of these times based on T and d:

$$T_I = T - \frac{d}{2}, \tag{2.5}$$

$$T_{IV} = T + \frac{d}{2}. \tag{2.6}$$

Here, T_I is the point of first contact and T_{IV} is the point of last contact. This gives us a series of transit ephemerides, which we then use to identify the exposures

that fall into one of these windows. The result is given in Table 2.1. Of the 34 exposures, we find that 14 were taken in-transit and 20 were taken out of transit. Note that once we discard the exposures discussed above, our final tally becomes 11 in-transit and 19 out-of-transit exposures.

To corroborate our technique, we also use the Tapir web interface[2] (Jensen 2013), which was developed as a mechanism to plan observations of periodic targets, including transiting exoplanets. It uses the NASA Exoplanet Archive database to calculate what targets are visible on a given date from a given location. Indeed, the in-transit observations found using our algebraic method described above agrees with the Tapir database results.

Now that we have determined our in-transit versus out-of-transit exposures and have measured the SNR for each exposure, we are ready to dive into the data analysis to determine if there is a planetary helium signature at 10833 Å.

---

[2]https://astro.swarthmore.edu/~jensen/tapir.html

Chapter 3

The Road to the Transmission Spectrum

We are now are ready to build the transmission spectrum, which will allow us to determine whether there is helium in the extended atmosphere of WASP-48b. In order to do so, we first must identify the helium triplet on the spectrum. We will apply telluric corrections, remove the stellar continuum and shift the spectrum into the correct rest frame. Then, we will create a master out-of-transit spectrum, divide each in-transit exposure by this master spectrum, and weight and sum the resulting spectra to arrive at the final transmission spectrum. First, however, we must turn to the 20th order, in which we know helium resides, and get to know the spectrum a bit more.

3.1 Homing in on Helium

We will focus on the range of approximately 10827–10838 Å, as shown in Figure 3.1. We know the 10833 Å helium triplet resides in this portion of the spectrum, although its expected wavelength position will be offset from its rest wavelength, because the spectrum is initially in a topocentric rest frame.
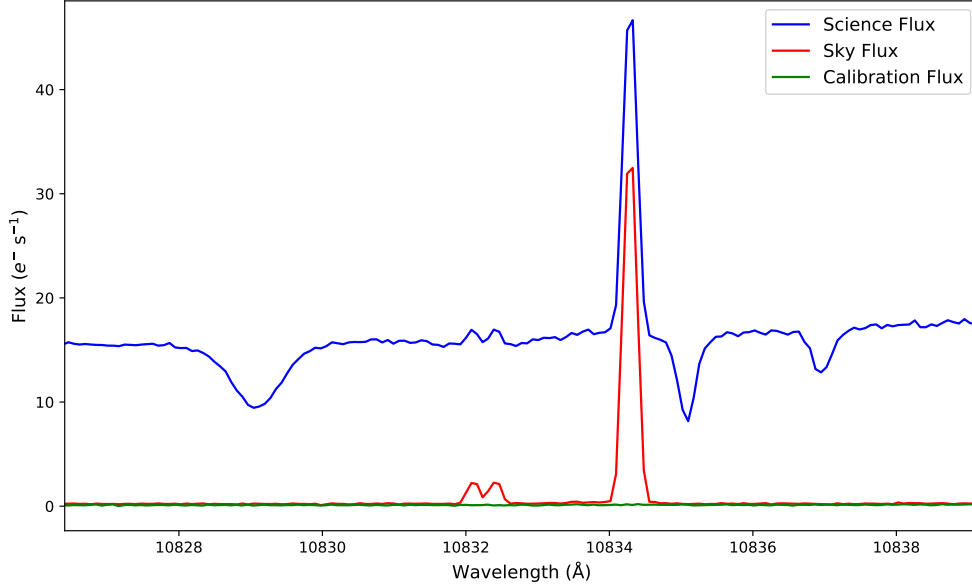
Figure 3.1: Spectrum of WASP-48 on 2019 May 19 08:08:20 UT in the topocentric rest frame. It is centered around the 10833 Å line. We include the science (blue), sky (red), and calibration(green) fibers. From left to right, we see a stellar feature, two telluric emission lines (one doublet and one very bright line), and two telluric absorption lines. We demonstrate how we identify these features in the coming sections.

For the remainder of this work, we focus on this portion of the spectrum. At first glance, in Figure 3.1, we see in the science fiber what appears to be a stellar spectral feature around 10829 Å, two emission features around 10832 and 10834 Å, and two other absorption features around 10835 and 10837 Å. All of these features must be understood in order to properly analyze the data. In turn, we will demonstrate that we are seeing a stellar silicon line, two hydroxyl (OH) telluric emission lines, and two water vapor telluric absorption lines, respectively. First, however, we must determine the precise vacuum wavelengths of the helium triplet and determine where the helium line is located in the spectrum.

3.1.1   Converting from air to vacuum wavelengths

Because the Habitable Zone Planet Finder operates in vacuum wavelengths, we must convert our expected helium lines from air to vacuum wavelengths. We use the air wavelength of helium given on the National Institute of Standards and Technology (NIST) Atomic Spectra Database[1]: 10829.09114, 10830.25010, and 10830.33977 Å. To convert to vacuum wavelengths, we use the following conversion taken from the Sloan Digital Sky Survey library[2]:

$$\lambda_{\mathrm{air}} = \frac{\lambda_{\mathrm{vac}}}{1.0 + 2.735182 \times 10^{-4} + \frac{131.4182}{\lambda_{vac}^2} + \frac{2.76249 \times 10^8}{\lambda_{vac}^4}}. \tag{3.1}$$

We use the solve function from the `SymPy` library in Python to solve the above equation for λ_{vac} for the three given values of λ_{air} above. We find our vacuum wavelengths for helium to be: 10832.07, 10833.22, and 10833.31 Å, which corroborate the values given in Allart et al. (2018). The air and vacuum wavelengths are listed in Table 3.1.

Air Wavelength (Å)	Vacuum Wavelength (Å)
10829.09	10832.07
10830.25	10833.22
10830.34	10833.31

Table 3.1: Air and vacuum wavelengths of metastable helium. Air wavelengths are taken from the NIST Atomic Spectra Database, and vacuum wavelengths are calculated from these air wavelengths using Equation 3.1.

---

[1]https://www.nist.gov/pml/atomic-spectra-database
[2]https://classic.sdss.org/dr7/products/spectra/vacwavelength.html

3.1.2 Determine Helium's Location in the Spectrum

Before diving into the data analysis, we begin by conducting an initial examination of the spectrum. We will shift the spectrum into the stellar rest frame in order to examine where the helium triplet falls.

Shifting into the Barycentric Rest Frame

To determine where the helium line is on our spectrum, we must account for both the motion of the Earth and the motion of the star. First, we use the `barycorrpy` Python package developed by Kanodia & Wright (2018), based on the IDL code by Wright & Eastman (2014) to shift the spectrum from a topocentric rest frame into a barycentric rest frame. This package was developed for implementation in high-precision radial velocity studies and corrects for the rotation and revolution of the Earth, precession, nutation, and polar motion of the Earth, and gravitational time dilation due to solar system objects, among other more precise corrections (including the Shapiro delay and leap second offset) that are not needed for our purposes. The package requires an input of time in UTC, observation location on the Earth, and position of the source. It then outputs a barycentric velocity for each given exposure that can be converted into a wavelength correction and added to the wavelengths of our spectra. We can see the velocity correction for each exposure in Figure 3.2.

We can see in Figure 3.2 that the velocity correction factor decreases slowly over the course of the observations, likely due to the orbit of the Earth. If we zoom in on any particular week, we can also see the correction decreasing over a given night due to the Earth's rotation, as shown in Figure 3.3.
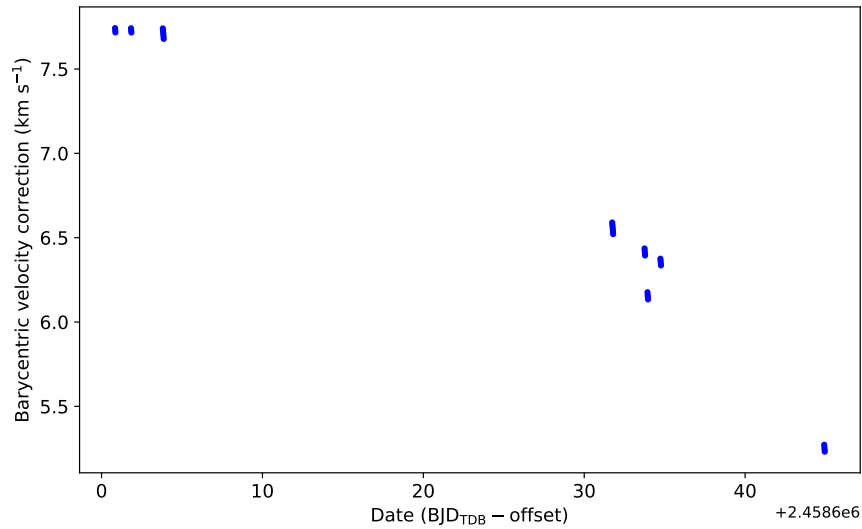
Figure 3.2: Barycentric velocity corrections for all exposures by BJD_{TDB} date using `barycorrpy` Python package. The offset on the BID_{TDB} date is 19 days, which simply allows us to start the x-axis at one. The velocity corrections decrease between the beginning and end of the observations due to Earth's orbit around the Sun.
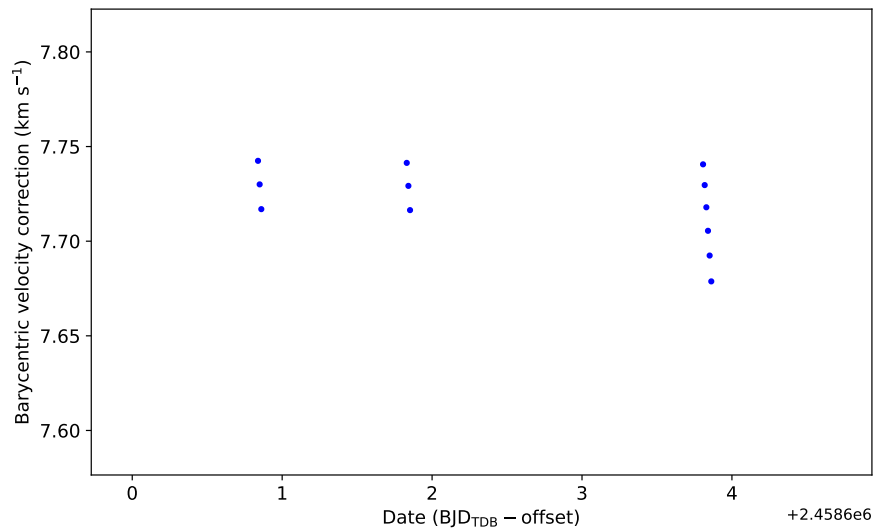

Figure 3.3: Barycentric velocity corrections for the first week of exposures using `barycorrpy` Python package. As in Figure 3.2, we allow an offset of 19 days to set the first observation at one on the x-axis. Each night, the velocity correction decreases sharply due to Earth's rotation.

We then apply this barycentric correction to each spectrum by converting the velocity correction into a change in wavelength using the Doppler formula,

$$\frac{\Delta\lambda}{\lambda} = \frac{v}{c},$$

(3.2)

where v is the barycentric velocity correction and c is the speed of light. We use this equation to solve for $\Delta\lambda$ at each wavelength in our spectrum, and we add this $\Delta\lambda$ to the given wavelengths to arrive at the barycentric rest frame.

Shifting into the Stellar Rest Frame

Next, we must correct for the motion of the star by shifting the spectrum into the stellar rest frame. This involves two components: the systematic radial velocity and the reflex radial velocity due to the orbit of the planet. We will ignore the latter, because we can show that the radial velocity semiamplitude is less than the spectral resolution of HPF (see Section 2.1). Radial velocity semiamplitude is a metric used to measure the magnitude of fluctuations in stellar radial velocity due to an orbiting planet or binary star. We use the equation for radial velocity semiamplitude (K) from Lovis & Fischer (2010),

$$K = \frac{28.4329 \text{ m s}^{-1}}{\sqrt{1 - e^2}} \frac{m_2 \sin i}{M_{\text{Jup}}} \left(\frac{m_1 + m_2}{M_\odot}\right)^{-1/2} \left(\frac{a}{1 \text{ au}}\right)^{-1/2},$$

(3.3)

where e is eccentricity (which we assume to be zero), m_2 is the mass of the planet in Jupiter masses, m_1 is the mass of the star in solar masses, and a is the semimajor axis in au. The values for these parameters can be found in Tables 1.1 and 1.2. We calculate that the radial velocity semiamplitude is ~ 138 m s^{-1}, which translates into ~ 0.0050 Å at 10833 Å using Equation 3.2. From Section

2.1, we know that the spectral resolution of the HPF is $0.20\,\text{Å}$ at this wavelength. Therefore, this additional shift due to the reflex motion of the star is too small for the spectrograph to discern, and we can safely ignore it.

Therefore, the final velocity correction is for the star's radial motion. From the SIMBAD Astronomical Database[3], the heliocentric radial velocity of WASP-48 is -19.740 km s^{-1}. Though we start in the barycentric, not heliocentric rest frame, we ignore this small difference and confirm that it is negligible in Section 3.1.3. We convert this velocity into $\Delta\lambda$ using Equation 3.2, and add $\Delta\lambda$ to the given wavelengths to arrive at the stellar rest frame, depicted in Figure 3.4. No visible spectral line is seen for the blue-component of the helium triplet, although this line typically has a weaker signature. Unfortunately, we do see that the red component is directly over the OH doublet in the stellar rest frame. Therefore, we must take care when removing these lines, as will be described Section 3.3.
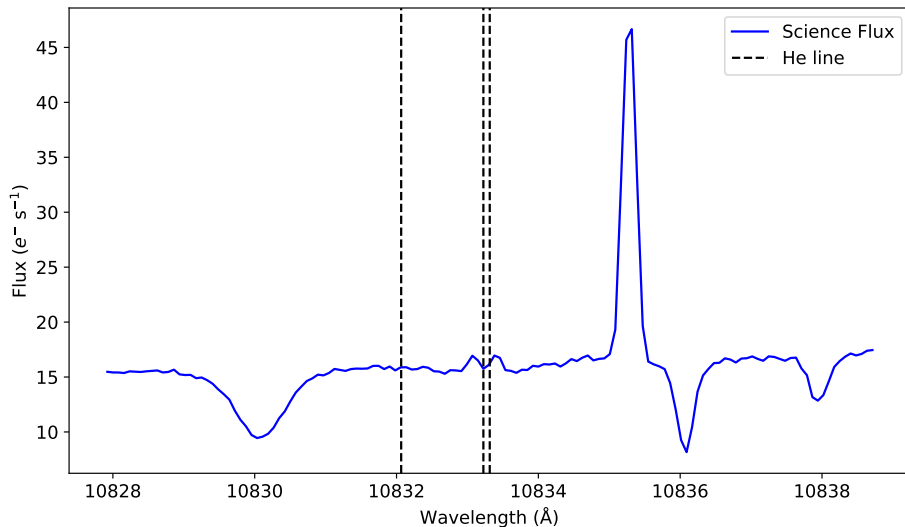
Figure 3.4: Expected location of helium triplet in the stellar rest frame for exposure taken on 2019 May 19 08:08 UT following barycentric and stellar radial velocity corrections. The red component of the helium triplet is over the OH emission doublet.

---

[3]http://simbad.u-strasbg.fr/simbad/

3.1.3   Confirming the Validity of the Rest Frame Shifts

While Figures 3.2 and 3.3 make intuitive sense, we would like an independent validation of our velocity corrections. To do this, we examine the apparent stellar spectral line seen to the red of the helium lines. By comparing our spectrum with those seen in Allart et al. (2019) and Salz et al. (2018), we determine that this line is neutral silicon, with a rest vacuum wavelength of 10830.06 Å taken from the NIST Atomic Spectral Database. We shift the spectrum into the stellar rest frame and can see in Figure 3.5 that the rest wavelength of the silicon line correlates very well with the core of the line seen in the spectrum. We can then confidently state that this is indeed a stellar feature, and that our technique for barycentric and stellar radial velocity correction works well.
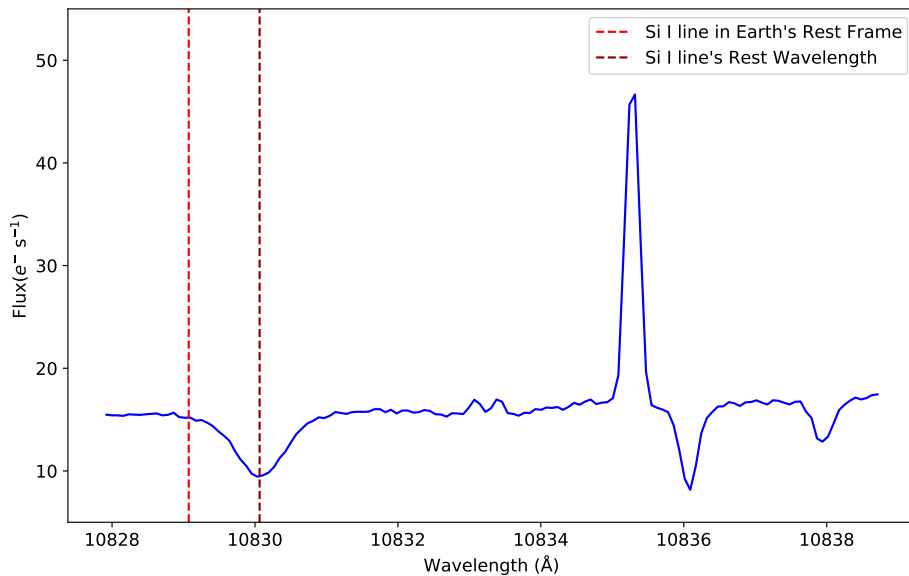
Figure 3.5: Spectrum in stellar rest frame taken on 2019 May 19 08:08 UT. The position of the silicon line in the topocentric rest frame versus its rest wavelength is depicted with vertical dashed lines. The core of the silicon line does align with its rest vacuum wavelength, which validates our velocity correction techniques.

3.2   A Note on Error Propagation

At this point, we begin propagating error as we go through the data analysis process. We start with the given variances for each exposure, and calculate error propagation following Bevington & Robinson (1969), where the propagated error, σ_{total}, is given by

$$\sigma_{total}{}^2 = \sum_i \sigma_i{}^2 \left(\frac{\partial f}{\partial x_i} \right)^2 , \qquad (3.4)$$

in which the function f is a function, x_i is each variable contained within that function, and σ_i^2 is the variance associated with each x_i. We exclude error bars from the intermediate plots for ease of visualization, but the final propagated error is shown in the transmission spectrum in Figure 3.12.

3.3   Telluric Correction

Now that we have established the location of the helium triplet in the stellar rest frame and confirmed the validity of our velocity correction techniques, we are ready to begin the data analysis. We start once again with the spectra in a topocentric rest frame and will shift the data into the correct rest frame later in the process.

Because we are using a ground-based telescope, part of the spectral signatures we see are due to the Earth's own atmosphere. Thus, the very first step in our data analysis process is to remove these telluric lines. In particular, we focus on the two emission lines closest to the 10833 Å line, as these are directly interfering with our ability to see any stellar helium line.

3.3.1 Confirmation of OH Emission Lines

The helium detection literature suggests that the emission lines seen in the spectra are due to OH (Allart et al. 2018; Ninan et al. 2020). We would like to confirm this independently. Rousselot et al. (2000) lists two OH sky emission lines in vacuum at 10832.257 and 10834.289 Å. We compare this to our spectrum and estimate that these probably refer to the emission lines we see. However, it is clear that the OH lines cited in this paper are not at high enough precision to distinguish between the two smaller peaks on the left. We want to be able to parse all the OH transitions that are contributing to these emission lines. Thus, we use the HITRAN (high-resolution transmission molecular absorption) database[4] to find OH emission lines in the wavelength range of interest. The values in this database are given in cm^{-1}, so we must convert into Å. We find four OH lines in the region of interest, as shown in Table 3.2.

OH line from HITRAN (cm^{-1})	Converted OH line (Å)
9231.82	10832.10
9231.56	10832.41
9223.00	10834.24
9229.92	10834.33

Table 3.2: OH sky emission lines from HITRAN converted from cm^{-1} into Å. We will use these to validate whether the emission lines we see in the spectra are indeed telluric OH lines.

We confirm that these lines match those seen in our spectrum in Figure 3.6. Surprisingly, the large peak is actually two separate lines that are blended together in the spectrum. It is also important to note that the OH sky emission lines do

---

[4]https://hitran.org

not need to undergo any velocity corrections, since these lines originate in the Earth's atmosphere. In other words, these lines occur at their rest wavelengths when the spectrum is in the topocentric rest frame.
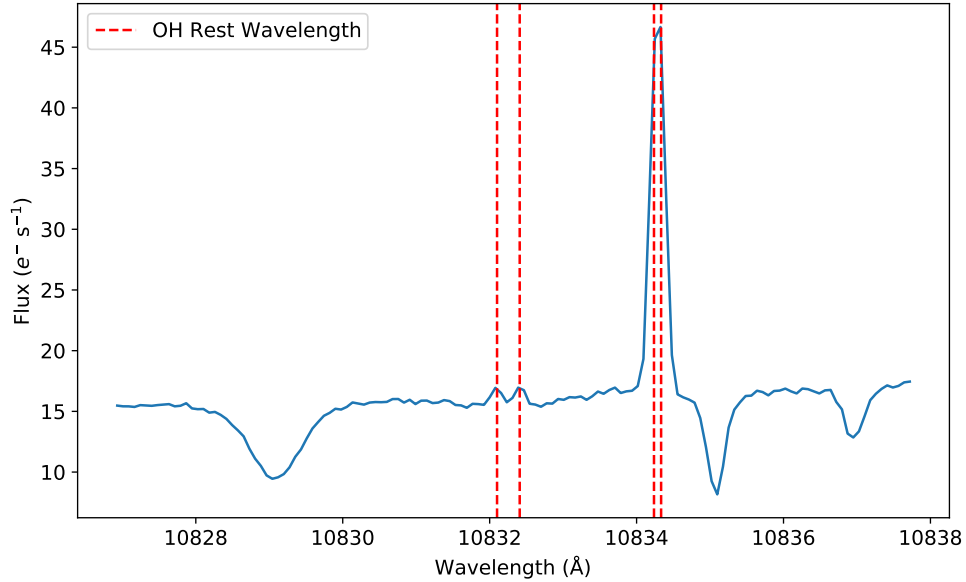
Figure 3.6: Spectrum from 2019 May 19 08:08 UT in the topocentric rest frame. Rest wavelengths of HITRAN derived OH lines are shown with vertical dashed lines. These coincide with the emission lines seen in the spectrum, confirming they are OH lines originating in the Earth's atmosphere.

3.3.2 Removing the OH Emission Lines

To remove the OH emission lines, we must subtract the sky fiber from the science fiber. First, the continuum of the sky spectra are subtracted by fitting them to a first order polynomial. The sky spectra are then interpolated with the science spectra using the `scipy` cubic interpolation function to ensure proper subtraction between the two.

Looking back at Figure 3.1, one can see that the right-most OH emission peak of the science and sky fiber are different in intensity, but we know they should be

equal because they arise from the same source. To correct for this, we calculate a sky fiber scaling ratio (which on average was ∼0.93), using the leftmost OH line in the large peak. We apply this to the region in the sky spectrum surrounding these telluric lines, between 10831–10835 Å. This will allow for the small OH emission doublet to be corrected as well. Note that we tried several methods for normalizing the peaks, and this method was most proficient at minimizing residuals without artificially creating a flat line at the continuum or overcompensating and leaving an OH imprint on the spectrum. Though the scaling ratio of the sky spectrum does have a chromatic (wavelength) dependence, the two OH emission lines are so close in wavelength, so this should not be an issue here. Once we apply the scaling factor, we simply subtract the interpolated sky spectrum from the science spectrum, as shown in Figure 3.7.

Figure 3.7: Science fiber in the topocentric rest frame, both before (green line) and following (blue line) sky emission subtraction. This exposure is from 2019 May 19 08:08 UT. The sky subtraction has successfully removed the OH emission lines and has revealed what appears to be a stellar helium line underneath the small OH doublet.
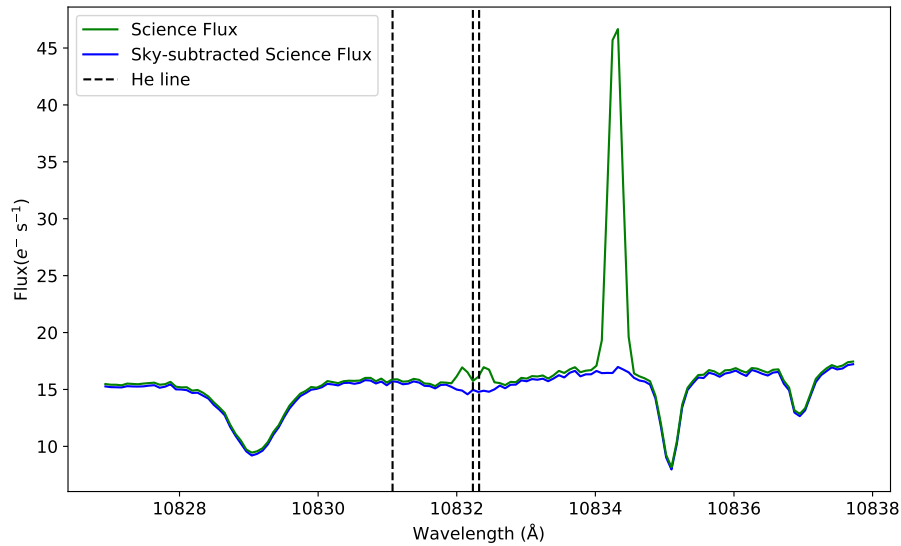
At first glance, this technique has revealed what appears to be a shallow stellar helium line underneath the OH emission lines. We corroborate this assumption by scanning through the full suite of exposures, shifting the spectra in a barycentric rest frame and applying the stellar radial velocity shift to the predicted helium triplet location. We see the core of this shallow line align with the location of the red component of the helium triplet in every case. Because the core of the feature lines up with the predicted helium location in different barycentric rest frames, this suggests it is indeed a stellar helium feature.

Using a Stellar Model to Confirm Features

To independently confirm the two stellar features, silicon and helium, that we see in this portion of the spectrum, we compare our observations with the PHOENIX model described in Husser et al. (2013). We use the PHOENIX online library of stellar spectra[5], in which we input stellar effective temperature, surface gravity, [Fe/H], and [α/M] to generate a spectrum. These parameters are listed in Table 1.1. For [α/M], which has not been measured for WASP-48, we estimate a value of -0.20 after running the model with various [α/M] inputs. For [Fe/H], which goes in step size of 0.5 on the PHOENIX website, we set the value to -0.5 after also testing multiple values. Changing the [Fe/H] and [α/M] input parameters did not meaningfully change the spectral features seen, but only changed their relative magnitudes. We then apply the rotational broadening package from `PyAstronomy` to the stellar spectrum. This is based on the stellar limb darkening coefficient and rotational velocity. The resulting synthetic spectrum is then normalized by dividing the spectrum by a first-order polynomial, and is compared to a normalized observed spectrum (from 2019 May 19 08:08 UT) in Figure 3.8.

---

[5]`https://phoenix.astro.physik.uni-goettingen.de/?page_id=15`
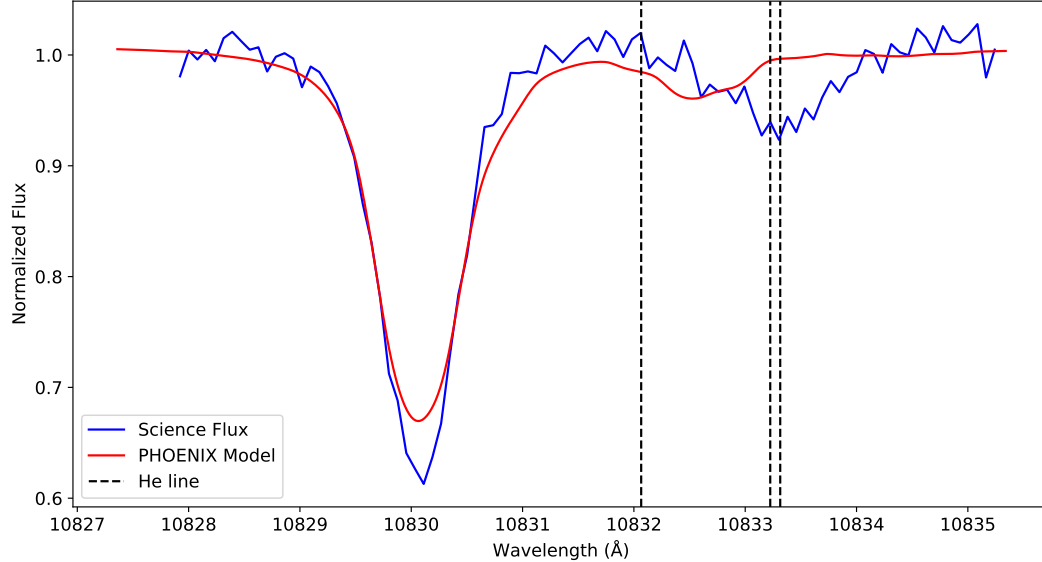
Figure 3.8: Normalized and rotationally broadened PHOENIX stellar model compared to normalized science flux from 2019 May 19 08:08 UT in the stellar rest frame. Though the observed silicon line matches relatively well with the model, we do not see a helium line, as expected. We see a feature that may be due to other molecules present in the stellar atmosphere.

Interestingly, the observed silicon line matches well with the model, corroborating our assertion that indeed it is a stellar line, but we do not see the expected helium feature. Before the synthetic spectrum is rotationally broadened, we see a small feature where the red component of the helium triplet is expected, but there are a multitude of other small stellar features surrounding it. When the rotational broadening is applied, all these features are erased except for the shallow feature between the helium lines seen in Figure 3.8. Using the NIST Atomic Spectral Database, we tentatively identify this broadened feature as a blended CO_2 and $H_2^{18}O$ line. The lack of helium in the synthetic spectrum remains a mystery. One possibility is that the discrepancy arises because this model was designed for main sequence stars. Since WASP-48 is evolving off the main sequence, the physics of

its atmosphere might not be analogous to a main sequence star with equivalent input parameters. Our detection of stellar helium (which is still supported by observing how the feature shifts in the barycentric rest frame according to the stellar velocity) suggests that perhaps there could be convective dredge-up of helium, although this is merely speculative. For now, we leave this for further follow-up. This intrigue first arose from our successful subtraction of telluric emission lines, and we must now address the telluric absorption features.

3.3.3   Identifying the Water Absorption Lines

As was the case for the telluric emission lines, the helium literature first hinted that the two features to the right of the OH emission lines were water vapor absorption features due to Earth's atmosphere. We follow the same procedure outlined in Section 3.3.1 to confirm that these are indeed telluric water absorption features. We use HITRAN to identify water lines in the region of interest (see Table 3.3) and plot these on a spectrum in the topocentric rest frame, as shown in Figure 3.9. We see that the HITRAN-derived wavelengths do coincide with the location of the absorption lines in the spectrum when it is in the topocentric rest frame, corroborating our guess that these are not stellar features, but water vapor lines from the Earth's atmosphere.

Water line from HITRAN (cm^{-1})	Converted water line (Å)
9229.29	10835.07
9227.70	10836.94

Table 3.3: H_2O absorption lines determined from HITRAN, used to confirm the apparent telluric absorption features to the right of the OH emission lines. As in Table 3.2, we converted from cm^{-1} into Å.
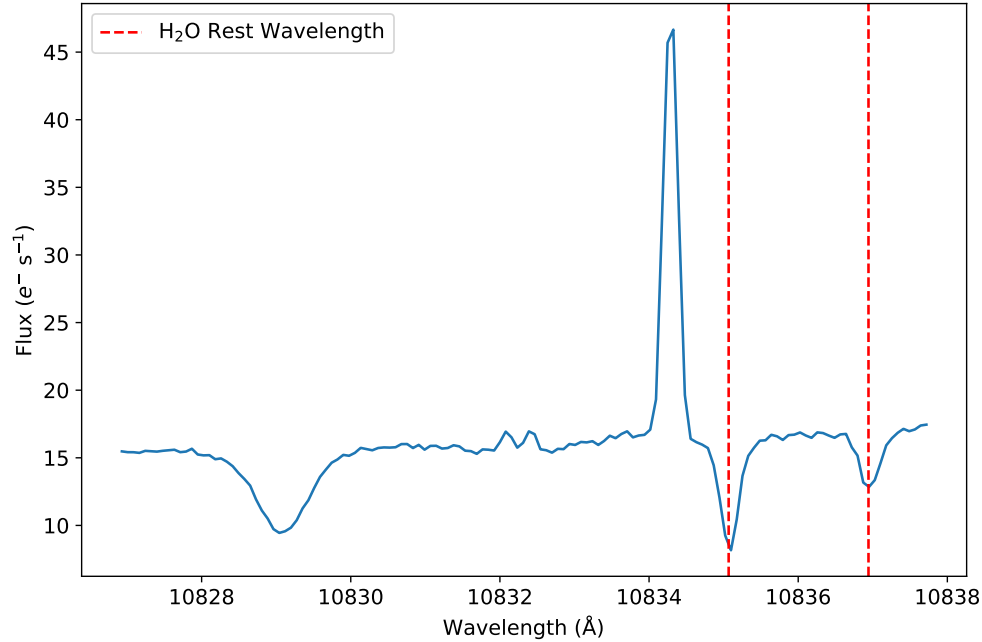
Figure 3.9: Spectrum from 2019 May 19 08:08 UT shown in the topocentric rest frame, with the locations of water absorption lines from HITRAN plotted as vertical red dashes. This demonstrates that the right-most two features in this region of the spectrum are indeed water features from the Earth's atmosphere.

Because these features are far from the helium lines (almost 2 Å), and fall outside the wavelength range required for our analysis, we follow Allart et al. (2019) and choose not to correct for these lines. We note that the telluric standard star, HR7740, does show these telluric absorption lines in its spectrum. If needed, we have this telluric standard we can use to subtract these absorption features, but we will ignore them at this stage. From now on, we will focus on the wavelength range between 10831–10835.

3.4 Stellar Continuum Removal

The next step in the data analysis process involves removing the stellar continuum itself in order to normalize the spectra. We fit a first-order polynomial to the stellar continuum, and divided the entire science spectrum by this polynomial. We chose a first-order polynomial because in the narrow wavelength range we are examining, the continuum is close to flat. We did a visual inspection of second-order and third-order polynomials, but these did not fit the continuum as well and resulted in highly extrapolated values at the edge of the order.

3.5 The Master Out-of-Transit Spectrum

Now that we have all of our individually corrected spectra, we create a master out-of-transit spectrum in the stellar rest frame. We first shift each individual spectrum into the stellar rest frame by applying barycentric and stellar radial velocity corrections, as described in Section 3.1.2. We interpolate each individual out-of-transit spectrum to a reference spectrum using the `scipy` cubic interpolation function. We then sum the spectra together, with each spectrum weighted by the inverse of its variance following Salz et al. (2018) and Ninan et al. (2020). This is particularly important because these data were taken over multiple nights with differing SNRs. We follow the methodology of Bevington & Robinson (1969) for the weighted average:

$$\mu = \frac{\sum \frac{x_i}{\sigma_i^2}}{\sum \frac{1}{\sigma_i^2}}, \tag{3.5}$$

where μ is the weighted average, x_i is the science flux, and σ_i^2 is the variance associated with each flux value. We thus divide each flux value by its variance, interpolate and sum across all spectra, and then divide by the sum of the inverse

variances. This gives us a one-dimensional array of out-of-transit fluxes.

We will divide each in-transit spectrum by this master out-of-transit spectrum before calculating the final transmission spectrum, but before we do this, we can create an analogous master in-transit spectrum to compare with the out-of-transit spectrum. This allows us to perform a visual inspection of the helium line and see if there is any hint of planetary helium. We cannot simply divide the master spectra by each other to arrive at our transmission spectra because we need to shift the spectra into their planetary rest frames, but examining them together does provide us with a sense of whether this investigation is likely to be a detection or non-detection.
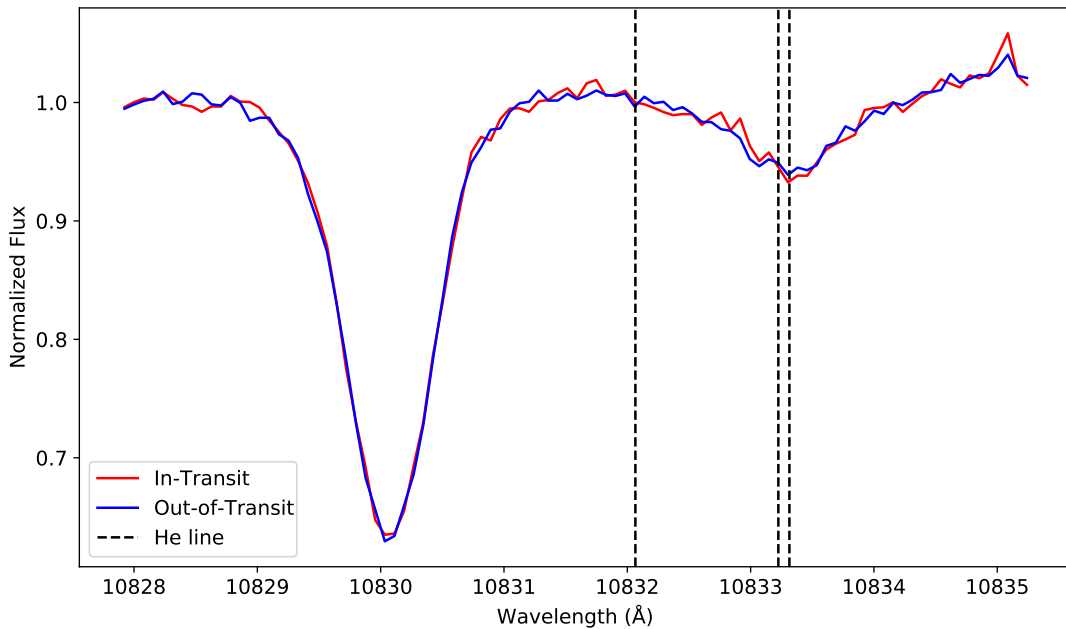

Figure 3.10: Master in-versus-out of transit spectrum in the stellar rest frame. The individual spectra have been interpolated and undergone a weighted sum, with their inverse variances used as weights. No planetary helium signal is visible.

From Figure 3.10, we do not see any indication that there is a source of plane-

tary helium. The in-transit and the out-of-transit spectra are very much aligned, suggesting there is no meaningful difference between them. To confirm this, however, we must create our final transmission spectrum and use the propagated error to determine significance.

3.6 Arriving at the Transmission Spectrum

The final step in this process is to create the transmission spectrum, which tells us the relative difference between the in-transit and out-of-transit spectra. The y-axis is defined as

$$\frac{F_{\text{in}} - F_{\text{out}}}{F_{\text{out}}} = \frac{F_{\text{in}}}{F_{\text{out}}} - 1, \tag{3.6}$$

where F_{in} and F_{out} are the in-transit flux and out-of-transit flux, respectively. In this case, we divide each in-transit exposure by the master out-of-transit spectrum while they are both still in the stellar rest frame. To do this, we interpolate the master out-of-transit-spectrum to each in-transit spectrum, which does not change the master out spectrum too much, but only ensures that they are properly aligned before the division occurs.

At this point, we have a series of ratio spectra, which must be summed to arrive at the transmission spectrum. First though, we shift these spectra into their planetary rest frames. This is important to do because if there is a planetary helium signature, it is imprinted on the stellar spectra, and its core might not align with the core of the stellar helium line. Though radial velocity is minimized when the planet is at its central point of transit, we perform a back-of-the-envelope calculation to estimate planetary radial velocity at ingress and egress (the beginning and end of transit, respectively) and find that it is ~ 66.6 km s^{-1}, which translates into a wavelength shift of ~ 2.4 Å. Because none of the in-transit exposures were

taken right at ingress or egress (the exposure from 2019 Jun 18 10:52 UT, which did lie close to egress, was discarded), we can expect the planetary radial velocity to be smaller than this value, but this is still a large enough shift that it must be taken into account. We also need to confirm that the maximum radial velocity shift is smaller than the wavelength difference between the red component of the helium triplet and the closest telluric water line, which is ~ 1.8 Å.

We use the `radvel` package to calculate planetary radial velocity (Fulton et al. 2018) for each of the in-transit exposures. This package uses the central time of transit, period, eccentricity, longitude of periastron, radial velocity semiamplitude, and time of observation to calculate the radial velocity of the star ($V_{\mathrm{r,star}}$) for each exposure. We then calculate the radial velocity of the planet ($V_{\mathrm{r,planet}}$) from

$$V_{\mathrm{r,planet}} = -V_{\mathrm{r,star}} \times \frac{M_{\mathrm{star}}}{M_{\mathrm{planet}}}, \qquad (3.7)$$

where M_{star} and M_{planet} are the mass of the star and planet, respectively. We check the results of this calculation in Figure 3.11, which depicts the radial velocity changing with phase of transit. As expected, prior to central transit, the radial velocity is negative (meaning the planet is moving towards us), at the center of transit it is zero, and after the central transit it is positive (meaning it is moving away from us). The maximum planetary radial velocity is ~ 32.7 km s^{-1}, which translates into ~ 1.2 Å. Because this is smaller than the wavelength difference between helium and the telluric water lines, we are justified in continuing to leave those telluric lines be. We also conduct a visual examination of each in-transit spectrum in the planet rest frame to confirm that the helium line does not overlap in any instance with the telluric water lines.
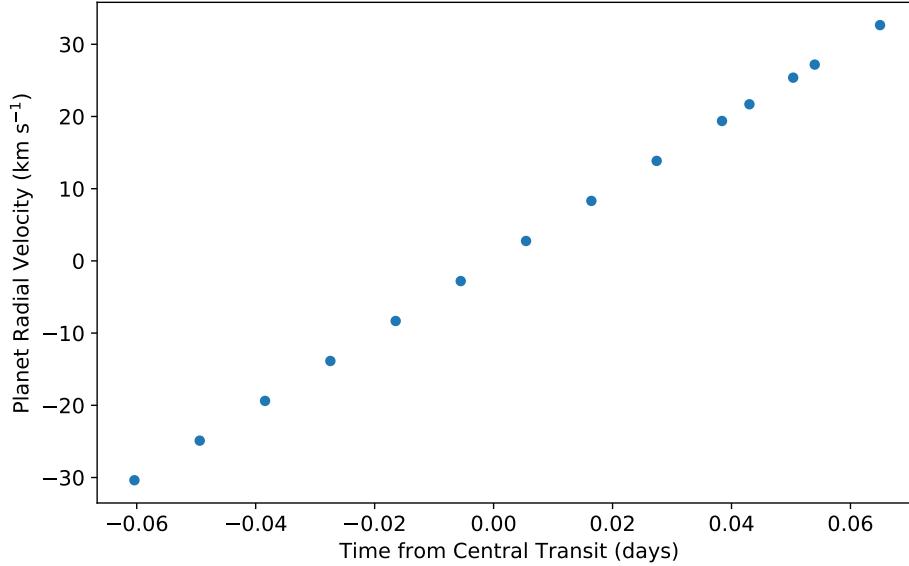
Figure 3.11: Planetary radial velocity calculated using the `radvel` package as a function of time from central transit. We plot this as a check on this technique. As expected, we see the radial velocity shift from negative to zero at the time of central transit to positive as the planet approaches egress.

We convert the calculated radial velocities from the `radvel` package into a change in wavelength using Equation 3.2, and we add this to the given wavelengths to shift the spectra into their planetary rest frames. We interpolate the spectra to a single reference spectrum and apply a weighted sum based on the inverse variances to arrive at the final transmission spectrum, shown in Figure 3.12. From the figure, it is apparent that there is no obvious planetary helium absorption, as the spectrum shows no meaningful deviation from zero at the location of the helium triplet.

An important note to make here is that two additional exposures have been excluded from this transmission spectrum: those from 2019 Jun 16 05:43 and 2019 Jun 16 05:59. We made the final decision to exclude them later on, in the statistical analysis process (see Section 4.2), but the first hint that something was
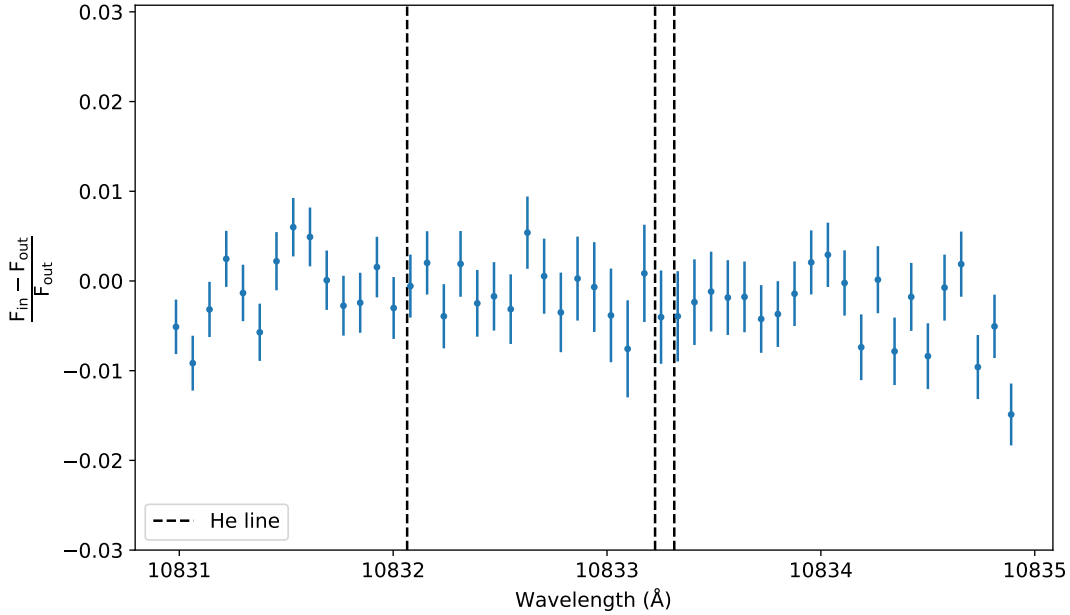
Figure 3.12: Master transmission spectrum in the planetary rest frame depicting propagated error, zoomed in on the wavelength region immediately surrounding the helium triplet. The spectrum is flat, suggesting there is no planetary metastable helium in the extended atmosphere of WASP-48b.

amiss occurred at this stage. When these exposures were included, we noticed that there was a spike of apparent emission between the red and blue components of the helium triplet, which we know to be erroneous because of the comparison with the stellar model and other helium detection papers which depict this wavelength regime. When we excluded these two exposures, this apparent emission vanished. This suggests that our data analysis process did not work as well for these two exposures compared with the rest. In addition, their SNRs are the lowest of our included sample at 59.1 and 61.1, respectively.

Overall, the transmission spectrum is flat, demonstrating that there is no difference between the in-transit and out-of-transit spectrum. While our eyes and intuition tell us this is the case, we must confirm that this is indeed a non-

detection by calculating an absorption value from this transmission spectrum and determining its significance. This will be described in Chapter 4.

3.6.1 Transmission Spectrum Per Night

We can also investigate the shape of the transmission spectrum per night to ensure there is no hint of helium detection in only one night. (As will be discussed more in Chapter 6, it is becoming apparent that variability in helium absorption can often occur.) We apply the process described for calculating the transmission spectrum to exposures taken each night. The result is shown in Figure 3.13.
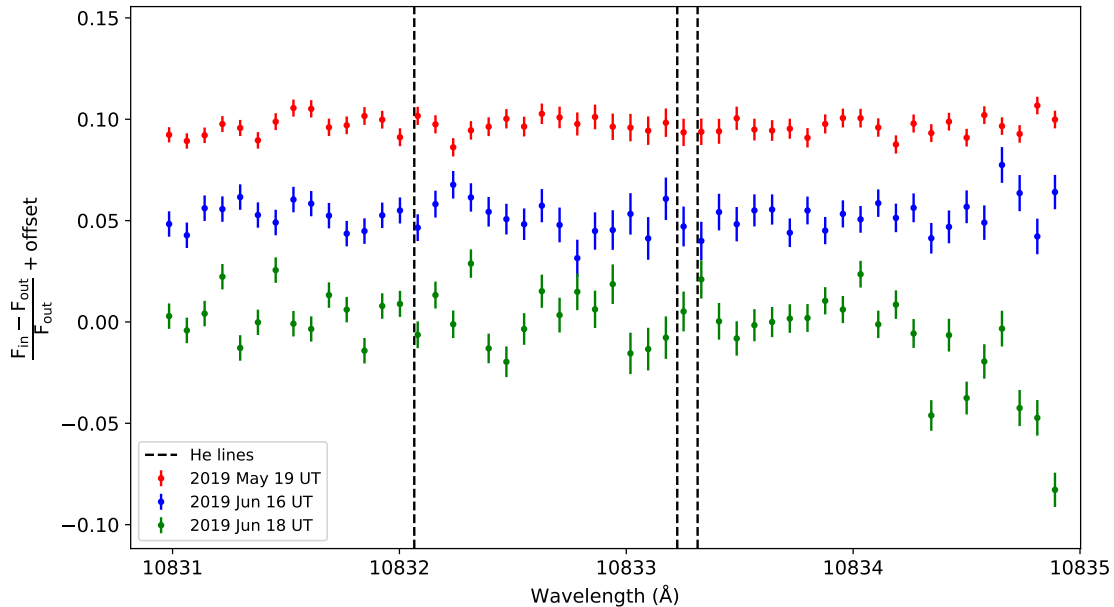
Figure 3.13: Transmission spectrum per night in the planetary rest frame. Exposures from 2019 May 19 UT, 2019 Jun 16 UT, and 2019 Jun 18 UT are depicted in red, blue, and green, respectively. Spectra from 2019 Jun 16 UT and 2019 May 19 UT are artificially offset by 0.05 and 0.1, respectively. The spectra do appear relatively flat, although there is deviation in error bars and variability. The spectrum from 2019 May 19 UT is the smoothest. It correspondingly contains the most number of exposures (5) and has the highest SNR.

As expected, there is no visible indication of helium absorption in any of these nightly transmission spectra. Figure 3.13 provides us insight into how the data affect our final transmission spectrum in Figure 3.12. Each spectrum is relatively flat, but the spectra from 2019 Jun 16 UT and particularly 2019 Jun 18 UT show much more variability and larger error bars. These nights contain only four and two exposures each, respectively, whereas five exposures were taken on 2019 May 19 UT. This may explain why the transmission spectrum from 2019 May 19 UT appears so smooth. In general, the exposures from 2019 May 19 UT have the highest SNR values as well (see Table 2.1), which provides further reasoning as to why the transmission spectrum from this night appears flatter than the other two.

Examining the spectra on a night-by-night basis is helpful because it affirms that there is no visible indication of helium absorption on any night. Moving forward, we revert to working with the final transmission spectrum (Figure 3.12) to determine the significance of these findings.

Chapter 4

Calculating and Contemplating Our Results

4.1 Setting an Upper Limit on Helium Absorption

No visible indication of planetary helium absorption can be seen in the master in-versus-out of transit spectrum (Figure 3.10) or the transmission spectrum (Figure 3.12). Still, we must calculate an absorption value and determine its statistical significance to definitely conclude that there is no detectable helium in the extended atmosphere of WASP-48b.

4.1.1 Calculating the Absorption Value

There are several methods used in the literature to calculate absorption from a transmission spectrum. The more traditional approach is to calculate the equivalent width (EW) of the absorption line, which is defined as the the width of a rectangle projected onto the spectrum whose height is equal to the level of the continuum flux (F_c) and whose total area corresponds to the area of the line profile (LeBlanc 2010). This is expressed mathematically as

$$W = \int_0^\infty \frac{F_c - F_\lambda}{F_c} \, d\lambda, \tag{4.1}$$

where F_λ is the flux of the line profile. In other words, the area of the rectangle $(W \times F_c)$ is equal to the difference between the continuum flux and line profile flux $(F_c - F_\lambda)$ integrated over all wavelengths.

While this is a perfectly viable option, we have elected to simply measure the average absorption depth over a narrow range of wavelengths centered on the two red components of the helium triplet (10833.22 and 10833.31 Å). Because the blue-most helium line (at 10832.07 Å) is often too weak to be detected (see Figure 4.6), we exclude this portion of the wavelength range in our calculation.

We have chosen this method for several reasons. First and foremost, it seems to be the most common method across the helium detections and nondetections in the literature to date (e.g., Nortmann et al. 2018; Salz et al. 2018; Alonso-Floriano et al. 2019). In particular, utilizing absorption depth allows us to calculate an effective planet radius at 10833 Å, which will be used in Chapter 5 to compare helium detections across exoplanets. Additionally, while EW measures are still used in the helium literature (e.g., Ninan et al. 2020; Kawauchi et al. 2022), because we do not visibly see any helium detection, utilizing a technique that seeks to characterize the area of the feature does not seem the most appropriate method.

Therefore, we simply measure the average absorption depth and associated error within the wavelength range 10833.10–10833.49 Å. The absorption depth is found to be -0.0030 ± 0.0050. We chose a 0.39 Å window following Alonso-Floriano et al. (2019) and Kirk et al. (2020) as closely as possible, who used a 0.30 Å and 0.43 Å bandpass, respectively. The range is ultimately dictated by the

width of each data point in our dataset. For example, if we wanted to narrow the range further by reducing our indices by one, the range would have been only 0.23 Å. We did test several different windows, and slightly increasing or decreasing the wavelength range did not meaningfully impact our final absorption value and error.

4.1.2   Deriving Significance

To measure the statistical significance, we compare the measured absorption of helium with the propagated error and normalized continuum flux. Note that the convention in transmission spectroscopy is to define absorption as a negative value (and emission as positive), with the normalized flux being equal to zero. We calculate the significance as

$$\text{significance} = \frac{x_i - \mu}{\sigma}. \tag{4.2}$$

Here, our "mean value", μ, is simply the value of the continuum flux (which is zero), because this is the value against which we need to compare the absorption. x_i is the measured helium absorption, and σ is the final error associated with the helium absorption. Because the propagated error represents one standard deviation, our final significance value indicates the number of standard deviations away from the mean the absorption is. If the significance value is greater than 3σ, the absorption is deemed significant, meaning we can claim a helium detection. This comes from the fact that at 3σ, 99.7% of the values lie within three standard deviations of the mean (the normalized flux). If the absorption is less than 3σ, there is enough chance that the "true value" is contained in the normalized flux. In other words, the absorption value could simply be zero, and thus no detection

can be claimed.

Inputting $x_i = -0.0030$ and $\sigma = 0.0050$ (with the mean defined as the normalized flux, $\mu = 0$) into Equation 4.2, we find a significance of 0.6σ. Because this is far within the 3σ required to claim a detection, we can now safely label this a nondetection of metastable helium in the atmosphere of WASP-48b.

4.2   The Empirical Monte Carlo Method

While the calculated absorption depth and corresponding statistical significance allows us to draw conclusions regarding the lack of helium detection, more robust measures that examine the contributions to the final transmission spectrum from individual exposures must be taken into account. For this, we turn to the empirical Monte Carlo (EMC) diagnostic described first in Redfield et al. (2008). This is a technique that aims to assess any underlying systematic errors in our analysis. These errors may include those arising from the data analysis itself, including stellar continuum removal, telluric corrections, and rest frame shifts, as well as systematic errors arising from astrophysical sources including stellar variability.

Addressing these errors is particularly important when using an instrument such as the HPF, which cannot observe any single target for any length of time, and instead relies on multiple observations over the course of many nights. Our own observations were taken from mid-May to late-June 2019, and therefore any night-to-night variability must be taken into consideration. Applying the EMC allows us to test whether certain exposures from different nights are contributing more than others to our final transmission spectrum. We do account for night-to-night variations in SNR by weighting each exposure by its inverse variance.

However, the other systematic errors mentioned previously, as well as further systematic errors that have been overlooked, will be evaluated by the EMC.

The idea behind the EMC is to apply our data analysis pipeline (detailed in Chapter 3) to a random subset of observations to arrive at a final absorption depth, and then conduct this random selection many times. Assuming no subset of exposures is skewing our overall result, the resulting histogram of absorption values should be centered around the absorption depth calculated in Section 4.1. To preserve the integrity of our analysis, a random selection of five in-transit and eight out-of-transit exposures is selected for each iteration, so that the ratio of in-to-out exposures in the EMC most closely matches the true ratio of all the in-transit exposures (11) to out-of-transit exposures (19). These numbers exclude the exposures that were discarded: 2019 Jun 18 10:52 UT and 2019 Jun 18 11:08 UT (detailed in Section 2.4), and 2019 Jun 16 05:43 UT and 2019 Jun 16 05:59 UT (detailed below in Section 4.2.1).

In addition to conducting the EMC for in-transit versus out-of-transit exposures ("in-out"), we also apply it to compare a random subset of in-transit exposures with the rest of the in-transit exposures ("in-in"). We do the same for out-of-transit exposures ("out-out"). These comparisons are done to ensure there is no systematic deviation within the in-transit or out-of-transit data. The absorption depth for both of these comparisons should be zero, signifying that there is no difference between various in-transit exposures (and the same for out-of-transit exposures). As in the "in-out" comparison, we preserve the in/out ratio for these two cases as closely as possible. Therefore, for the "in-in" comparison, we randomly select four exposures and compare them to the other seven, and for the "out-out" comparison, we randomly select seven exposures and compare them to the remaining 12.

We chose to apply the EMC for 330 iterations for each scenario ("in-in", "out-out", and "in-out") because this is the maximum possible number of combinations for the "in-in" scenario. We calculated the maximum number of possibilities in each case using the formula from Schroeder (1999):

$$\left(\frac{n}{k}\right) = \frac{n!}{k!(n-k)!},\tag{4.3}$$

where $\left(\frac{n}{k}\right)$ denotes the number of distinct subsets of k numbers from a given set of n numbers. This value is the lowest for the "in-in" scenario (330) and thus becomes the limiting factor.

To illustrate the EMC, we show an example of the "out-out" scenario in Figure 4.1. This figure is a histogram depicting the calculated absorption value (transmission signal) for the 330 different "out-out" iterations. Absorption is defined to be negative, and emission is defined to be positive. We see that in fact, the distribution is not quite centered on zero, but demonstrates a slight absorption. This is important to consider because it will affect our final absorption value for the "in-out" scenario. The final EMC will overplot all three scenarios to provide a visualization of where they fall relative to each other and relative to the point of zero transmission.

4.2.1 Discarding Two Exposures from 2019 Jun 16

Before illustrating the final version of the EMC, we must address our rational for excluding the in-transit exposures from 2019 Jun 16 05:43 UT and 2019 Jun 16 05:59 UT. In Sections 2.4, we noted that both have the lowest SNR values of our included sample (59.1 and 61.1, respectively). In Section 3.6, we noted that these two exposures were causing a "spike" of apparent emission close to where
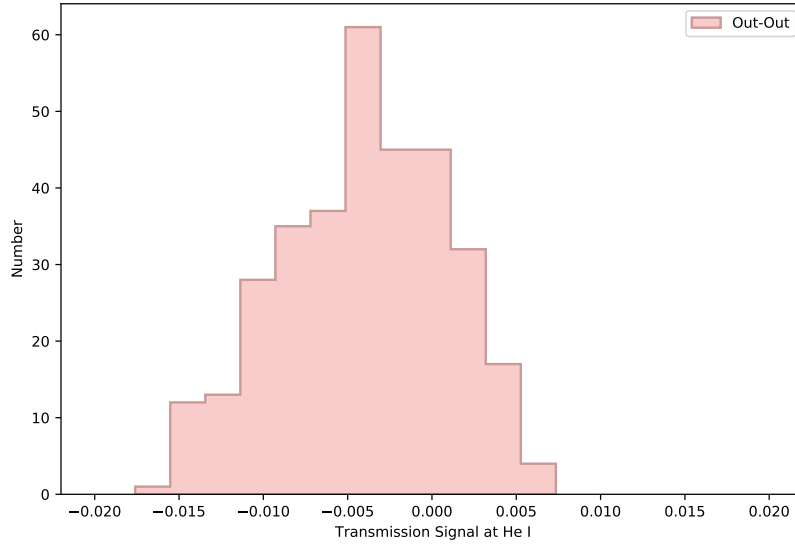
Figure 4.1: An example of the EMC method applied to the "out-out" scenario for 330 iterations. We do see that this scenario is not precisely centered on zero, which is important when interpreting our final absorption value.

the expected helium absorption lay, which resulted in a positive value for our calculated absorption depth. This suggested that for these two exposures, our data reduction was imperfect (i.e., imperfect telluric subtraction, stellar continuum removal, etc.). This argument is strengthened by examining the nature of the EMC when these exposures are included. Instead of a Gaussian shape centered around the absorption calculated in Section 4.1, there is a clear bimodal distribution in the "in-out" scenarios, as shown in Figure 4.2. This indicates that a small subset of exposures is largely skewing the data. When all exposures are included, the signal at the 10883 Å line is positive, meaning emission, not absorption, is measured in this case. Because the 2019 Jun 16 05:43 UT and 2019 Jun 16 05:59 UT spectra lead to the emission observed around the helium line, this suggests that they are the culprits here as well. Indeed, when these two exposures are removed, the bimodal nature of the "in-out" distribution disappears (see Figure 4.3).

Note that we did test removing other random in-transit exposures to see if they have the same large effect on the final EMC and absorption depth. Not only did removing other data not meaningfully change the absorption depth in the same way that these two exposures did, but it did not impact the overall EMC either.

It is for these reasons that we ultimately chose to exclude these data from our final transmission spectrum. Their low SNRs suggested they might be problematic, and the fact that they caused an emission "spike" in the transmission spectrum suggested that the data reduction pipeline was not working as well with these data as with the others. The fact that the EMC shows a bimodal distribution only when they are included provided the final evidence.

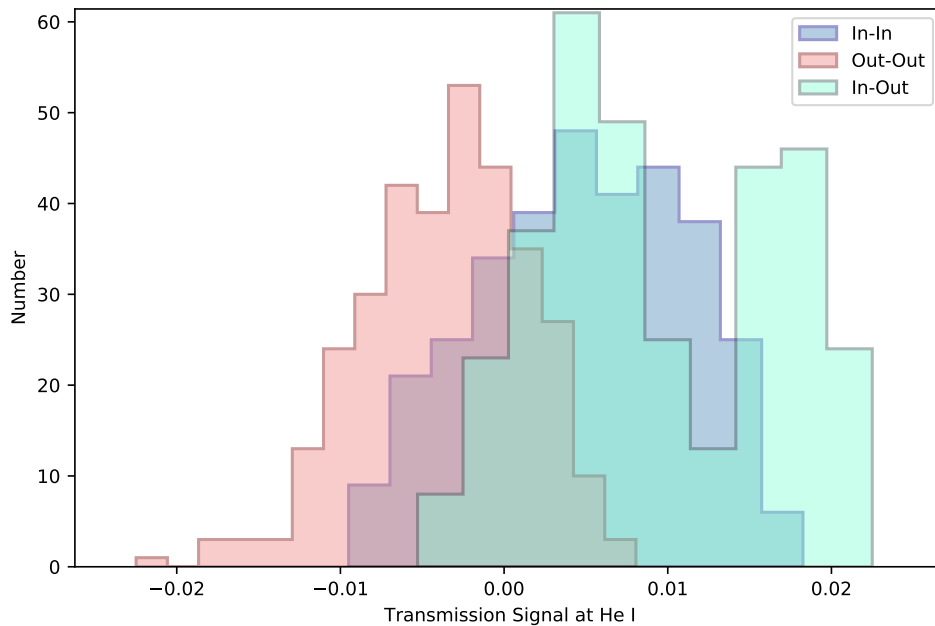**Figure 4.2:** The EMC method applied for 330 iterations in all three scenarios ("in-in", "out-out", and "in-out"). This version includes the exposures from 2019 Jun 16 05:43 UT and 2019 Jun 16 05:59 UT. The "in-out" data show a bimodal distribution, suggesting that a few transits are largely skewing the data when they are randomly selected. When the two exposures are removed, this distribution disappears (see Figure 4.3).

4.2.2 The Final EMC

Once the exposures from 2019 Jun 16 05:43 UT and 2019 Jun 16 05:59 UT are removed, the EMC is run for 330 iterations for all three scenarios. The final result is shown in Figure 4.3. The "in-out" scenario closely aligns with the "out-out" scenario; both are slightly skewed toward absorption (negative transmission signal values). The "in-in" scenario is more closely centered on zero absorption, though its shape is somewhat right-skewed. Though none of the scenarios are perfectly Gaussian and/or centered on zero absorption, this can be forgiven since there were only 330 iterations. In Redfield et al. (2008), this was done for thousands of iterations. We simply do not have enough exposures to run the EMC this many times without repeating combinations.

In addition, though the distributions do not perfectly align, there is no visual indication that the "in-out" data are significantly different from the "in-in" or "out-out" scenarios. (If this were the case, we would expect the green histogram to be significantly shifted to the left toward absorption.) This follows what we found for the final transmission spectrum in Figure 3.12. In addition, we can compare the calculated absorption and standard deviation from the transmission spectrum (black lines in Figure 4.3) to the mean and standard deviation of the "in-out" scenario of the EMC (magenta lines in Figure 4.3; see also Table 4.1). From the transmission spectrum, we measure -0.0030 ± 0.0050, and in the EMC, we measure -0.0024 ± 0.0055. Using Equation 4.2, we can calculate that the EMC absorption value is within 0.12σ of the calculated absorption value (vice versa, the calculated absorption value is within 0.11σ of the EMC value). Because the absorption and associated standard deviations are so close between the two methods, we can confirm that we correctly propagated error through the analysis
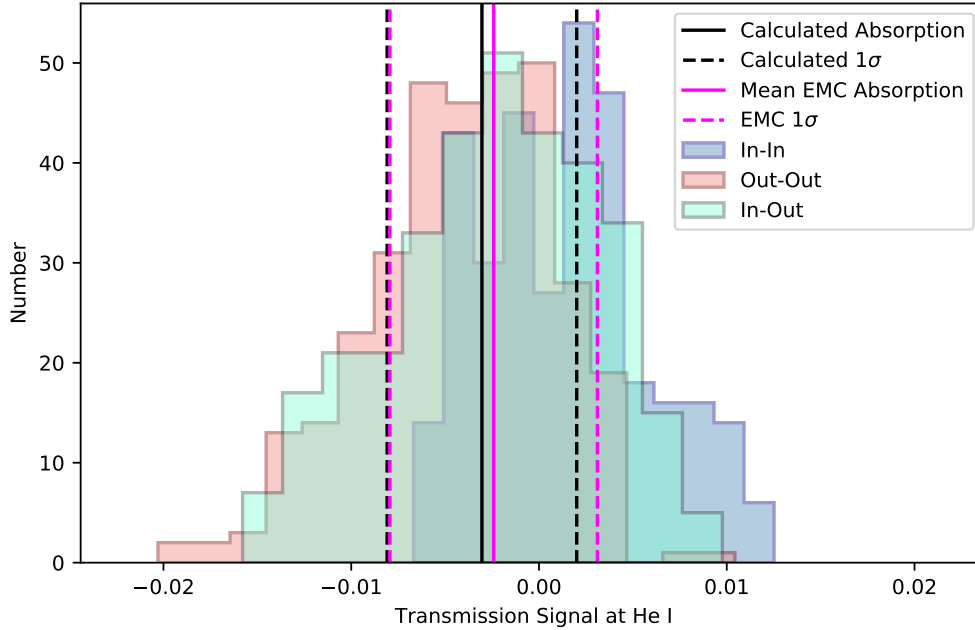
Figure 4.3: Final version of EMC, showing absorption depth at the 10833 Å helium line across randomly selected subsets of "in-transit" and "out-of-transit" exposures. The solid and dotted black lines depict the calculated absorption depth and associated error from Section 4.1. The corresponding magenta lines show the average absorption and associated error calculated in the EMC. The lines are close together, suggested we have correctly accounted for systematic errors in the data analysis.

and sufficiently accounted for all systematic errors. Thus, the EMC gives us a method to check our results from Section 4.1. We see a small, insignificant amount of absorption and thus cannot claim a helium detection.

4.3   The Oklopčić Model

Now that we have provided robust constraints on our observations, we would like to explore our nondetection by understanding the underlying physics driving the atmosphere of WASP-48b. To put our findings into context, we follow the model from Oklopčić & Hirata (2018), known hereafter as the Oklopčić model.

	μ	σ
In-In	0.0014	0.0044
Out-Out	-0.0040	0.0049
In-Out	-0.0024	0.0055

Table 4.1: Mean (μ) and standard deviation (σ) values for the "in-in", "out-out", and "in-out" scenarios from the EMC. Both the "out-out" and "in-out" scenarios show slight absorption, and the "in-in" scenario shows slight emission.

This was the first theoretical paper since Seager & Sasselov (2000) to discuss the promise of searching for metastable helium in exoplanet atmospheres, and the first to quantify predicted absorption signatures. The Oklopčić model is a one-dimensional model of an exoplanetary atmosphere containing hydrogen and helium, and it can be used to calculate the radial density profile of the 2^3S state and thus the helium absorption depth in a transmission spectrum.

The basis of the model is that an escaping atmosphere can be described by a steady-state, spherically symmetric isothermal Parker wind (Parker 1958). Though this model was originally derived for the wind in the solar corona, it is now commonly applied to exoplanet atmospheres. Parker realized that without an external pressure source, the solar corona could not remain in static equilibrium, because the pressure coming from the corona overwhelms interstellar pressure (Owen 2019). Parker argued that the only possible hydrodynamic solution is an outflow with low velocities close to the surface which gradually accelerate and become supersonic at an altitude known as the sonic point. This solution produces decreasing pressures and densities at large radii, with a velocity profile as a function of altitude/radius described by (Lamers & Cassinelli 1999):

$$\frac{v(r)}{v_s} \exp\left[-\frac{v^2(r)}{2v_s^2}\right] = \left(\frac{r_s}{r}\right)^2 \exp\left[-\frac{2r_s}{r} + \frac{3}{2}\right]. \qquad (4.4)$$

Here, r_s is the sonic point, or the location at which the gas speeds transition from

subsonic to supersonic velocities. It is given by

$$r_s = \frac{GM_{pl}}{2v_s^2},$$

(4.5)

where M_{pl} is the mass of the planet. v_s is the velocity at the sonic point (i.e., the speed of sound) and is defined as

$$v_s = \sqrt{\frac{kT}{\mu m_H}}.$$

(4.6)

Additionally, the density profile can be derived by combining Equation 4.4 with the equation for mass conservation,

$$\dot{M} = 4\pi r^2 \rho(r) v(r),$$

(4.7)

to find the density profile as a function of altitude/radius:

$$\frac{\rho(r)}{\rho_s} = \exp\left[\frac{2r_s}{r} - \frac{3}{2} - \frac{v^2(r)}{2v_s^2}\right].$$

(4.8)

Thus, we have analytical solutions to the density and velocity profiles of the exoplanetary atmosphere. These solutions are shown in Figure 4.4 for the two case study planets used in the paper, GJ 436b and HD 209458b. The density decreases asymptotically with altitude, while the velocity increases asymptotically with altitude. The main free parameters for these profiles are planetary radius and mass (M_{pl} in Equation 4.5), atmospheric composition (μ, in Equation 4.6), temperature of the thermosphere (T from Equation 4.6), and mass-loss rate ($\dot{M}$ in 4.7). Atmospheric composition is usually taken to be solar, with a 9:1 hydrogen to helium ratio. Thermosphere temperature instead of equilibrium temperature is
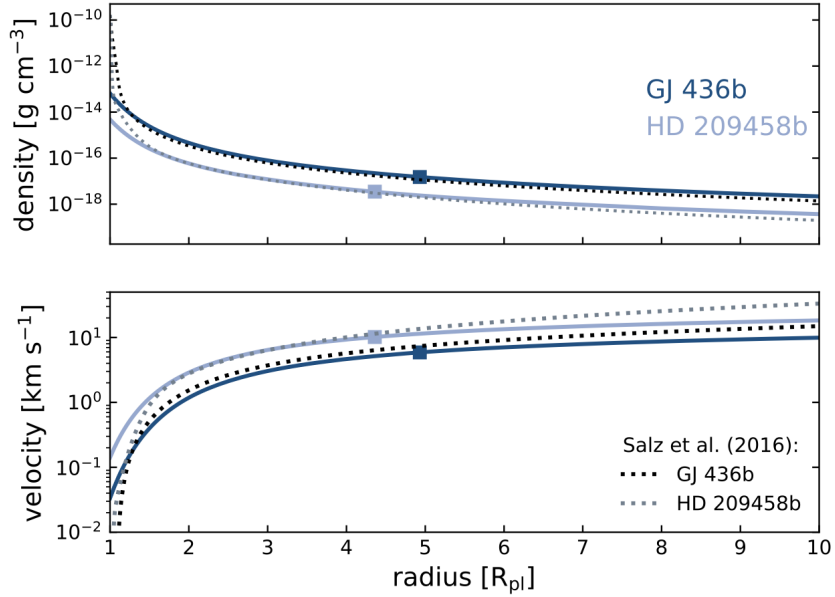
Figure 4.4: Analytic solutions to density and velocity profiles for GJ 436b (dark blue line) and HD 209458b (light blue line). These solutions are compared to a previous model from Salz et al. (2016), and the two give similar solutions. The density decreases asymptotically and the velocity increases asymptotically with altitude, which is given in units of planet radius. Figure 2 from Oklopčić & Hirata (2018).

used because the thermosphere undergoes a high amount of stellar radiation and is where atmospheric escape occurs.

However, neither thermosphere temperature nor mass loss rate can be derived from the model, and thus must be assumed. The high-energy stellar radiation is believed to be the driving force behind these parameters, and without this information, mass-loss rate estimates are usually considered to be an order-of-magnitude estimate at best (A. Oklopčić, private correspondence). Thus, our final model will include absorption depths at a range of thermosphere temperatures and mass-loss rates. Note that the thermosphere typically experiences high temperatures due to incoming stellar radiation; for example, Earth's thermosphere can reach temperatures of ~ 2770 K during the day (Prölss & Bird 2004). Hot Jupiters experiencing much greater stellar flux than Earth can be expected to have thermosphere tem-

peratures ranging anywhere from 5000 to 10,000 K (Oklopčić & Hirata 2018).

From the density and velocity profiles, population levels of hydrogen and helium atoms as a function of radius can be derived. Because the density of the thermosphere is generally low, local thermodynamic equilibrium cannot be assumed, and the factors that affect populations levels must be explicitly calculated, including photoionization, recombination, radiative decay, and collisional excitations (Oklopčić 2019). To do so, the following equation, which represents how the fraction of an ion changes with radius, must be numerically solved:

$$\frac{\partial f_{ion}}{\partial r} = \frac{1 - f_{ion}}{v} \Phi e^{-\tau_0} - \frac{0.9\rho}{1.3 m_H v} f_{ion}^2 \alpha_{rec}. \tag{4.9}$$

Here, Φ represents the photoionization rate, and α_{rec} is the recombination rate. One can see that the velocity profile is explicitly required in Equation 4.9, and τ_0 (signifying optical depth) requires the density profile and is defined as:

$$\tau_0 = \int_r^\infty (1 - f_{ion}) \rho(r) \, dr. \tag{4.10}$$

Equation 4.9 can be numerically solved to find the fraction of helium in the neutral versus ionized states, as well as the number density of free electrons. From there, the radial distribution of helium atoms in the neutral singlet versus neutral triplet state can be found by solving the following equations:

$$v\frac{\partial f_1}{r} = (1 - f_1 - f_3)n_e\alpha_1 + f_3 A_{31} - f_1\Phi_1 e^{-\tau_1}$$
$$-f_1 n_e q_{13a} + f_3 n_e q_{31a} + f_3 n_e q_{31b} + f_3 n_{H^0} Q_{31}, \tag{4.11}$$

$$v\frac{\partial f_3}{r} = (1 - f_1 - f_3)n_e\alpha_3 - f_3 A_{31} - f_3\Phi_3 e^{-\tau_3}$$
$$+f_1 n_e q_{13a} - f_3 n_e q_{31a} - f_3 n_e q_{31b} - f_3 n_{H^0} Q_{31}.$$
(4.12)

In these equations, the first term represents the recombination rate, with f_1 and f_3 indicating the fraction of helium in the singlet and triplet states, respectively, n_e indicating the number density of electrons, and α_1 and α_3 indicating the recombination rate coefficient of the singlet and triplet states, respectively. The second term represents the triplet-to-singlet radiative decay rate, where A_{31} is the associated Einstein coefficient (indicating the rate of transition from the triplet to singlet state due to radiative decay). The third term signifies the photoionization rate. Here, Φ is the associated photoionization rate coefficient and τ is optical depth. The final four terms take collisional excitation and de-excitation into account, with q_{13a}, q_{31a}, and q_{31b} denoting collision rate coefficients due to collisions with free electrons (where the subscripts a and b represent the S or P quantum number, respectively), and Q_{31} denoting the coefficient associated with de-excitation due to collisions with neutral hydrogen atoms.

A schematic of all these different transitions that are taken into account can be seen in Figure 1.8 in Section 1.4. Looking at this figure, it may be apparent that some transitions are ignored in these calculations. Notably, the radiative transition to the 2^3P state is ignored, because according to Oklopčić & Hirata (2018), this transition conserves the 2^3S state because any helium in the 2^3P state will simply decay back into the 2^3S state. Additionally, collision ionization is ignored based on assumptions of the thermosphere temperatures, as are direct collisions from the metastable state to the ground state because they are considered less

probable than collisions to the singlet excited state (Osterbrock & Ferland 2006).

From these equations, the column density of the metastable 2^3S state as a function of radius can be determined from the overall density profiles of the singlet, triplet, and ionized states. This is shown in two case planets, GJ 436b and HD 209458b, examined in Oklopčić & Hirata (2018), as seen in Figure 4.5. The density of metastable helium increases briefly, and then decreases radially from the planet. There is metastable helium present beyond the Roche lobe for GJ 436b, which can affect the line profile of the absorption feature, because symmetrical outflow can no longer be assumed (Oklopčić & Hirata 2018).
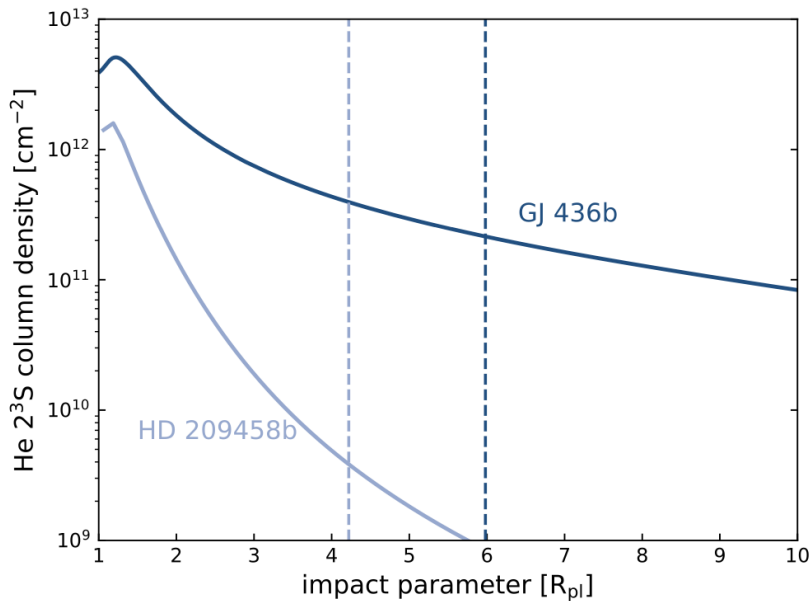
Figure 4.5: Column density of metastable helium as a function of planetary radius, calculated in Oklopčić & Hirata (2018). GJ 436b is a warm sub-Neptune orbiting an M-dwarf at 0.028 au (e.g., Butler et al. 2004), and HD 209458b is the aforementioned hot Jupiter orbiting a G-type star (e.g., Charbonneau et al. 2000) The dashed vertical lines represent the Roche limits of the planets. The density of metastable helium increases briefly, then decreases radially from the planet. In the case of GJ 436b, metastable helium is present past the Roche lobe. Figure 3 from Oklopčić & Hirata (2018).

Finally, this density profile is used to calculate the predicted metastable helium absorption by integrating the optical depth from the planetary radius to the stellar

radius. (Any absorption beyond the stellar radius will not be seen via transmission spectroscopy, which relies on the background stellar spectrum.) The optical depth is given by:

$$\tau_v(b) = 2 \int_b^\infty \frac{n_3(r)\sigma_0\Phi(\Delta\nu)r}{\sqrt{r^2 - b^2}} \, dr.$$

(4.13)

Here, n_3 is the number density of metastable helium, σ_0 is the absorption cross section, and $\Phi(\Delta\nu)$ is the Voigt line profile. The final result is the absorption calculated at mid-transit for the two case planets, GJ 436b and HD 209458b, by taking into account the gas only within the Roche limit as well as the gas at all radii. As shown in Figure 4.6, GJ 436b shows a deeper absorption profile than HD 209458b, and whether or not the Roche lobe is used as the upper limit on the integration of the optical depth impacts the final absorption feature.
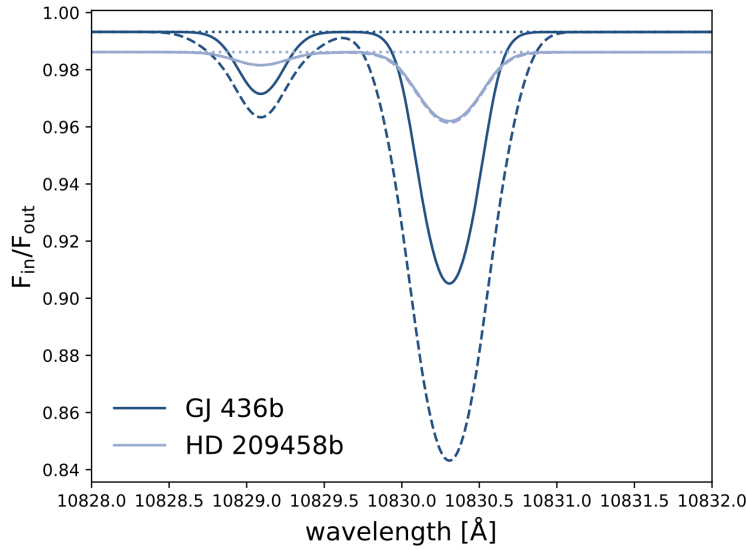
Figure 4.6: Final results of the Oklopčić model, as tested on two case planets, GJ 436b and HD 209458b. F_{in}/F_{out} denotes the ratio of the in-transit spectrum to out-of-transit spectrum. Note that wavelengths are given as air wavelengths. The solid lines indicate the absorption due to gas within the planet's Roche lobe, and the dashed lines indicate absorption at all radii. GJ 436b shows a deeper absorption feature than HD 209458b, suggesting it is a better target for observation. Because metastable helium extends beyond its Roche lobe, the absorption feature is more pronounced when considering gas at all radii. Figure 4 from Oklopčić & Hirata (2018).

The authors postulate why GJ 436b would be a better candidate based on their results. Their suppositions include the fact that a lower planetary gravitational potential suggests higher thermosphere densities, the ratio of EUV to mid-UV flux (Oklopčić 2019), and differences in helium and hydrogen ionizing flux. The first two possibilities will be described in more detail in Chapter 5.

4.4 Modeling WASP-48b

The Oklopčić model can be applied to any exoplanet to determine whether a helium absorption feature is expected. Indeed, this model has become the gold standard in helium detections and non-detections to date, and is frequently used to compare observations with theory (e.g., Kasper et al. 2020; Paragas et al. 2021; Zhang et al. 2021).

We compare the results of our transmission spectrum with the results predicted by the Oklopčić model. Input parameters include planetary mass and radius, atmospheric composition, thermosphere temperature, planetary mass-loss rate, and stellar spectra. Mass and radius are given in Table 1.2. Solar composition (9:1 hyrogen-to-helium ratio) and solar input spectrum are assumed. The spectrum is used because EUV flux drives atmospheric heating and escape. (For more information, see Section 1.4 or Chapter 5.) Unfortunately, it is difficult to a priori estimate the thermosphere temperature and mass loss rate without information about the high-energy luminosity of the star. Because of this, helium absorption for WASP-48b has been modeled over a range of parameters: 7000–10,000 K for the thermosphere temperature and $10^9 - 10^{11}$ g s^{-1} for the mass-loss rate. These ranges are typical of those predicted for close-in, highly irradiated exoplanets.

An example of the absorption signature predicted by the Oklopčić model at

a thermosphere temperature of 9500 K across the full range of mass-loss rates is shown in Figure 4.7. Note that in our transmission spectrum, we define the normalized continuum flux to be at zero, whereas the Oklopčić model defines it to be at one. In addition, in the model the flux is offset by the transit depth at all wavelengths. Recall that transit depth (δ) is defined as:

$$\delta = \left(\frac{R_p}{R_\star}\right)^2, \tag{4.14}$$

where R_p is the radius of the planet and $R_\star$ is the radius of the star. In the case of WASP-48b, $\delta = 0.00974$, and so in the original model, the normalized continuum flux is located not quite at 1, but at $1 - 0.00974$ or about 0.990. While this makes sense theoretically, in practice the transmission spectrum is a differential measurement across a narrow range of wavelengths sensitive to wavelength-dependent variations in absorption. For this reason, spectrographs such as the HPF are unable to detect the small wavelength-independent reduction in flux due to the transit. In order to accurately compare the model with the transmission spectrum, we therefore artificially add 0.00974 to the model's normalized flux to set the continuum at one, then subtract one to set the continuum flux at zero to match the observations.

One can see in Figure 4.7 that as mass-loss rate increases, so does the absorption depth of the helium feature. This makes sense, because as the mass loss rate increases, the density of helium atoms in the extended atmosphere increases, increasing the absorption signature. Likewise, we can examine how thermosphere temperature drives the absorption feature by plotting the range of temperatures across a single mass-loss rate (in this case, 10^{10} g s^{-1}). This is shown in Figure 4.8. From this figure, it appears that as thermosphere temperature increases

Figure 4.7: Oklopčić model overplotted with the final transmission spectrum, centered on the 10831–10835 Å range. This example depicts various mass-loss rates with a thermosphere temperature of 9500 K. Absorption signature increases with mass-loss rate at this thermosphere temperature.

from 7500–10,000 K, the helium absorption signature decreases. This phenomenon could occur because as the thermosphere temperature increases, a higher fraction of helium could become ionized, leading to a lower metastable helium abundance. (This of course, is just one possible explanation.) The notable exception in this case is the scenario modeled at 7000 K, where the combination of thermosphere temperature and mass-loss rate appears to not show any visible absorption. This is difficult to understand without examining the absorption depth across the full range of parameters (see Figure 4.9). When we inspect the full range of models, we see that this trend of decreasing absorption depth with increasing thermosphere temperature only holds for thermosphere temperatures 8000 K or greater. See discussion below for greater detail.
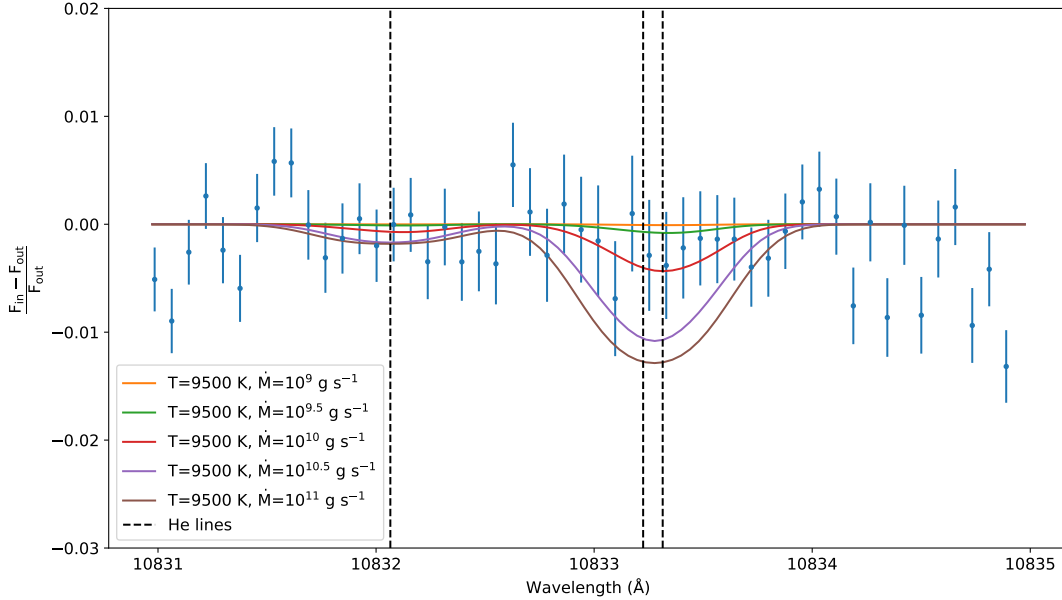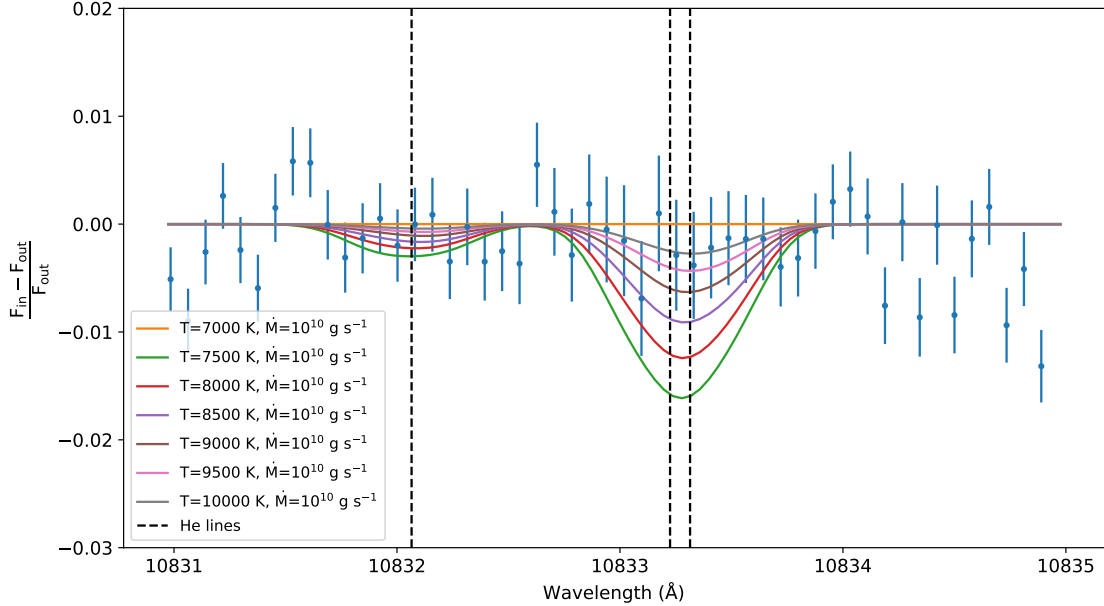
Figure 4.8: Oklopčić model overplotted with the final transmission spectrum, centered on the 10831–10835 Å range. This example depicts various thermosphere temperatures at a mass-loss rate of 10^{10} g s^{-1}. With the exception of the model at 7000 K, as thermosphere temperature increases, mass-loss rate decreases.

From examining these figures, one could make a back-of-the-envelope prediction that, say, our observations constrain the mass-loss rate to less than $10^{10.5}$ g s^{-1} at a thermosphere temperature of 7500 K (Figure 4.7) or a thermosphere temperature of at least 8500 K when the mass-loss rate is 10^{10} g s^{-1} (Figure 4.8). However, these trends may not hold true across all parameter ranges. We have already hinted that at a lower thermosphere temperature, absorption may not decrease with increasing thermosphere temperature. To more fully constrain the parameters of the extended atmosphere of WASP-48b, we can create a contour plot depicting the predicted absorption at all modeled thermosphere temperatures and mass-loss rates.

To do this, we must calculate absorption depth at each combination of param-

eter in the model. Because we have resolved line profiles in the model, we could choose to measure EW or peak absorption in the model, but we will use the same technique described in Section 4.1. Thus, we calculate the average absorption and associated error in the wavelength range 10833.12–10833.48 Å (this is as close to the range described in Section 4.1 as possible). We did this across all ranges of thermosphere temperatures and mass loss rates, and the results are shown in Figure 4.9. Note that because the model with a thermosphere temperature of 7000 K was modeled only up to a mass loss rate of 10^{10} g s^{-1}, this leaves a blank gap in the upper left corner of the contour plot.
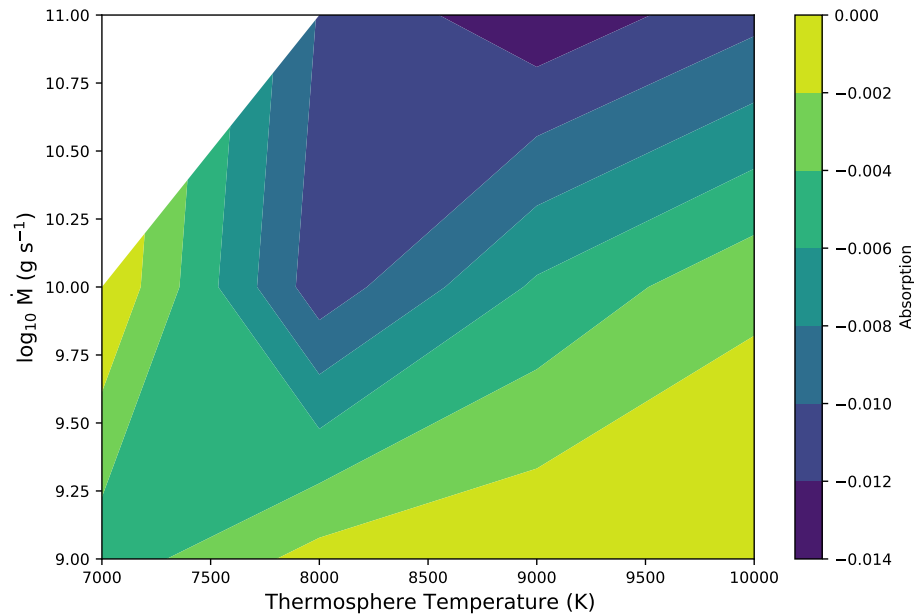
Figure 4.9: Average absorption depth across various mass-loss rates and thermosphere temperatures. Negative values represent absorption across the 10833.12–10833.48 Å range. This visualization suggests that the higher both the thermosphere temperature and the mass-loss rate, the greater the absorption value.

Figure 4.9 shows that at a thermosphere temperature greater than 8000 K, absorption increases with increasing mass-loss rate and decreases with increasing

temperature. The latter trend is particularly apparent between mass-loss rates of $10^{9.5}$ g s^{-1} and $10^{10.5}$ g s^{-1}. Interestingly, at thermosphere temperatures less than 8000 K, the trends are quite different. Absorption remains relatively constant with increasing mass-loss rate but increases with increasing temperature. Overall, the absorption is low at both low mass-loss rates and low temperatures.

We convert this plot from a measure of absorption to a measure of "sigma rejection" compared with our observations, shown in Figure 4.10. We use Equation 4.2 to compare the absorption value and associated error of the model with our calculated absorption value of 0.0030. If the model is 3σ or greater away from the calculated absorption, that mass loss rate and temperature combination can be safely rejected. This will allow us to constrain the mass-loss rate and thermosphere temperature more so than our model initially allowed.
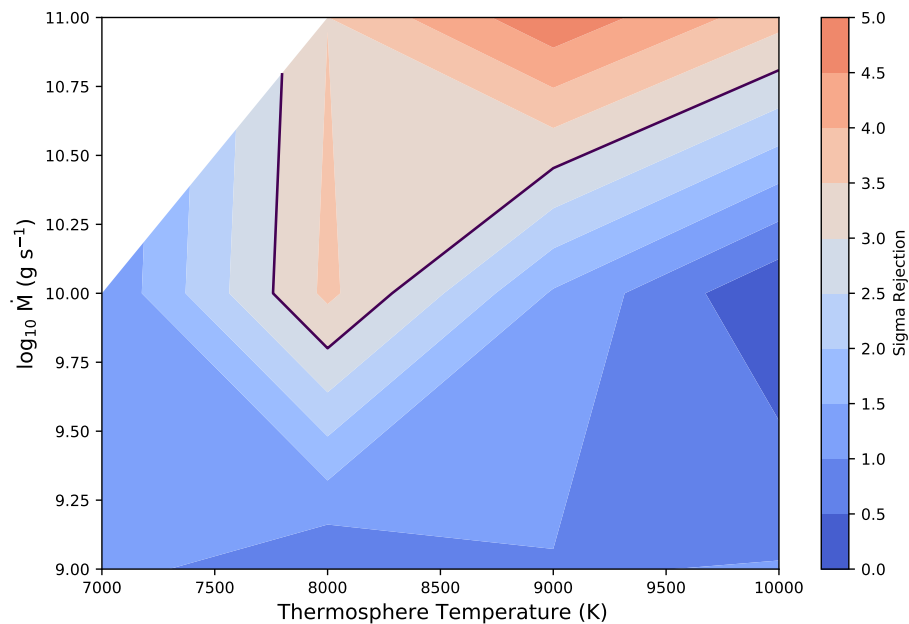
Figure 4.10: The number of standard deviations between the calculated and modeled absorption, measured across the full range of parameters. A line is drawn around the 3σ contour to show that anything higher than this value (red on the plot) can be rejected.

From Figure 4.10, blue contours represent a sigma rejection of less than 3σ, while contours in red represent a sigma rejection of greater than 3σ. The areas of the plot in red can be rejected. We see that this still leaves us with a large amount of degeneracy on the possible mass-loss rate and thermosphere temperature for the planet. WASP-48b could have a higher thermosphere temperature of 10,000 K with a mass-loss rate anywhere from $10^{11} - 10^{10.5}$ g s^{-1}. It could also have a mass-loss rate of less than 10^{10} g s^{-1} if its thermosphere temperature is about 8000 K. Only the highest mass-loss rate (10^{11} g s^{-1}) for WASP-48b can be rejected. This makes it difficult to draw concrete conclusions regarding the environment of the extended atmosphere of this hot Jupiter without further constraints on the calculated absorption value. Future observations would need to improve the error measurement, which could be done with more transits or a larger telescope.

4.5   Implications for lack of HeI detection

Though modeling WASP-48b with a range of mass-loss rates and thermosphere temperatures only allows partial constraints on these parameters, we can still confidently state that no escaping helium was detected in the atmosphere of WASP-48b. There could be many reasons for this. It may be that WASP-48b indeed has low amounts of high-energy radiation (EUV flux), and therefore there is simply not any atmospheric escape occurring in the extended atmosphere. Still, other factors may influence the absorption signature. It is possible that there could still be ongoing atmospheric escape, but the thermosphere temperature is too high to support this neutral helium population, and so most of the helium is already ionized (Owen 2019). Another possibility is that stellar variability leads to varying planetary outflows and thus a time-dependent absorption feature that

is only detectable during certain epochs. The stellar variability could be due to XUV variability, stellar winds, shear instability, or stellar flares (Zhang et al. 2022a). These possibilities will be discussed in more detail in Chapter 6.

Assuming our non-detection indicates that there is little-to-no current atmospheric escape on WASP-48b, we must ask ourselves if this conclusion makes sense in light of our current models and understanding of atmospheric escape. We should consider how various stellar and planetary parameters relate to the observed helium absorption. These parameters include those related to EUV flux (such as stellar activity, age, and rotation rate), but also include factors such as planetary surface gravity and semimajor axis. In Chapter 5, we dive into these factors, not just for WASP-48b, but for all exoplanets in which helium has been studied.

Chapter 5

Metastable Helium Detections: The Past and Future

From the results of Chapter 4, we can now conclude that no planetary helium absorption was detected in the transit observations of WASP-48b, and we will take this to mean that there is little to no ongoing atmospheric escape in the extended atmosphere of WASP-48b. In this chapter, we now turn to understanding this non-detection in the context of all helium detections and non-detections to date.

5.1   Helium and EUV Flux

Recall from Section 1.4 that atmospheric escape in exoplanets is thought to largely be due to high-energy radiation from the stellar corona, which causes the upper layers of the planet's atmosphere to heat up and escape. Photons at EUV wavelengths are the subset of high-energy radiation responsible for ionizing neutral helium, which then recombines to the metastable 2^3S state. In exoplanets, this photoionization-recombination pathway is thought to be the dominant mechanism behind populating the metastable helium state, more so than collisional excitation (Oklopčić & Hirata 2018), and thus EUV flux is thought to be the driving factor in the detection of helium in transmission spectra.

However, the main challenge of understanding helium detections and non-

detections comes from predicting stellar EUV flux, which is due to stellar magnetic activity in the corona and transition region between the corona and chromosphere (e.g., Nortmann et al. 2018; Oklopčić 2019). The radiation from stars in the EUV wavelength regime (typically defined as 100–912 Å) is difficult to observe due to its high absorption by the interstellar medium (Sanz-Forcada et al. 2011). To date, only one space mission, the *Extreme Ultraviolet Explorer (EUVE)*, has been commissioned for the purpose of studying stellar EUV emission. While it was able to collect data, it only examined nearby stars in the range 100–400 Å (Sanz-Forcada et al. 2011). Other proposed missions to directly study stellar EUV flux (France et al. 2020) have not yet come to fruition.

This leaves astronomers to simply predict stellar EUV flux by deriving scaling relationships between EUV flux and observable parameters such as age Sanz-Forcada et al. (2011), the stellar activity index log R'_{HK} (Sreejith et al. 2020; defined in Section 5.4.1), and stellar rotation rate (Wright et al. 2011). Assuming the legitimacy of these scaling factors, we can use these observable parameters as proxies for EUV flux and thereby determine whether there is indeed a correlation between EUV flux and helium absorption signatures. In this chapter, we will try to uncover these correlations by examining all helium detections and non-detections in the literature.

Because EUV flux is due to stellar magnetic activity, most of these parameters relate in some way to stellar activity. For example, age is often cited because magnetic activity (and therefore high-energy radiation) tends to decrease with stellar age. This was demonstrated in Ribas et al. (2005), who showed that the combined X-ray and EUV luminosities (henceforth denoted as XUV) of the Sun today are a factor of 100–1000 times lower than they were when the Sun was a young main-sequence star. From this work and others (e.g., Sanz-Forcada et al. 2011),

many older stars are deemed "quiet" and "inactive" with low XUV luminosities. Another factor that is often used as a proxy for magnetic activity is stellar rotation rate. In fact, some astronomers attest that decreasing high-energy luminosity over a star's lifetime could be be directly attributed to a star's decreasing rotation rate (Wright et al. 2011).

It is important to note that Oklopčić (2019) found that it is not simply overall EUV flux that should correlate with helium absorption, but the ratio of EUV flux to mid-UV flux (in order words, the "hardness" of the stellar spectra). As discussed in Section 1.4, while EUV flux is thought to populate the 2^3S state by initializing the photoionization-recombination pathway, the mid-UV flux directly ionizes the 2^3S state and therefore depopulates it. Thus, stars with low mid-UV flux (due to lower effective temperatures) but high EUV flux should optimize helium absorption. Oklopčić (2019) found that planets orbiting K-type stars are the most promising candidates given these constraints, and because of this finding, many helium searches to date have been around K stars.

In addition to correlations with stellar activity, other parameters such as semi-major axis and planetary surface gravity must be considered. Oklopčić (2019) found that helium absorption detections in exoplanets farther than 0.1 au from a K1 host star were unlikely, while the absorption signature may increase at distances less than 0.03 au. Additionally, the lower the planetary surface gravity, the denser the upper atmosphere will be, which could contribute to a lower helium absorption if collisions depopulate the 2^3S state (Oklopčić & Hirata 2018). These factors will be further discussed in Section 5.6.

5.2 Non-detection of helium on WASP-48b in context

Given the overview of parameters outlined in Section 5.1, we can first review whether our non-detection makes sense in light of these assumptions. Recall that WASP-48b orbits an old ($\sim$ 7.9 Gyr), slightly evolved F star. According to our discussion above, neither F-type stars nor old stars are ideal for the detection of helium. WASP-48's low log R'_{HK} value (-5.135) further supports the notion that this is an inactive star, and thus has low amounts of high-energy radiation being emitted from the corona. However, its high rotation rate ($v \sin i \sim 12.2$ km s^{-1}), particularly for a star of its age, suggests that perhaps its activity level could be higher than anticipated. Our non-detection in spite of this high rotation rate hints that perhaps rotation rate is not the best proxy for stellar activity.

Though the non-detection of helium in WASP-48b seems to not raise any questions in light of current understandings of EUV flux, stellar activity, and age, to more robustly investigate these relationships, the full suite of helium detections and non-detections should be considered. Only then can we draw conclusions about the observational veracity of these theoretical assumptions.

5.3 Helium in the literature

To the best of our knowledge, WASP-48b is the 30$^{\mathrm{th}}$ planet to be investigated for the detection of helium in its extended atmosphere. Table 5.1 gives an overview of all the helium searches by spectral type.

Table 5.1 shows that there have been more non-detections (20) than detections (10), and for spectral types F, G, and M, the majority of investigations have been

Spectral Type	Detections	Non-Detections
A	0	1
F	1	3
G	1	4
K	6	5
M	1	6
T Tauri	1	1
Total	**10**	**20**

Table 5.1: Distribution of helium detections and non-detections in the literature by spectral type. Each planet is counted only once. Most detections have been around K stars, though some have been around F, G, M, and T Tauri stars. There have also been more non-detections than detections, and these span across spectral types. Note that the number of K stars investigated outnumbers all the other spectral types.

non-detections. Only one planet orbiting a hot A-type star has been investigated (KELT-9b), and this was a non-detection (Nortmann et al. 2018). Notably, 11 out of the 30 planets investigated have been orbiting K stars, and of these, more than half have been detections. While this supports the finding from Oklopčić (2019) that K stars are the most promising candidates, the sample is still relatively small and skewed toward K stars to draw any final conclusion. In addition, there have been several non-detections around K stars, as well as detections around other spectral types, that suggest that the preference for planets orbiting K stars is by no means clear cut.

Several F, G, and M type stars have been investigated as well, and though there has been one detection around each type of star, respectively, the majority of the findings around these three spectral types have thus far been non-detections. The sole detection around an F-star was for the hot Jupiter HAT-P-32b (Czesla et al. 2022), which is interesting to note because it also has a rapid rotation rate ($v \sin i \sim 20.7$ km s^{-1}). It is, however, younger than the WASP-48b system (~ 3.8 Gyr). WASP-48b is one of three non-detections for planets around F-type stars. The only other planet orbiting an evolved star in this sample (WASP-12b,

Kriedberg & Oklopčić 2018) is also orbiting an F star, meaning two out of three of the F star non-detections are from planets orbiting stars coming off the main sequence. If the relationship between age and EUV flux is validated, this means that the F star sample is largely skewed.

Even two planets orbiting a T Tauri pre-main sequence star (Vissapragada et al. 2021) have been studied. In this system, helium was detected only in the planet (V1298d) closer to the star, which makes sense in light of the fact that the closer planet receives a higher amount of EUV radiation from the star, presumably driving higher levels of atmospheric escape.

There was one recently submitted paper detailing the discovery of TOI-3757 b, a hot Jupiter orbiting an M-dwarf (Kanodia et al. 2022), but this was excluded from our study because though the authors place an upper limit on helium absorption, they acknowledge that the helium line was directly over the bright OH telluric emission line and they were unable to derive any meaningful upper limit.

Overall, this sample is skewed toward K-type stars. Still, this is a much larger sample than when the first comparisons between helium detections began (Nortmann et al. 2018), and as more detections and non-detections are published, any correlations that truly exist should become clear.

The full tables of stellar and planetary parameters for each planet are found in Tables 5.2 and 5.3, respectively. These parameters have been taken from the literature. To the best of our knowledge, this is the most complete sample of helium literature to date. While there are some inhomogeneities in the way that the data are derived (e.g., some stellar ages are derived through isochrone fitting, while others are derived using gyrochronology), this must be used as a starting point to compare various parameters with helium absorption.

Table 5.2: Stellar parameters for exoplanets with published helium results. + indicates age was derived using log R'$_{\rm HK}$ value. * denotes gyrochronology age. Otherwise, age was derived via isochrones. **References:** 1. Anderson et al. (2017); 2.Piaulet et al. (2021); 3.(Kirk et al. 2020); 4.(Anderson et al. 2014); 5. Nortmann et al. 2018); 6.Bakos et al. (2010); 7.Allart et al. (2018); 8.Bouchy et al. (2005); 9. Boyajian et al. (2015); 10. Bonomo et al. (2017); 11.Barstow et al. (2017); 12.(Salz et al. 2018); 13. Hebb et al. (2009); 14. Turner et al. (2016); 15.Kriedberg & Oklopčić (2018); 16.Hartman et al. (2011a); 17. Paragas et al. (2021); 18. del Burgo & Allende Prieto (2016); 19. Melo et al. (2006); 20. Santos et al. (2004); 21. Queloz et al. (2000); 22. Southworth (2010); 23.Torres et al. (2008); 24. Alonso-Floriano et al. (2019); 25. von Braun et al. (2011); 26. Yee et al. (2017); 27. Bourrier et al. (2018a); 28. Zhang et al. (2021); 29. Gillon et al. (2014); 30. Lalitha et al. (2014); 31. Charbonneau et al. (2009); 32. Harpsøe et al. (2013); 33. Kasper et al. (2020); 34. Niraula et al. (2017); 35. Rodriguez et al. (2018); 36. Guo et al. (2020); 37. Ellis et al. (2021); 38. Howard et al. (2011); 39. Salz et al. (2015); 40. Bourrier et al. (2018b); 41. Lanotte et al. (2014); 42. David et al. (2019); 43. Vissapragada et al. (2021); 44. Kosiarek et al. (2019); 45. Bonfils et al. (2012); 46. Palle et al. (2020); 47. Gaudi et al. (2017); 48. Rice et al. (2019); 49. Prieto-Arranz et al. (2018); 50. Carleo et al. (2021); 51. Triaud et al. (2013); 52. Florian & Gallet (2020); 53. Triaud et al. (2015); 54. (Fossati et al. 2022); 55. West et al. (2016); 56. Casasayas-Barris et al. (2021a); 57. Gillon et al. (2016); 58. Agol et al. (2021); 59. Burgasser & Mamajek (2017); 60. Krishnamurthy et al. (2021); 61. Gillon et al. (2017); 62. Mann et al. (2020); 63. Zhang et al. (2022c); 64. Hartman et al. (2011a); 65. Czesla et al. (2022); 66. Barragán et al. (2022); 67. Zhang et al. (2022b); 68. Kawauchi et al. (2022); 69. Gan et al. (2022); 70. Hébrard et al. (2013); 71. Vissapragada et al. (2020); 72. Kanodia et al. (2022); 73. Enoch et al. (2011); 74. O'Rourke et al. (2014); 75. Sreejith et al. (2020); 76. Lam et al. (2017)

Planet	Spectral Type	$T_{\rm eff}$ (K)	Age (Gyr)	Radius ($R_\odot$)	Mass ($M_\odot$)	[Fe/H]	$v \sin i$ (km s^{-1})	log R'$_{\rm HK}$
WASP-107b	K6[1]	4425±70[2]	$6.9^{+3.7}_{-3.4}$[2]	0.67±0.02[2]	$0.683^{+0.017}_{-0.016}$[2]	+0.02±0.09[2]	2.5±0.8[1]	–
WASP-69b	K5[4]	4700±50[4]	1.10±0.15[4]*	0.813±0.028[4]	0.826±0.029[4]	+0.15±0.08[4]	2.2±0.4[4]	−4.54[4]
HAT-P-11b	K4[6]	4850±50[6]	$6.5^{+5.9}_{-4.1}$[6]	0.75±0.02[6]	$0.81^{+0.02}_{-0.03}$[6]	+0.31±0.05[6]	1.5±1.5[6]	−4.584[6]
HD 189733b	K2[8]	5050±50[8]	5.23.5[9]	0.76±0.01[8]	0.82±0.03[8]	−0.030.04[8]	3.5±1.0[8]	−4.5±0.007[75]
WASP-12b	F[13] (evolving)	6300±200	2±1[13]	1.57±0.07[13]	1.35±0.14[13]	+0.30[14]	2.2±1.5[13]	−5.500[14]
HAT-P-18b	K2[16]	4803±80[16]	12.4±6.4[16]	0.749±0.037[16]	0.770±0.031[16]	+0.10±0.08[16]	0.5±0.5[16]	–
HD 209458b	G0[18]	6071±20[18]	3.5±1.4[18]	1.20±0.05[18]	1.26±0.15[18]	+0.02±0.03[20]	3.75±1.25[21]	−4.92±0.029[75]
55 Cnc e	G8[25]	5172±18[26]	8.6±1.0[27]+	0.943±0.010[27]	0.905±0.015[27]	+0.35±0.1	<1.23±0.01[27]	−5.03[27]
GJ 1214b	M4.5[29]	3250±100[29]	5 – 10[30]+	0.2213±0.0043[29]	0.176±0.009[29]	+0.1±0.1[29]	<2.0[31]	–
GJ 9827d	K6[34]	4255±110[34]	10[49]	0.651±0.065[34]	0.659±0.060[34]	−0.28±0.12[34]	2±1[34]	–
HD 97658b	K1[36]	5192±122[36]	3.9±2.6[37]	0.746±0.034[36]	0.77±0.05[36]	−0.23±0.03[38]	0.5±0.5[38]	−4.975±0.025[38]
GJ 436b	M2.5[39]	3479±60[40]	6.5[39]*	0.449±0.019[40]	0.445±0.044[40]	−0.03±0.20[23]	0.33±0.091[40]	−5.09±0.001[75]
V1298b	T Tauri[42]	4970±120[42]	0.023±0.004[42]	1.345±0.056[42]	1.101±0.051[42]	–	–	–
V1298d	T Tauri[42]	4970±120[42]	0.023±0.004[42]	1.345±0.056[42]	1.101±0.051[42]	–	–	–
GJ 3470b	M1.5[44]	3652±50[44]	0.3 – 3[44]	0.48±0.04[44]	0.51±0.06[44]	+0.20±0.10[44]	–	−4.86±0.003[75]
KELT-9b	A0[47]	10170±450[47]	0.3[47]	2.362±0.075[47]	2.52±0.25[47]	−0.030±0.200[47]	111.4±1.3[47]	–
GJ 9827b	K6[34]	4255±110[34]	10[49]	0.651±0.065[34]	0.659±0.060[34]	−0.28±0.12[34]	2±1[34]	–
WASP-80b	K7[51]	4150±100[10]	1.601±0.202[52]*	0.571±0.016[10]	0.570±0.050[10]	−0.14±0.16[51]	3.46±0.35[51]	–
WASP-76b	F7[55]	6250±100[55]	5.3±2.9[55]*	1.73±0.04[55]	1.46±0.07[55]	+0.23±0.10[55]	3.3±0.6[55]	–
TRAPPIST-1b	M8[57]	2566±26[58]	7.6±2.2[59]	0.1192±0.0013[58]	0.0898±0.0023[58]	+0.040±0.080[57]	6±2[57]	–
TRAPPIST-1e	M8[57]	2566±26[58]	7.6±2.2[59]	0.1192±0.0013[58]	0.0898±0.0023[58]	+0.040±0.080[57]	6±2[57]	–
TRAPPIST-1f	M8[57]	2566±26[58]	7.6±2.2[59]	0.1192±0.0013[58]	0.0898±0.0023[58]	+0.040±0.080[57]	6±2[57]	–
HD 63433b	G2[62]	5640±74[62]	0.414±0.023[62]	0.912±0.034[62]	0.990±0.030[62]	+0.04±0.05[62]	7.3±0.3[62]	−4.39±0.05[62]
HD 63433c	G2[62]	5640±74[62]	0.414±0.023[62]	0.912±0.034[62]	0.990±0.030[62]	+0.04±0.05[62]	7.3±0.3[62]	−4.39±0.05[62]
HAT-P-32b	F[64]	6207±88[10]	3.8±1.5[64]	1.219±0.016[64]	1.160±0.041[64]	−0.04±0.08[64]	20.7±0.5[64]	−4.62[64]
HD 73583b	K4[66]	4511±110[66]	0.48±0.19[66]	0.65±0.02[66]	0.73±0.02[66]	0.00±0.09[66]	3.5±0.5[66]	−4.465±0.015[66]
TOI-2136b	M[68]	3373±108[68]	4.6±1.0[69]	0.3440±0.0099[68]	0.3272±0.008[68]	+0.02±0.14[68]	0.21±0.012[68]	–
WASP-52b	K2[70]	5000±100[70]	0.4±0.37[70]*	0.79±0.02[70]	0.87±0.03[70]	+0.03±0.12[70]	3.6±0.9[70]	−4.4±0.2[70]
WASP-127b	G5[76]	5620±85[76]	11.41±1.80[76]	1.39±0.03[76]	1.08±0.03[76]	−0.18±0.06[76]	0.3±0.2[76]	–
WASP-48b	F[73] (evolving)	5920±150[73]	7.9±2.0[73]	1.75±0.09[73]	1.19±0.05[73]	−0.12±0.12[73]	12.2±0.7[73]	−5.135[74]

Table 5.3: Planetary parameters for exoplanets with published helium results.

Planet	Radius (R_J)	Mass (M_J)	a (au)	T_{eq} (K)	log g_P (cm s^{-2})	δ_{He}	δ_{He}/H	Detection?
WASP-107b	0.94±0.02[1]	0.096±0.005[2]	0.055±0.001[1]	770±60[1]	2.49±0.05[1]	1.12±0.08[3]	47.6±3.7[3]	Yes
WASP-69b	1.057±0.047[4]	0.260±0.017[4]	0.04525±0.00053	963±18	2.726±0.046	0.74±0.11[5]	48.4±0.9[5]	Yes
HAT-P-11b	0.422±0.014[6]	0.081±0.009[6]	0.0530$^{+0.0002}_{-0.0008}$	878±15	3.05±0.06	1.06±0.09[7]	64.2±1.1[7]	Yes
HD 189733b	1.138±0.027[10]	1.123±0.045[10]	0.0313±0.0004[8]	1201±13[23]	3.3±0.03[10]	0.17±0.042[12]	39.3±0.4[12]	Yes
WASP-12b	1.825±0.091[10]	1.39±0.12[10]	0.02312$^{+0.00094}_{-0.00100}$[10]	2516±36[13]	2.99±0.03[13]	0.0021±0.0047[15]	0.17±0.00[15]	No
HAT-P-18b	0.995±0.052[16]	0.197±0.013[16]	0.0559±0.0007[16]	852±28[16]	2.69±0.05[16]	0.12±0.11[17]	7.5±0.3[17]	Yes
HD 209458b	1.359$^{+0.016}_{-0.019}$[10]	0.682±0.015[10]	0.0490±0.0020[18]	1459±12[22]	2.963±0.005[23]	0.29±0.18[24]	28.2±0.2[24]	Yes
55 Cnc e	0.1673±0.0028[27]	0.0251±0.00104[27]	0.01544±0.00005[27]	1990[28]	3.35±2.00	0.32±0.03[28]	6.8±0.1[28]	No
GJ 1214b	0.254±0.018[32]	0.0197±0.0027[32]	0.01411±0.00032[32]	604±19[29]	2.88±2.07	0.046±0.106[33]	1.6±0.5[33]	No
GJ 9827d	0.185±0.0125[35]	0.016±0.0057[35]	0.05615±0.00091[35]	680±25[35]	3.07±0.12[35]	0.34±0.20[33]	12.1±4.5[33]	No
HD 97658b	0.2055±0.009814[36]	0.0246±0.00173[36]	0.0831±0.0011[38]	751±12[37]	3.16±2.09	0.90±0.13[33]	40.2±6.4[33]	No
GJ 436b	0.366±0.014[41]	0.0799±0.0066[40]	0.0308±0.0013[41]	649±60[23]	3.17±2.13	0.26±0.09[5]	24.3±22.4[5]	No
V1298b	0.916±0.052[42]	—	0.1688±0.0026[42]	677±22[42]	—	0.036±0.101[43]	—	No
V1298d	0.572±0.040[42]	—	0.1083±0.0017[42]	845±27[42]	—	0.10±0.84[43]	—	Yes
GJ 3470b	0.346±0.029[44]	0.03958±0.004124[44]	0.0348±0.0014[45]	615±16[45]	2.91±2.04	0.93±0.44[46]	48.4±1.3[46]	Yes
KELT-9b	1.891±0.061[47]	2.88±0.84[47]	0.03462±0.00110[47]	4050±180[47]	3.30±0.11[47]	0.22±0.07[5]	23.1±10.2[5]	No
GJ 9827b	0.1407±0.0028[48]	0.0154±0.0015[48]	0.01880±0.00020[48]	1114±46[49]	3.29±2.12	1.66±0.90[50]	46.1±1.9[50]	No
WASP-80b	0.952±0.027[10]	0.540±0.036[10]	0.03427±0.00096[10]	825±19[53]	3.178±13[51]	0.11±0.06[54]	22.1±5.4[54]	No
WASP-76b	1.83±0.06[53]	0.92±0.03[53]	0.0330±0.0005[53]	2160±40[53]	2.80±0.02[53]	0.32±0.07[56]	19.3±3.6[56]	No
TRAPPIST-1b	0.09956±0.00125[58]	0.004323±0.000217[58]	0.01154±0.00010[58]	400±9[57]	3.03±1.71[58]	0.040±0.024[60]	1.2±0.3[60]	No
TRAPPIST-1e	0.0821±0.00125[58]	0.00218±0.0000[58]	0.02925±0.002500[58]	251.3±4.9[61]	2.90±1.38[58]	0.070±0.027[60]	2.0±0.4[60]	No
TRAPPIST-1f	0.09323±0.00116[58]	0.003269±0.00009[58]	0.03849±0.00033[58]	219.0±4.2[61]	2.97±1.38[58]	0.020±0.024[60]	0.9±0.2[60]	No
HD 63433b	0.192±0.009[62]	—	0.0719±0.0033[62]	969±13[54]	—	2.42±0.16[63]	—	No
HD 63433c	0.238±0.011[62]	—	0.1458±0.0101[62]	680±9[54]	—	1.82±0.14[63]	—	No
HAT-P-32b	1.789±0.025[10]	0.75±0.13[10]	0.03427±0.00042[10]	1786±26[64]	2.82±0.10[64]	0.83±0.04[65]	61.5±9.0[65]	Yes
HD 73583b	0.249±0.009[66]	0.0321±0.0107[66]	0.0604±0.0027[66]	714±21[66]	3.11±2.66[66]	1.32±0.35[67]	66.9±2.0[67]	Yes
TOI-2136b	0.20±0.0062[68]	0.015±0.0098[68]	0.0533±0.0015[68]	378±13[68]	2.98±2.80[68]	1.25±0.68[68]	70.8±24.4[68]	No
WASP-52b	1.27±0.03[70]	0.46±0.02[70]	0.0272±0.0003[70]	1315±35[70]	2.81±0.03[70]	0.083±0.051[71]	5.8±1.5[71]	No
WASP-127b	1.37±0.04[76]	0.18±0.02[76]	0.0520±0.0005[76]	1400±24[76]	2.33±0.06[76]	0.19±0.39[77]	4.4±0.8[77]	No
WASP-48b	1.67±0.1[73]	0.984±0.085[73]	0.0344±0.0026[73]	2035±52[73]	2.91±0.06[73]	0.15±0.49[73]	10.9±0.3[73]	No

References: 1. Anderson et al. (2017); 2.Piaulet et al. (2021); 3.(Kirk et al. 2020); 4.(Anderson et al. 2014); 5. Nortmann et al. (2018); 6.Bakos et al. (2010); 7.Allart et al. (2018); 8.Bouchy et al. (2005); 9. Boyajian et al. (2015); 10. Bonomo et al. (2017); 11.Barstow et al. (2017); 12.Salz et al. (2018); 13. Hebb et al. (2009); 14. Turner et al. (2016); 15.Kriedberg & Oklopčić (2018); 16.Hartman et al. (2011a); 17. Paragas et al. (2021); 18. del Burgo & Allende Prieto (2016); 19. Melo et al. (2006); 20. Santos et al. (2004); 21. Queloz et al. (2000); 22. Southworth (2010); 23.Torres et al. (2008); 24. Alonso-Floriano et al. (2019); 25. von Braun et al. (2011); 26. Yee et al. (2017); 27. Bourrier et al. (2018a); 28. Zhang et al. (2021); 29. Gillon et al. (2014); 30. Lalitha et al. (2014); 31. Charbonneau et al. (2009); 32. Harpsøe et al. (2013); 33. Kasper et al. (2020); 34. Niraula et al. (2017); 35. Rodriguez et al. (2018); 36. Guo et al. (2020); 37. Ellis et al. (2021); 38. Howard et al. (2011); 39. Salz et al. (2015); 40. Bourrier et al. (2018b); 41. Lanotte et al. (2014); 42. David et al. (2019); 43. Vissapragada et al. (2021); 44. Kosiarek et al. (2019); 45. Bonfils et al. (2012); 46. Palle et al. (2020); 47. Gaudi et al. (2017); 48. Rice et al. (2019); 49. Prieto-Arranz et al. (2018); 50. Carleo et al. (2021); 51. Triaud et al. (2013); 52. Florian & Gallet (2020); 53. Triaud et al. (2015); 54. (Fossati et al. 2022); 55. West et al. (2016); 56. Casasayas-Barris et al. (2021a); 57. Gillon et al. (2016); 58. Agol et al. (2021); 59. Burgasser & Mamajek (2017); 60. Krishnamurthy et al. (2021); 61. Gillon et al. (2017); 62. Mann et al. (2020); 63. Zhang et al. (2022c); 64. Hartman et al. (2011b); 65. Czesla et al. (2022); 66. Barragán et al. (2022); 67. Zhang et al. (2022b); 68. Kawauchi et al. (2022); 69. Gan et al. (2022); 70. Hébrard et al. (2013); 71. Vissapragada et al. (2020); 72. Kanodia et al. (2022); 73. Enoch et al. (2011); 74. O'Rourke et al. (2014); 75. Sreejith et al. (2020); 76. Lam et al. (2017) 77. dos Santos et al. (2020)

5.3.1   Quantifying Helium Absorption Across the Literature

As discussed in Section 4.1, there are several ways by which helium absorption is reported in the literature. The total absorption depth (typically presented as a percent difference between the in-transit and out-of-transit spectrum) is often used, as is the equivalent width of the helium profile. Another method is to measure the height of the opaque atmosphere at the 10833 Å absorption feature. First, an effective planet radius (R_{eff}) at the helium line is defined from Fossati et al. (2022):

$$\frac{R_{\mathrm{eff}}}{R_P} = \sqrt{\frac{\delta + c}{\delta}}, \tag{5.1}$$

where R_P is the planet radius, δ is the transit depth (calculated using Equation 4.14), and c is the absorption depth or upper limit. This equation, by inputting δ and c, allows you to find R_{eff} normalized to R_p and determine the change in transit depth at the helium line (δ_{R_P}). For example, if $\frac{R_{\mathrm{eff}}}{R_P} = 1.2$, then $\delta_{R_P} = 0.2$. Therefore, we calculate δ_{R_P} as

$$\delta_{R_P} = \sqrt{\frac{\delta + c}{\delta}} - 1. \tag{5.2}$$

This change in transit depth, δ_{R_P}, then, represents the height of an opaque atmosphere that causes R_{eff} to be greater than R_P at a given wavelength and produces the absorption signature in the transmission spectrum (Nortmann et al. 2018). It is in units of R_P, and so to compare δ_{R_P} across planets, it must be normalized.

The approach that has become standard in the literature is to normalize δ_{R_P} to the scale height, H_{eq}. This is the distance over which the atmospheric pressure

decreases by a factor of e, and it is derived from the ideal gas law and equation of hydrostatic equilibrium (Schroeder 1999). Scale height is given by

$$H_{eq} = \frac{k_B T_{eq}}{\mu g}, \tag{5.3}$$

where k_B is the Boltzmann constant, T_{eq} is the planetary equilibrium temperature, g is planetary surface gravity, and μ is mean molecular weight of the planetary atmosphere. Following Fossati et al. (2022), we set μ to be 1.3 times the mass of hydrogen. The authors arrived at this value by assuming a hydrogen-dominated atmosphere instead of a hydrogen and helium atmosphere, with the goal being to reduce error caused by uncertainties in the helium abundance. We recognize that assuming a standard value for μ across all planet types may be an over-generalization, but at this stage of exoplanet atmospheric characterization, it may not be prudent to be quick to assign varying μ values and introduce more variability into our results.

Another criticism of using scale height as the normalization factor is that it depends on planetary equilibrium temperature, which is simply the theoretical blackbody temperature of the planet and is derived by setting the incoming stellar flux equal to the flux emitted by the planet (Lissauer & de Pater 2013). Atmosphere (and along with that, the temperature of the thermosphere) is not considered. It has been argued that thermosphere temperature and equilibrium temperature are unrelated (A. Oklopčić, private correspondence) and that a scale height derived from equilibrium temperature is not the most appropriate normalization factor. A better option may be to use thermosphere temperature in place of equilibrium temperature, which would allow δ_{R_P} to be normalized against the scale height of the thermosphere. However, at this moment in exoplanet re-

search, the thermosphere temperatures of exoplanets are highly unconstrained, and adding this additional unknown variable into our equation would only lead to further uncertainty.

Therefore, though using scale height as the normalization factor is not without its limitations, at this moment it is the best option for exoplanet researchers. Additionally, it is widely utilized across the helium literature, making it easier to compare our findings with others.

5.3.2   The First Helium Comparison

The first paper in which multiple helium detections and non-detections were compared in order to uncover any correlation between absorption and high-energy radiation/stellar activity was Nortmann et al. (2018). This was the paper that introduced the δ_{R_P}/H_{eq} normalized metric, and this has continued to be used to this day. Nortmann et al. (2018) calculates δ_{R_P}/H_{eq} for the five published helium findings at the time, and plotted it against both the log R'_{HK} value and combined X-ray and EUV flux. The results are shown in Figure 5.1. At the time, only two helium detections were included (though it is interesting to note that the first helium detection in WASP-107b by Spake et al. (2018) had occurred earlier that year and was excluded from this figure), and these are indicated by black diamonds. Vertical arrows denote upper limits on helium detections in three other planets. The sample size is limited, but this was the first time that a relationship between helium and high-energy radiation/stellar activity was supported observationally. This figure also highlights the range of expected values for δ_{R_P}/H_{eq}. Typically, values of 40 or less are non-detections (WASP-48b is found to have a value of 10.9), while values of 60–100 are often detections.
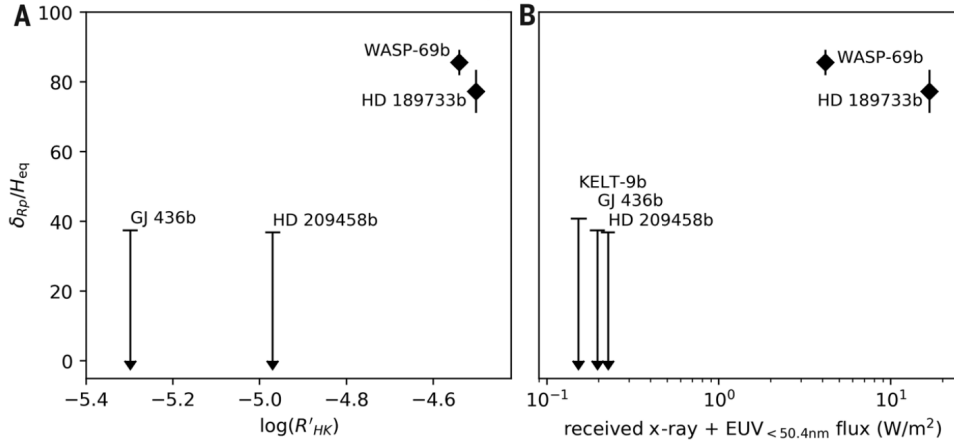
Figure 5.1: Normalized absorption altitude of helium (δ_{R_P}) normalized to scale height (H_{eq}) plotted against **A)** the stellar log R'_{HK} value and **B)** the combined X-ray and EUV flux. Vertical arrows indicate upper limits of helium (non-detections), and black diamonds indicate that helium was detected. Though the sample is limited, Nortmann et al. (2018) concludes that a relationship between helium absorption and both stellar activity and X-ray/EUV emission is hinted at by these figures. Adapted from Figure 4 in Nortmann et al. (2018).

Since this paper, many others have attempted to build upon it with an ever-growing sample of helium literature (e.g., Kasper et al. 2020; Orell-Miquel et al. 2022; Fossati et al. 2022). We do the same here, but in addition to plotting δ_{R_P}/H_{eq} against only high-energy flux, we also consider other parameters associated with stellar activity. These were outlined in Section 5.1 and will be fully investigated in the following sections.

5.4   Correlations between helium detections and stellar activity/EUV flux

To begin our discussion, we first aim to recreate the figures from Nortmann et al. (2018), shown in Figure 5.1. This will give us the greatest insight as to whether the posited relationship between high-energy radiation and helium ab-

sorption holds true in light of all the more recently published helium literature. In the following series of plots, as many planets from Table 5.3 are included in each graph as possible. Some parameters, such as the stellar log R'_{HK} value, are not found for all stars. Note also that any planet with an unknown mass is excluded (V1298b, V1298b, HD 63433b, and HD 63433c) because H_{eq} depends on planetary surface gravity, which cannot be calculated without planetary mass. We include both helium detections and non-detections in these figures, with non-detections denoted by a vertical arrow.

5.4.1 Stellar Activity Index (log R'_{HK})

We first examine the relationship between normalized helium absorption and the stellar activity index, log R'_{HK}. This is a commonly used metric first described in Noyes et al. (1984), and is defined as the ratio of emission in the cores of the Ca II H and K lines to the total stellar bolometric emission. The Ca II H and K lines originate in the chromosphere of the star, and so this is a useful indicator of stellar activity because it is a measure of the heating in the chromosphere associated with magnetic activity (Noyes et al. 1984). Furthermore, it is advantageous because these Ca II lines are in the optical regime (3933 Å and 3968 Å), meaning they are observable using ground-based telescopes (Sreejith et al. 2020). However, because the Ca II lines originate in the chromosphere, they do probe a spatially independent region from the corona and transition region, where EUV radiation originates (Nortmann et al. 2018; Sreejith et al. 2020).

Still, log R'_{HK} is widely used as a method to quantify the stellar magnetic activity: the higher the log R'_{HK} value, the higher the stellar activity. Recently, Sreejith et al. (2020) developed an analytical scaling relation between log R'_{HK}

and EUV flux, and this has further fueled our interest in uncovering any relation between log R'_{HK} and helium absorption.

Though the log R'_{HK} value is only available for half of the stars in our sample (15 out of 30), we plot the normalized helium absorption versus log R'_{HK} for the data that are available. The results are shown in Figure 5.2. There does appear to be a positive correlation between δ_{R_P}/H_{eq} and log R'_{HK}, with the exception of WASP-52b, supporting the notion that helium absorption and atmospheric escape is correlated with stellar activity. Our sample size is limited, however, and this should be measured across a larger sample before any conclusions can be made.
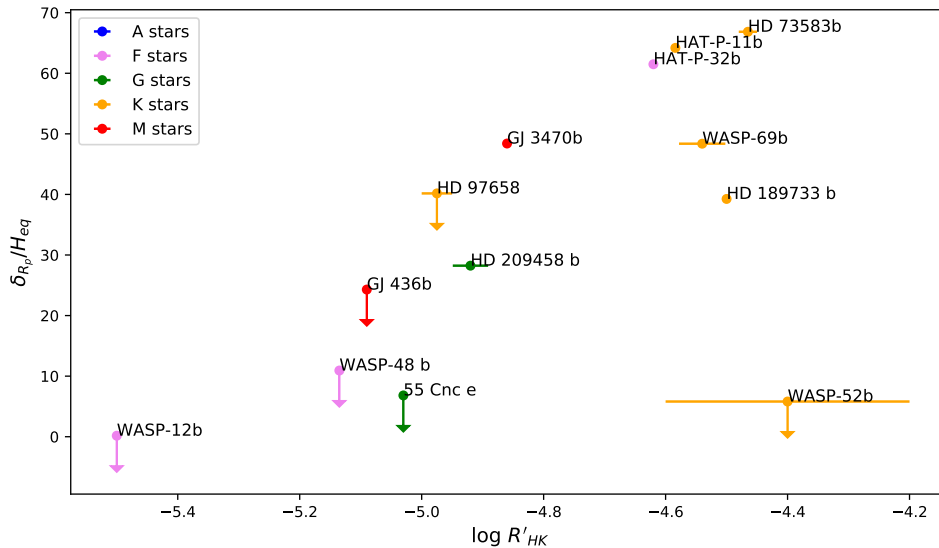

Figure 5.2: Normalized helium absorption versus log R'_{HK}, with spectral type designated by color. Non-detections (upper limits on helium absorption) are depicted with vertical arrows. With the notable exception of WASP-52b, there is a positive correlation between δ_{R_P}/H_{eq} and log R'_{HK}, hinting at a relationship between helium absorption and stellar activity. WASP-48b is in the lower left corner at a δ_{R_P}/H_{eq} value of ~ 10.9 and log R'_{HK} value of -5.135.

It is worth comparing this graph to the rightmost graph in Figure 5.1 from Nortmann et al. (2018). Notably, the δ_{R_P}/H_{eq} values are not equivalent between

them. For example, in our plot, δ_{R_P}/H_{eq} for WASP-69b is approximately 48, while in the Nortmann et al. (2018) figure, the value is closer to 85. This is not unusual. When searching the literature and reviewing comparable plots in various helium detection/nondetection papers, we found that though the relative trends in the shape and placement of data points in the graph were congruent, the δ_{R_P}/H_{eq} values themselves were not. This could be due to a variety of factors: a difference in how the helium absorption measure was taken from the literature, the use of different T_{eq} values, or varying assumptions about atmospheric compositions resulting in disparate μ values. Not enough information is given in these papers to follow each protocol thoroughly, and this is something that must be addressed as the exoplanet community continues to build comparative helium studies.

5.4.2   Predicted EUV Flux

The most likely parameter against which to measure δ_{R_P}/H_{eq} is EUV flux itself. However, as discussed in Section 5.1, EUV flux cannot be directly measured and instead is estimated using a variety of analytical and computational approaches (e.g., Sanz-Forcada et al. 2011; Linsky et al. 2014; Youngblood et al. 2017; Sreejith et al. 2020; Duvvuri et al. 2021). In addition, instead of helium absorption being compared directly with EUV flux, it is often compared more generally with X-ray or XUV flux (e.g., Zhang et al. 2021; Fossati et al. 2022).

For our purposes, unfortunately, it is difficult to estimate EUV flux for WASP-48b using many of these various approaches. For example, Linsky et al. (2014) uses the Ly-α line as a scaling factor with EUV flux, while Youngblood et al. (2017) extrapolates this further to use the width of the Ca II K line to derive a relationship between Ca II K and Ly-α. However, these spectral features have

not been reported for WASP-48. Enoch et al. (2011) does mention that the Ca II
H and K lines are absent from the stellar spectrum but does not provide any
quantitative data. Sanz-Forcada et al. (2011) uses an analytic expression to scale
EUV flux with stellar age, and Sreejith et al. (2020) does the same with log
R'_{HK}, but we measure helium absorption against both these measures directly (see
Section 5.5 for the relationship between δ_{R_P}/H_{eq} and age).

Furthermore, it is unwise to compare helium absorption against EUV flux val-
ues found in the literature, as these are all likely derived using different techniques.
Instead, we must find a homogeneous way to predict EUV flux. Many papers have
used X-ray luminosity either as a proxy or as a scaling factor for EUV luminosity
(Sanz-Forcada et al. 2011). A recent paper by Poppenhaeger (2022) made the
assertion that EUV luminosity can be derived from X-ray luminosity, but instead
of following one scaling law, it should follow two, based on iron abundances in the
stellar corona. This is because stellar EUV emission is dominated largely by line
emissions from bound-bound transitions, many of which are formed by iron in the
corona. High coronal iron abundance tends to occur in stars with high coronal
temperatures, and these high temperatures in turn are due to a higher activity
level. Therefore, an improved δ_{R_P}/H_{eq} versus EUV flux relation can be derived
by calculating EUV luminosity from X-ray luminosity and assuming either high
or low iron coronal abundances. This is shown in Figure 5.3, where the scatter in
the positive correlation between helium absorption and high-energy radiation is
reduced if this new method for deriving EUV flux is used.

Though X-ray spectra are needed to validate coronal iron abundances, placing
stars in the "high" versus "low" category can be estimated based on spectral type.
Poppenhaeger (2022) establishes that all M0 stars and later should be in the low
abundance category, as should hot stars and old stars, which are both expected
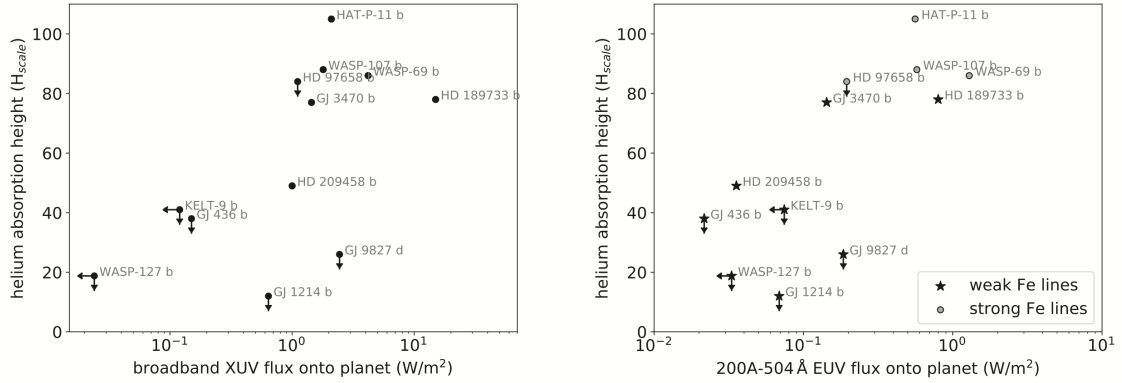
Figure 5.3: Normalized helium absorption versus XUV flux (right) and EUV flux (left). XUV measures are taken from the literature, while EUV flux is calculated using the scaling factors from Poppenhaeger (2022). The side-by-side comparison of these show an tighter correlation using the EUV flux scaling method. Adapted from Figure 8 in Poppenhaeger (2022).

to have low coronal temperatures. We follow this protocol and assign a high or low coronal iron abundance to the stars in our sample. We then calculate EUV luminosity using either the Poppenhaeger (2022) scaling relation for high iron abundances,

$$\log L_{\mathrm{high}} = 0.36 \times \log \frac{L_x}{10^{29}} + 28.19, \tag{5.4}$$

or the scaling relation for low coronal abundances,

$$\log L_{\mathrm{low}} = 0.72 \times \log \frac{L_x}{10^{29}} + 27.84. \tag{5.5}$$

We use X-ray luminosities found in the literature. Because these luminosities are only available for 17 stars in our sample, the entire sample from Table 5.2 is not included. The X-ray luminosity for WASP-48 is not available, but in order to include this in our discussion, we estimate its X-ray luminosity using a scaling

relation with age provided in Sanz-Forcada et al. (2011):

$$L_x = 1.89 \times 10^{28} \tau^{-1.55}, \tag{5.6}$$

where τ is the stellar age in Gyr. Though we chose to apply this scaling law for WASP-48, we did not apply this to all stars in our sample because the large uncertainties on age (see Section 5.5) will propagate into large uncertainties in the X-ray luminosity, which is not very helpful for our purposes. In the future, deriving X-ray coronal fluxes from the *XMM-Newton* DR10 Catalogue[1], following Poppenhaeger (2022), would be a prudent way to expand our sample size.

For now, we list X-ray luminosities and iron abundances for the stars in our sample in Table 5.4. Using Equations 5.4 and 5.5, we calculate EUV luminosities for these stars, and convert this into EUV flux using the inverse square law. From here, we plot the normalized helium absorption δ_{R_P}/H_{eq} against the EUV flux. This is shown in Figure 5.4, with spectral type delineated by color and non-detections by vertical arrows. Surprisingly, we see that there is more scatter in the data compared to Figure 5.3. While there does still appear to be an overall positive trend between helium absorption and EUV flux, the addition of more non-detections into this plot lessens the clarity of this relationship.

This finding raises the question of whether the relationship between helium absorption and atmospheric escape is more complicated than first presumed. There may be underlying factors regarding the nature of helium absorption that are lost when attributing it solely to incoming EUV flux. Of course, it is important to note that many assumptions went into the formation of our plot, which affects our interpretation of the data. We extracted X-ray luminosities in the literature

---

[1]https://xcatdb.unistra.fr/4xmmdr10/index.html

from various sources and extrapolated the high-versus-low coronal iron abundance assignments from Poppenhaeger (2022). It may be that there is significant inhomogeneity between X-ray measurements or that the delineation between high and low iron abundance is not straightforward. In addition, utilizing upper limits (which, depending on the error, may not hold much meaning) are not the most appropriate way to incorporate these data. Indeed, we see that many of the outliers are non-detections. A method such as the maximum likelihood estimation might be worth investigating in future work.

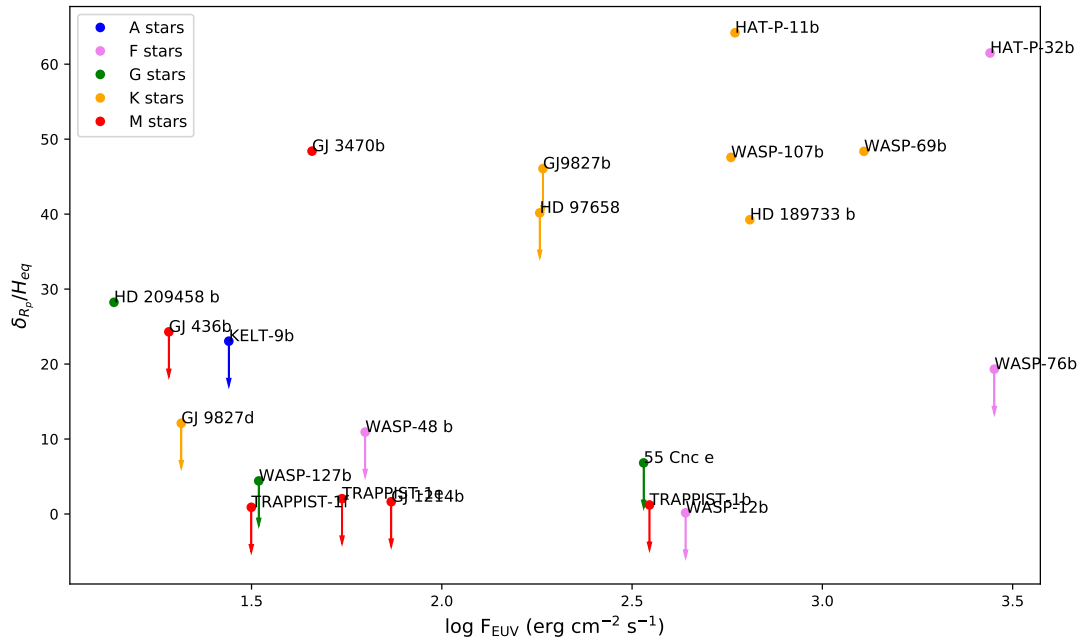**Figure 5.4:** Normalized helium absorption plotted against EUV flux. EUV flux is derived using the scaling factors detailed in Poppenhaeger (2022). Spectral type is designated by color, and non-detections are shown with vertical arrows. Error bars not included. WASP-48b is in the lower left portion of the plot. There does appear to be a correlation between absorption and EUV flux, but there is still a high degree of scatter.

Star	$\log L_X$ (erg s^{-1})	High/Low Iron Abundance
WASP-107	27.61[1]	High
WASP-69	28.11[1]	High
HAT-P-11	27.55[2]	High
HD 189733	28.18[2]	Low
WASP-12	< 27.58[2]	Low
HD 209458	< 26.40[2]	Low
55 Cnc	26.65[2]	Low
GJ 1214	25.91[2]	Low
GJ 9827	26.81[3]	Low
HD 97658	27.21[3]	High
GJ 436	26.04[1]	Low
GJ 3470	26.71[1]	Low
KELT-9	< 26.4[3]	Low
WASP-76	28.30[4]	High
TRAPPIST-1	26.61[5]	Low
HAT-P-32	28.36[6]	High
WASP-127	27.0[3]	Low
WASP-48	26.9[7]	Low

Table 5.4: X-ray luminosity and iron coronal abundances for host stars of helium studies. With the exception of WASP-48, X-ray luminosity is taken from the literature and is not available for the entire sample from Table 5.2. Iron coronal abundance is determined following Poppenhaeger (2022) (see text). **References:** 1. Foster et al. (2021); 2. Salz et al. (2016); 3. Poppenhaeger (2022); 4. Casasayas-Barris et al. (2021a); 5. Wheatley et al. (2017); 6. Czesla et al. (2022); 7. Sanz-Forcada et al. (2011)

5.5 Correlations between helium detections and other parameters

Though Figure 5.4 did not depict a clear relationship between helium absorption and EUV flux, we do still wish to examine other parameters related to stellar activity that may offer insight into any trends in atmospheric escape. In this section, we dive into various parameters that may be correlated with high-energy stellar radiation. Our goal here is to do a broad survey of other parameters be-

sides log R$'_{HK}$ and EUV flux that may be used to predict helium absorption and to identify promising targets in the future.

5.5.1   Stellar Age

As discussed in Section 5.1, stellar age is important because it has been shown that high-energy radiation decreases over the course of a star's lifetime (e.g., Sanz-Forcada et al. 2011). If this is true, we would expect to see a general trend of decreasing helium absorption with increasing stellar age. Figure 5.5 depicts δ_{R_P}/H_{eq} values plotted against stellar age, with different spectral types delineated by color. This figure does not depict any clear trends between helium absorption and age, although there may be correlations that are hidden by the large error bars on many of the stellar age values. Note though, that non-detections (depicted with vertical arrows) are occurring not only in planets orbiting old stars, but around host stars of all ages, even in K stars that are as young as 0.4 Gyr (WASP-52b). This is surprising because the younger the star, the higher the expected EUV radiation. The other youngest non-detection is around an A-type star (KELT-9b), but this is perhaps not as surprising given that hot stars emit a lower fraction of their bolometric luminosity in the UV compared to cooler stars (West et al. 2004).

Another confounding factor to consider is how age was determined. Most of the age values given in Table 5.2 were determined using isochrones, which are theoretical evolutionary tracks of populations of stars on the Hertzsprung-Russell (HR) diagram that used to determine stellar age LeBlanc (2010). However, some ages were calculated using gyrochronology (based on a star's rotation rate), and others were calculated empirically based on the stellar log R$'_{HK}$ value. Because these different techniques can yield vastly different estimates in a star's age (see

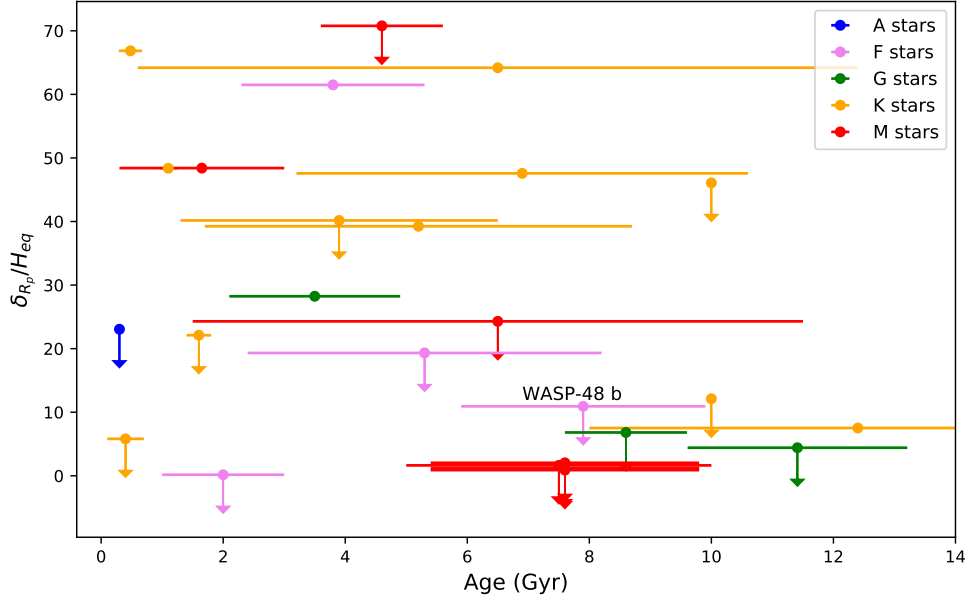Section 1.5), this introduces another source of error in the plot.

Figure 5.5: Normalized height of helium absorption versus stellar age. Spectral type is designated by color, and WASP-48b is singled out at an age of 7.9 Gyr and δ_{R_P}/H_{eq} of 10.9. No clear correlation can be seen, though the uncertainties on stellar age prevent any meaningful insight from being gleaned.

5.5.2   Stellar Rotation Rate

The next observable parameter to consider is stellar rotation rate, most commonly seen in the literature as $v \sin i$. Because often the inclinations (i) of the stellar system are unknown, the rotational velocity v cannot fully be constrained. Instead, we measure v projected onto our line of sight ($v \sin i$). For transiting exoplanets, it is safe to assume that i is close to 90° if we assume that the stellar rotation inclination, planetary rotation inclination, and planetary orbit inclination are all aligned. This makes $v \sin i$ a reasonable estimate for stellar rotation rate. Stellar rotation rate is correlated with stellar activity (e.g., Wright et al. 2011),

and so we would expect that the higher the rotation rate, the higher the stellar activity, and thus the higher the EUV flux and helium absorption. However, as with the case for age, we do not see a clear relationship when we plot these parameters against each other, as shown in Figure 5.6. In this figure, there are two fast-rotating outliers, WASP-48 and another F-type star, HAT-P-32. KELT-9b, the A-type star, was excluded from this plot because it is an even greater outlier, with a $v \sin i$ of more than 111 km s^{-1}. Notably, no helium was detected in KELT-9b, but it was detected in the other fast rotator, HAT-P-32. Even so, no trend can be seen in the rest of the data.
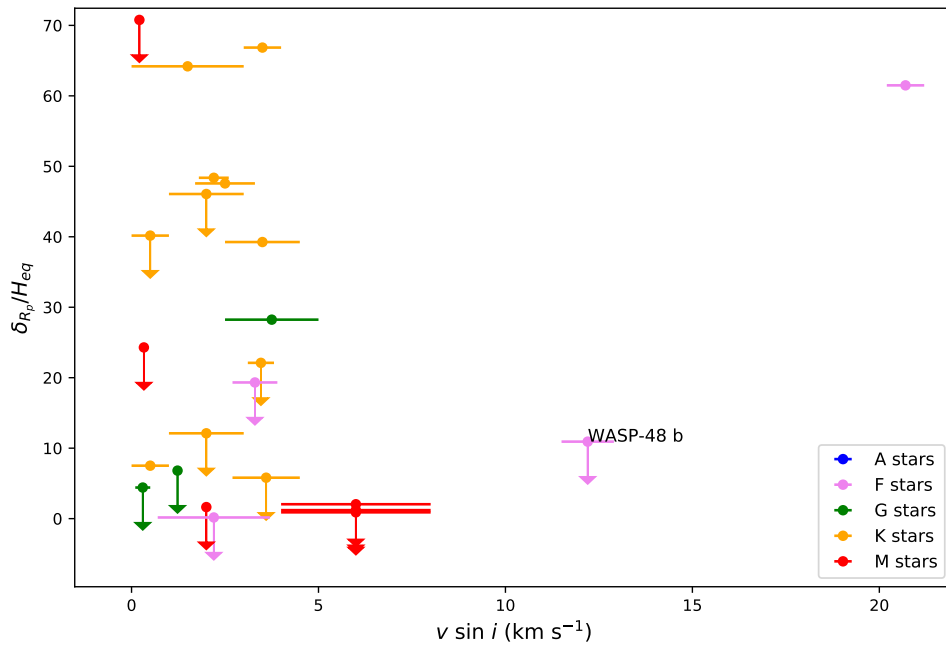

Figure 5.6: Normalized height of helium absorption versus stellar rotation rate, with spectral type designated by color. WASP-48b is one of the outliers with a high stellar rotation rate of 12.2 km s^{-1}. Still, excluding the two fast-rotating F-type stars, no clear relationship between $v \sin i$ and helium absorption is present.

5.5.3   Stellar Metallicity

In addition to age and rotation rate, stellar metallicity may be an important factor to consider because it may affect how quickly a star's rotation rate decreases over its lifetime (Amard & Matt 2020). Metal-rich stars are thought to "spin-down" faster, which may suggest for our purposes that planets orbiting older metal-rich stars experience lower EUV flux and helium absorption. However, the authors acknowledge that the relationship between activity, rotation rate, and metallicity is not always straightforward, because oftentimes older metal-poor stars (though they rotate faster than their metal-rich counterparts) actually demonstrate lower magnetic activity levels (Amard & Matt 2020). This suggests that there may not be as clear-cut a relationship between these factors and helium absorption as might be presumed from a bird's eye view. Indeed, no trends between δ_{R_P}/H_{eq} and [Fe/H] (the standard indicator of metallicity) are seen in Figure 5.7.

From Figures 5.5, 5.6 and 5.7, it is unclear how stellar age, rotation rate, and metallicity tie in with planetary atmospheric escape and metastable helium detection. Though these parameters all do correlate with stellar activity, it may be that the relationship is too indirect to affect how the stellar EUV flux impacts the planetary system. On the other hand, there may be a correlation that is undetectable given our current sample, uncertainties, or methodologies.

5.6   Planetary correlations to consider

Much of this chapter has been focused on stellar properties driving high-energy radiation. However, there are some planetary parameters that can affect atmospheric escape, and these must also be addressed.
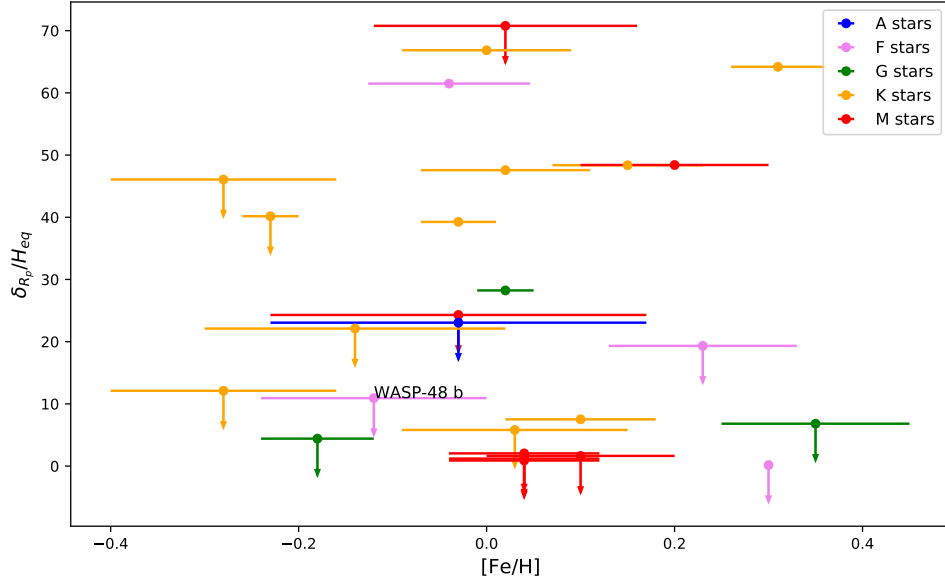
Figure 5.7: Normalized helium absorption versus host star metallicity, with spectral type designated by color and upper limits by vertical arrows. WASP-48b is labeled at an [Fe/H] of −0.12. No relationship between these parameters is visibly seen here.

5.6.1   Semimajor Axis

Because flux received by the planet inherently depends on its distance from the host star, semimajor axis should be investigated, as stars farther from their host stars will receive less high-energy radiation. As mentioned in Section 5.1, Oklopčić (2019) found that for K1 stars, it was very unlikely to for any helium absorption to be detected in stars at a distance greater than 0.1 au, while an increase in absorption may be expected for planets closer than 0.03 au. For stars of other spectral types, these values do not hold true, but we may still expect the same trend of a drop-off in helium absorption at a given semimajor axis threshold. We investigate the relationship between normalized helium absorption and semimajor axis in Figure 5.8. Though all helium studies are shown in this

graph, we must only compare within each spectral type. Still, no correlations are visually apparent. For example, within K stars, the only planet at a distance less than 0.03 au is a non-detection (GJ 9827b), and there is a high amount of scatter in helium absorption as semimajor axis increases.
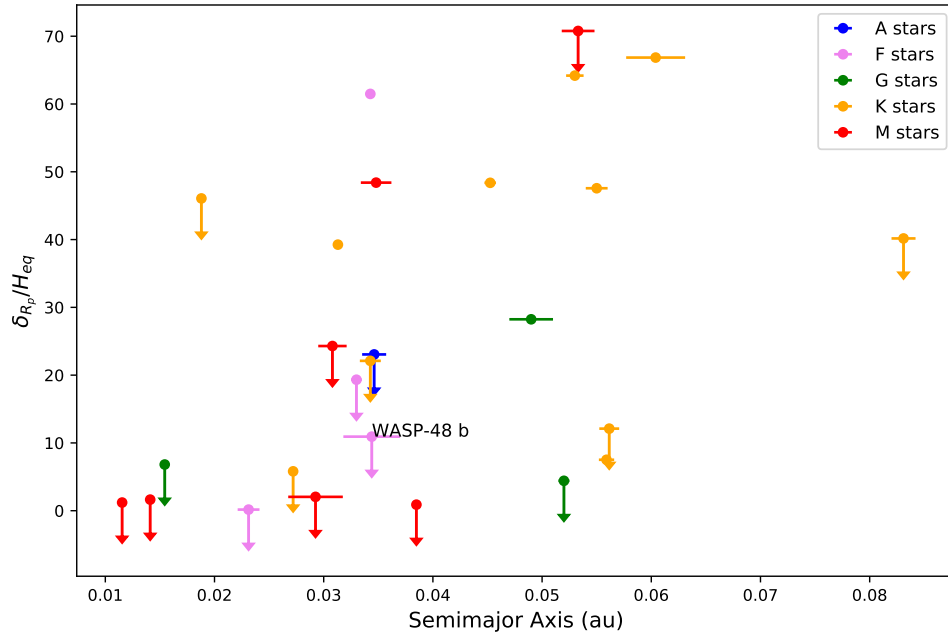

Figure 5.8: Normalized helium absorption versus semimajor axis. Spectral type is delineated by color and non-detections by vertical arrows. WASP-48b is labeled at 0.0344 au from its host star. Comparing within each spectral type (particularly K stars), no clear trends are revealed.

5.6.2   Planetary Surface Gravity

The final parameter we consider is planetary surface gravity, which is important because planets with lower gravitational potential may be more at risk for atmospheric escape, leading to a deeper helium absorption feature (Oklopčić & Hirata 2018). With this in mind, we might expect a higher helium absorption feature in planets with lower surface gravities. We investigate this claim in Fig-
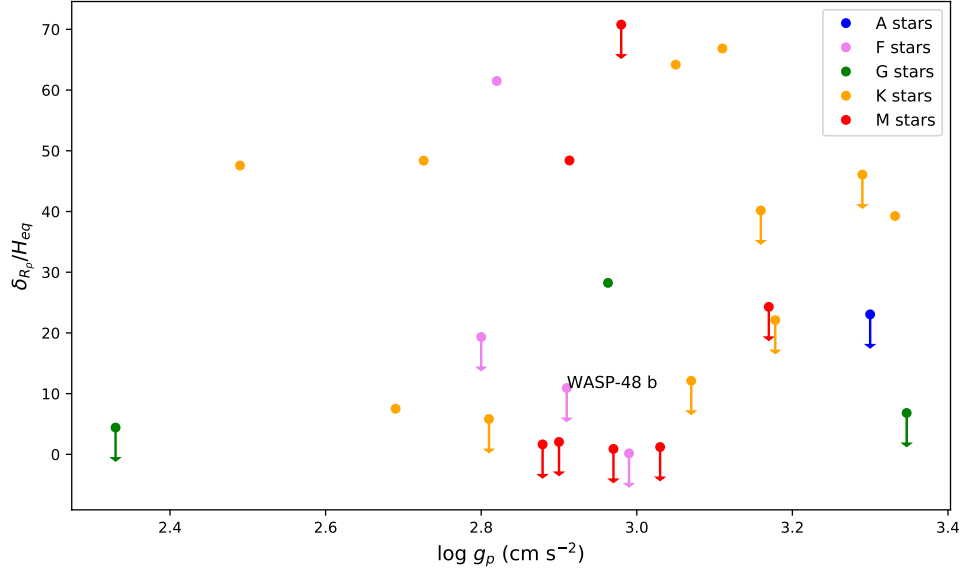
Figure 5.9: Normalized helium absorption versus planetary surface gravity. Error bars not included. WASP-48b is labeled with $\log g_P \sim 2.91$. Spectral type is delineated by color and non-detections by vertical arrows. No clear relationship is seen.

ure 5.9, and do not find any such relationship. This is corroborated by Fossati et al. (2022), who also did not find any correlation between helium absorption and planetary surface gravity.

5.7   Summary of trends

Surprisingly, we found no clear trends with helium absorption across almost all the considered parameters, including stellar age, rotation rate, metallicity, planetary semimajor axis, and planetary surface gravity. We did find a positive relationship between absorption and the $\log R'_{\mathrm{HK}}$ values, but this sample size was limited. EUV flux, which is widely believed to be the driver of atmospheric escape and helium absorption, did not demonstrate as clear a trend as $\log R'_{\mathrm{HK}}$ when all available helium studies were included, though there did appear to be

some correlation.

To quantify these findings, we utilize the Pearson correlation coefficient, which characterizes the linearity between two arrays. A value of -1 implies a precise negative linear relationship, a value of $+1$ implies a precise positive linear relationship, and a value of 0 implies no correlation. We use the `scipy` Pearson correlation coefficient function to calculate the coefficient for each of the correlations detailed in this chapter. Our results are shown in Table 5.5.

Parameter	Pearson Correlation Coefficient
log R'_{HK}	$+0.61$
F_{EUV}	$+0.42$
Stellar Age	-0.37
$v \sin i$	-0.01
[Fe/H]	-0.04
Semimajor Axis	$+0.44$
log g_p	$+0.11$

Table 5.5: Calculated Pearson correlation coefficient between δ_{R_P}/H_{eq} and the above parameters. As expected from Figures 5.2–5.9, δ_{R_P}/H_{eq} has the strongest linear relationship with log R'_{HK}.

As predicted by our visual inspection of these trends, the correlation coefficient for log R'_{HK} ($+0.61$) is the largest in magnitude. This further supports our assertion that log R'_{HK} has a stronger linear relationship with δ_{R_P}/H_{eq} than any other parameter. The coefficient for EUV flux ($+0.42$) is positive but smaller in magnitude than that for log R'_{HK}. Surprisingly, the value for semimajor axis ($+0.44$) is positive, but we would expect helium absorption to decrease with increasing

distance from the host star. This may be attributable to the fact that we did not delineate by spectral type when calculating the coefficient for semimajor axis. The coefficient for stellar age is -0.37, hinting at a weak but negative correlation. Finally, the correlation coefficients for the other parameters ($v \sin i$, [Fe/H], and $\log g_P$) are the smallest in magnitude and do not indicate any correlations with helium absorption.

It is important to note that this technique provides a quick check on our intuition, but there may be more robust metrics to measure the relationship between these parameters. We are assuming a linear correlation for this test, but this might not necessarily be the case. Other statistical tests should be applied in the future as the sample size of helium literature continues to grow.

Because $\log R'_{\mathrm{HK}}$ appears correlated with helium absorption, this supports the notion that stellar activity is the ultimate driver. However, the fact that we do not find a strong correlation with EUV flux raises come confusion. Fossati et al. (2022) also acknowledges a lack of correlation between high-energy radiation and helium absorption, while most other helium papers do claim a positive trend (e.g., Nortmann et al. 2018; Poppenhaeger 2022). This signifies that either there is too much inhomogeneity across methodologies to accurately compare between them, or that helium absorption is not correlated as closely with EUV flux as has been previously presumed. As discussed in Section 5.3, there are discrepancies between how helium absorption is measured and how it is normalized. There are also a myriad of techniques for predicting EUV flux (see Section 5.4), which introduces further uncertainty. To clarify whether the problem resides in disparate methodologies across papers or in a broader misconception of the physics of metastable helium signatures, we must standardize protocols in the future when comparing across the literature.

Chapter 6

Conclusion and Future Prospects

6.1   Non-detection of Helium in WASP-48b: A Summary

In this thesis, we examine whether there is any ongoing atmospheric escape in the extended atmosphere of WASP-48b, a hot Jupiter orbiting a slightly evolved, rapidly rotating F-type star. Close-in exoplanets are known to experience high rates of high-energy radiation, and this may be enough to drive atmospheric escape and mass loss. This is important because mass loss may be a contributor to planetary evolution and explain the radius gap seen in comparative exoplanetology studies. In addition, understanding the conditions under which a planet can maintain its atmosphere is important for building our galactic understanding of habitability.

We used high-resolution ground-based transmission spectroscopy to examine the 10833 Å helium triplet, a marker of atmospheric escape which resides in the near-infrared region of the spectrum. Observations were taken in May and June of 2019 using the Habitable Zone Planet Finder on the Hobby-Eberly Telescope in Texas. Thirty-four exposures were taken over this time period, and four were discarded for the purposes of this study. We build a transmission spectrum by creating a master out-of-transit spectrum, dividing each in-transit spectrum by

this master spectrum, and applying a weighted sum to the resulting spectra based on their inverse variances. The resulting transmission spectrum we find is "flat", meaning there is no difference between the in-transit and out-of-transit data. In other words, no planetary helium appears to be present in the extended atmosphere of WASP-48b. We use our transmission spectrum to calculate a maximum possible value for helium absorption, and we use an empirical Monte Carlo test to validate our results.

We compare our findings with the Oklopčić model, which predicts planetary helium absorption based on the stellar EUV spectrum, planet mass, radius, atmospheric composition, thermosphere temperature, and mass-loss rate. Given the range of parameters for WASP-48b, the Oklopčić model does not predict a large helium absorption in most cases, consistent with our findings. Because thermosphere temperature and mass-loss rate are poorly constrained in most exoplanets, we model our findings against a range of these parameters and find that our non-detection can be explain by a low thermosphere temperature or low mass-loss rate. However, there is still a large amount of degeneracy across these parameters.

Our non-detection of planetary helium in WASP-48b can be explained through low levels of EUV radiation, low helium abundances, or stellar winds (and other sources of stellar variability). Given that the the Oklopčić model predicts a small to nonexistent helium absorption feature, there is no reason to presume that our estimate of solar abundances (a 9:1 hydrogen-to-helium ratio) is inaccurate. Stellar winds could induce a variable helium feature, but are unlikely to suppress it entirely (Zhang et al. 2021). This leads us to conclude that our non-detection is most likely due to low levels of atmospheric escape. This makes sense in light of the fact that WASP-48b orbits an old star, and we know high-energy radiation decreases with stellar age.

6.2 Current State of Detections

To understand this non-detection to the fullest extent, we compare our findings to all other published helium works. We follow Nortmann et al. (2018) and normalize helium absorption to the planetary atmospheric scale height, H_{eq}. We then plot these values against a variety of parameters for almost all of the published helium detections and non-detections to date. These parameters include metrics associated with high-energy radiation (the log R'_{HK} value, EUV flux, stellar age, rotation rate, and metallicity) as well as planetary parameters that impact atmospheric escape (semimajor axis and surface gravity). We find that the log R'_{HK} value shows the strongest correlation with helium absorption. There does appear to be a slight positive trend with EUV flux, but there are still many outliers in the data. In addition, there is too much scatter across all the other parameters for any trends to be revealed, further complicating the picture.

Several factors could explain the lack of a strong correlation between helium absorption and EUV flux. It could be due to improper measurements of either parameter. Normalizing helium absorption to the scale height, for example, could be inappropriate because the scale height is derived from the planet's equilibrium temperature, which may not scale with the temperature of the thermosphere. On the other hand, the predicted EUV values we have used in this thesis (based on Poppenhaeger 2022) may also not be accurate. Finding ways to more accurately model stellar EUV emission, or even building a telescope or facility to directly measure it, will be critical moving forward.

Oklopčić (2019) predicts that close-in planets orbiting K stars are the most likely to experience high levels of atmospheric escape and provide the most promising candidates for helium absorption. While there has certainly been the largest

number of detections around K-type stars, there have also been detections around other spectral types (F, G, M, and T Tauri stars) as well as several non-detections around K-type stars. More investigations of planets around a variety of stellar types need to be done to observationally validate the claim that K-type stars are optimal for helium detections.

6.3   Recommendations for future observations

Studies of atmospheric escape have come a long way in the last decade. In addition to Ly-α and Hα studies, metastable helium has become another standard indicator that a planet is experiencing atmospheric escape. As more planets are investigated and comparative studies expand, the goal of the exoplanet atmospheric research community is to fully understand the timeline of atmospheric escape, the stellar and planetary environment in which it occurs, and its impact on atmospheric evolution and habitability over a planet's lifetime. To reach these goals, more factors need to be considered than have been in the last decade or so.

First and foremost, we should couple helium observations with Ly-α and/or Hα studies to corroborate findings when possible. This has been done for some planets, including HD 189773 (Vidal-Madjar et al. 2003; Salz et al. 2018), 55 Cnc e (Ehrenreich et al. 2012; Zhang et al. 2021), and GJ 9827b and d Carleo et al. (2021), but setting this as standard practice will strengthen our ability to quantify atmospheric escape.

Another corroboration technique should be to include multiple transits in analyses, because it has become increasingly apparent that stellar variability plays a meaningful role in fluctuating mass loss and helium absorption over short timescales. HD 189733b has been shown to exhibit XUV variability of up to 33%

(Zhang et al. 2022a), which greatly impacts the amount of helium absorption that is detected. Without measuring helium absorption across multiple nights, we run the risk of greatly overestimating or underestimating the fundamental mass loss estimate, which could adversely affect our understanding of how mass loss impacts planetary evolution.

Besides improving our observational practices, we should expand our modeling techniques for predicting helium absorption in order to corroborate theoretical predictions. This has already started in recent works: for example, Zhang et al. (2021) use three different models to compare with their observations. In addition to the 1D Parker wind model developed by Oklopčić & Hirata (2018), which we use in this work, 2.5D and 3D models have been developed (Wang & Dai 2018; Khodachenko et al. 2019). These models have been applied to Ly-α studies and are starting to be applied to helium searches as well.

Finally, we must address the elephant in the room, which is the problem of estimating stellar EUV flux. We must work toward developing a standard for predicting high-energy stellar radiation, instead of the menagerie of techniques that are currently in use. While multiple approaches are of course useful, many of these approaches provide contradictory findings. We must find reliable methods that accurately predict stellar EUV flux. Funding a mission to directly observe EUV emission from other stars would be an incontrovertible way to validate these various models for nearby exoplanets. However, such a mission would only be able to observe stars within about 50 pc due to EUV absorption by the ISM (e.g., Vidal-Madjar et al. 2003), so we would not directly be able to measure stellar EUV flux for all the stars in our sample. However, it would provide additional constraints on current EUV models, which could then be applied to stars farther than 50 pc.

In the meantime, understanding the precise nature of the relationship between EUV flux and helium absorption should continue to be investigated. We should continue to search for analytical scaling relations with factors such as age (Sanz-Forcada et al. 2011), log R'_{HK} (Sreejith et al. 2020), and X-ray emission (Poppenhaeger 2022). If the assertion by Poppenhaeger (2022) that iron abundances hold insight into the stellar coronal activity and are related to helium absorption is indeed accurate, we can employ X-ray spectroscopy to directly measure iron abundances in exoplanet host stars to determine likely candidates for atmospheric escape studies.

Many of these suggestions hold true for WASP-48b. While multiple transits were observed, no other atmospheric escape studies have been conducted for the planet. We are unable to examine Lyα absorption in this case, due to the star's distance (WASP-48 is ~ 460 pc away), but we could corroborate our helium non-detection with an Hα investigation. This would strengthen our assertion that there is little-to-no ongoing atmospheric escape. We should also employ multiple models to help further constrain the mass loss rate and understand how much total mass loss the planet has experienced over its lifetime. Obtaining X-ray data could further enhance our understanding of activity in the corona of WASP-48. At this time, a helium non-detection in a hot Jupiter orbiting an old, slightly evolved F-type star makes sense in light of our current understanding and models.

We must continue to push toward more rigorous observations and models to complete the picture of how atmospheric escape in close-in exoplanets drives planetary evolution. This is just one small piece of the exoplanet characterization puzzle, but it will bring us closer to understanding the architecture and habitability of planetary systems within our Galaxy.

Bibliography

Agol, E., et al. 2021, PSJ, 2, 1

Allart, R., et al. 2019, A&A, 623, A58

—. 2018, Science, 362

Alonso-Floriano, F. J., et al. 2019, A&A, 629, A110

Amard, L., & Matt, S. P. 2020, ApJ, 889, 108

Anderson, D. R., et al. 2014, MNRAS, 445, 1114

—. 2017, A&A, 604, A110

Bailes, M., Lyne, A. G., & Shemar, S. L. 1991, Nature, 352, 311

Bakos, G. Á., et al. 2010, ApJ, 710, 1724

Barnes, J. R., Haswell, C. A., Staab, D., & Anglada-Escudé, G. 2016, MNRAS, 462, 1012

Barragán, O., et al. 2022, MNRAS

Barstow, J. K., Aigrain, S., Irwin, P. G. J., & Sing, D. K. 2017, ApJ, 834, 50

Bevington, P. R., & Robinson, D. K. 1969, Data Reduction and Error Analysis for the Physical Sciences

Bonfils, X., et al. 2012, A&A, 546, A27

Bonomo, A. S., et al. 2017, A&A, 602, A107

Bouchy, F., et al. 2005, A&A, 444, L15

Bourrier, V., et al. 2017, AJ, 154, 121

—. 2018a, A&A, 619, A1

—. 2018b, Nature, 553, 477

Boyajian, T., et al. 2015, MNRAS, 447, 846

Brown, T. M. 2001, ApJ, 553, 1006

Bundy, K. A., & Marcy, G. W. 2000, PASP, 112, 1421

Burgasser, A. J., & Mamajek, E. E. 2017, ApJ, 845, 110

Burrows, A., & Lunine, J. 1995, Nature, 378, 333

Butler, R. P., Vogt, S. S., Marcy, G. W., Fischer, D. A., Wright, J. T., Henry,
    G. W., Laughlin, G., & Lissauer, J. J. 2004, ApJ, 617, 580

Campbell, B., Walker, G. A. H., & Yang, S. 1988, ApJ, 331, 902

Carleo, I., et al. 2021, AJ, 161, 136

Casasayas-Barris, N., et al. 2021a, A&A, 654, A163

—. 2021b, A&A, 647, A26

Cassan, A., et al. 2012, Nature, 481, 167–169

Cauley, P. W., Redfield, S., & Jensen, A. G. 2017, ApJ, 153, 217

Charbonneau, D., et al. 2009, Nature, 462, 891

Charbonneau, D., Brown, T. M., Latham, D. W., & Mayor, M. 2000, ApJ, 529,
    L45

Charbonneau, D., Brown, T. M., Noyes, R. W., & Gilliland, R. L. 2002, ApJ, 568, 377

Chromey, F. R. 2016, To Measure the Sky

Ciceri, S., et al. 2015, A&A, 577, A54

Cochran, W. D., Hatzes, A. P., Endl, M., Paulson, D. B., Walker, G. A. H., Campbell, B., & Yang, S. 2002, in AAS/Division for Planetary Sciences Meeting Abstracts, Vol. 34, AAS/Division for Planetary Sciences Meeting Abstracts #34, 42.02

Czesla, S., et al. 2022, A&A, 657, A6

David, T. J., Petigura, E. A., Luger, R., Foreman-Mackey, D., Livingston, J. H., Mamajek, E. E., & Hillenbrand, L. A. 2019, ApJ, 885, L12

Deeg, H. J., & Alonso, R. 2018, in Handbook of Exoplanets, ed. H. J. Deeg & J. A. Belmonte, 117

del Burgo, C., & Allende Prieto, C. 2016, MNRAS, 463, 1400

dos Santos, L. A., et al. 2020, A&A, 640, A29

Duvvuri, G. M., et al. 2021, ApJ, 913, 40

Eastman, J., Siverd, R., & Gaudi, B. S. 2010, PASP, 122, 935

Ehrenreich, D., et al. 2012, A&A, 547, A18

Ellis, T. G., Boyajian, T., von Braun, K., Ligi, R., Mourard, D., Dragomir, D., Schaefer, G. H., & Farrington, C. D. 2021, AJ, 162, 118

Enoch, B., et al. 2011, ApJ, 142, 86

Florian, & Gallet. 2020, arXiv e-prints, arXiv:2006.07880

Fossati, L., et al. 2022, A&A, 658, A136

Foster, G., Poppenhaeger, K., Ilic, N., & Schwope, A. 2021, arXiv e-prints, arXiv:2106.14550

France, K., et al. 2020, in Society of Photo-Optical Instrumentation Engineers (SPIE) Conference Series, Vol. 11444, Society of Photo-Optical Instrumentation Engineers (SPIE) Conference Series, 1144405

Fulton, B. J., Petigura, E. A., Blunt, S., & Sinukoff, E. 2018, PASP, 130, 044504

Gan, T., et al. 2022, arXiv e-prints, arXiv:2202.10024

Gasman, D., Min, M., & Chubb, K. L. 2022, A&A, 659, A114

Gatewood, G., & Eichhorn, H. 1973, AJ, 78, 769

Gaudi, B. S., et al. 2017, Nature, 546, 514

Gillon, M., et al. 2014, A&A, 563, A21

—. 2016, Nature, 533, 221

—. 2017, Nature, 542, 456

Girardi, L., Bertelli, G., Bressan, A., Chiosi, C., Groenewegen, M. A. T., Marigo, P., Salasnich, B., & Weiss, A. 2002, A&A, 391, 195

Guillot, T., Burrows, A., Hubbard, W. B., Lunine, J. I., & Saumon, D. 1996, ApJ, 459, L35

Guo, X., et al. 2020, AJ, 159, 239

Harpsøe, K. B. W., et al. 2013, A&A, 549, A10

Hartman, J. D., et al. 2011a, ApJ, 726, 52

—. 2011b, ApJ, 742, 59

Hebb, L., et al. 2009, ApJ, 693, 1920

Hébrard, G., et al. 2013, A&A, 549, A134

Hershey, J. L. 1973, AJ, 78, 421

Horne, K. 1986, PASP, 98, 609

Howard, A. W., et al. 2011, ApJ, 730, 10

Hubbard, W. B., Fortney, J. J., Lunine, J. I., Burrows, A., Sudarsky, D., & Pinto, P. 2001, ApJ, 560, 413

Hubbard, W. B., Hattori, M. F., Burrows, A., Hubeny, I., & Sudarsky, D. 2007, Icarus, 187, 358

Husser, T. O., Wende-von Berg, S., Dreizler, S., Homeier, D., Reiners, A., Barman, T., & Hauschildt, P. H. 2013, A&A, 553, A6

Jacob, W. S. 1855, MNRAS, 15, 228

Jensen, A. G., Redfield, S., Endl, M., Cochran, W. D., Koesterke, L., & Barman, T. 2012, ApJ, 751:86

Jensen, E. 2013, Astrophysics Source Code Library, ascl:1306.007

Kanodia, S., et al. 2022, arXiv e-prints, arXiv:2203.07178

Kanodia, S., & Wright, J. 2018, RNAAS, 2, 4

Kaplan, K. F., Bender, C. F., Terrien, R. C., Ninan, J., & Roy, A. 2019, in ASP Conference Series, Vol. 523, Astronomical Data Analysis Software and Systems XXVIII, ed. P. J. Teuben, M. W. Pound, B. A. Thomas, & E. M. Warner, 567

Karoff, C., et al. 2018, ApJ, 852, 46

Kasper, D., Bean, J. L., Oklopčić, A., Malsky, I., Kempton, E. M. R., Désert, J., A., R. L., & Mansfield, M. 2020, ApJ, 160, 258

Kausch, W., et al. 2014, in ASP Conference Series, Vol. 485, Astronomical Data Analysis Software and Systems XXIII, ed. N. Manset & P. Forshay, 403

Kawauchi, K., et al. 2022, arXiv e-prints, arXiv:2202.10182

Khodachenko, M. L., Shaikhislamov, I. F., Lammer, H., Berezutsky, A. G., Miroshnichenko, I. B., Rumenskikh, M. S., Kislyakova, K. G., & Dwivedi, N. K. 2019, ApJ, 885, 67

Kiefer, F. 2019, A&A, 632, L9

Kirk, J., Alam, M. K., López-Morales, M., & Zeng, L. 2020, AJ, 159, 115

Knutson, H. A., Howard, A. W., & Isaacson, H. 2010, ApJ, 720, 1569

Kosiarek, M. R., et al. 2019, AJ, 157, 97

Kreidberg, L. 2015, PASP, 127, 1161

Kriedberg, L., & Oklopčić, A. 2018, RNAAS, 2, 44

Krishnamurthy, V., et al. 2021, AJ, 162, 82

Kulow, J. R., France, K., Linsky, J., & Loyd, R. O. P. 2014, ApJ, 786, 132

Lalitha, S., Poppenhaeger, K., Singh, K. P., Czesla, S., & Schmitt, J. H. M. M. 2014, ApJ, 790, L11

Lam, K. W. F., et al. 2017, A&A, 599, A3

Lamers, H. J. G. L. M., & Cassinelli, J. P. 1999, Introduction to Stellar Winds

Lanotte, A. A., et al. 2014, A&A, 572, A73

Latham, D. W., Mazeh, T., Stefanik, R. P., Mayor, M., & Burki, G. 1989, Nature, 339, 38

LeBlanc, F. 2010, An Introduction to Stellar Astrophysics

Lecavelier Des Etangs, A. 2007, A&A, 461, 1185

Lecavelier des Etangs, A., et al. 2012, A&A, 543, L4

Linsky, J. L., Fontenla, J., & France, K. 2014, ApJ, 780, 61

Lissauer, J. J., & de Pater, I. 2013, Fundamental Planetary Science

Lopez, E. D., & Fortney, J. J. 2013, ApJ, 776, 2

Lovis, C., & Fischer, D. 2010, in Exoplanets, ed. S. Seager, 27–53

Lyne, A. G., & Bailes, M. 1992, Nature, 355, 213

MacLeod, M., & Oklopčić, A. 2021

Madhusudhan, N., & Redfield, S. 2015, International Journal of Astrobiology, 14, 177

Mahadevan, S., et al. 2012, Proc. SPIE, 8446, 84461S

—. 2014, Proc. SPIE, 9147, 91471G

Mann, A. W., et al. 2020, AJ, 160, 179

Mayor, M., & Queloz, D. 1995, Nature, 378, 355

Mazeh, T., Holczer, T., & Faigler, S. 2016, A&A, 589, A75

Melo, C., Santos, N. C., Pont, F., Guillot, T., Israelian, G., Mayor, M., Queloz, D., & Udry, S. 2006, A&A, 460, 251

Metcalf, A. J., et al. 2019, Optica, 6, 233

Miller, M. C., & Hamilton, D. P. 2001, ApJ, 550, 863

Morton, D. C. 1991, ApJS, 77, 119

Moulton, F. R. 1899, AJ, 20, 33

Moutou, C., Coustenis, A., Schneider, J., St Gilles, R., Mayor, M., Queloz, D., & Kaufer, A. 2001, A&A, 371, 260

Murgas, F., Pallé, E., Parviainen, H., Chen, G., Nortmann, L., Nowak, G., Cabrera-Lavers, A., & Iro, N. 2017, A&A, 605, A114

Ninan, J., et al. 2018, Proc. SPIE, 10709, 107092U

Ninan, J. P., et al. 2020, ApJ, 894, 97

Niraula, P., et al. 2017, AJ, 154, 266

Nortmann, L., et al. 2018, Science, 362, 1388

Noyes, R. W., Hartmann, L. W., Baliunas, S. L., Duncan, D. K., & Vaughan, A. H. 1984, ApJ, 279, 763

Oklopčić, A. 2019, ApJ, 881, 133

Oklopčić, A., & Hirata, C. M. 2018, ApJ, 855, L11

Oklopčić, A., Silva, M., Montero-Camacho, P., & Hirata, C. M. 2020, ApJ, 890, 88

Orell-Miquel, J., et al. 2022, arXiv e-prints, arXiv:2201.11120

O'Rourke, J. G., et al. 2014, ApJ, 781, 109

Osterbrock, D. E., & Ferland, G. J. 2006, Astrophysics of gaseous nebulae and active galactic nuclei

Owen, J. E. 2019, Annual Review of Earth and Planetary Sciences, 47, 67

Owen, J. E., & Lai, D. 2018, MNRAS, 479, 5012

Owen, J. E., & Wu, Y. 2013, ApJ, 775, 105

Palle, E., et al. 2020, A&A, 638, A61

Paragas, K., et al. 2021, ApJ, 909, L10

Parker, E. N. 1958, ApJ, 128, 664

Piaulet, C., et al. 2021, AJ, 161, 70

Poppenhaeger, K. 2022, arXiv e-prints, arXiv:2202.08838

Prieto-Arranz, J., et al. 2018, A&A, 618, A116

Prölss, G. W., & Bird, M. K. 2004, Physics of the Earth's Space Environment: an introduction

Queloz, D., et al. 2000, A&A, 354, 99

Rauer, H., Bockelée-Morvan, D., Coustenis, A., Guillot, T., & Schneider, J. 2000, A&A, 355, 573

Redfield, S., Endl, M., Cochran, W. D., & Koesterke, L. 2008, ApJ, 283, L87–L90

Reuyl, D., & Holmberg, E. 1943, ApJ, 97, 41

Ribas, I., Guinan, E. F., Güdel, M., & Audard, M. 2005, ApJ, 622, 680

Rice, K., et al. 2019, MNRAS, 484, 3731

Rodriguez, J. E., Vanderburg, A., Eastman, J. D., Mann, A. W., Crossfield, I. J. M., Ciardi, D. R., Latham, D. W., & Quinn, S. N. 2018, AJ, 155, 72

Rogers, L. A., & Seager, S. 2010, ApJ, 716, 1208

Rousselot, P., Lidman, C., Cuby, J. G., Moreels, G., & Monnet, G. 2000, A&A, 354, 1134–1150

Sada, P. V., et al. 2012, PASP, 124, 212–229

Salz, M., et al. 2018, A&A, 620

Salz, M., Czesla, S., Schneider, P. C., & Schmitt, J. H. M. M. 2016, A&A, 586, A75

Salz, M., Schneider, P. C., Czesla, S., & Schmitt, J. H. M. M. 2015, A&A, 576, A42

Santos, N. C., Israelian, G., & Mayor, M. 2004, A&A, 415, 1153

Sanz-Forcada, J., Micela, G., Ribas, I., Pollock, A. M. T., Eiroa, C., Velasco, A., Solano, E., & García-Álvarez, D. 2011, A&A, 532, A6

Schneider, J. 1994, Ap&SS, 212, 321

Schroeder, D. V. 1999, An Introduction to Thermal Physics

Seager, S., & Deming, D. 2010, ARA&A, 48, 631

Seager, S., & Sasselov, D. D. 1998, ApJ, 502, L157

—. 2000, ApJ, 537, 916

Seager, S., Whitney, B. A., & Sasselov, D. D. 2000, ApJ, 540, 504

Southworth, J. 2010, MNRAS, 408, 1689

Spake, J. J., Oklopčić, A., & Hillenbrand, L. 2021, A&A

Spake, J. J., et al. 2018, Nature, 557, 68

Sreejith, A. G., Fossati, L., Youngblood, A., France, K., & Ambily, S. 2020, A&A, 644, A67

Strand, K. A. 1943, PASP, 55, 29

Struve, O. 1952, The Observatory, 72, 199

Sutherland, I. E., & Hodgman, G. W. 1974, Communications of the ACM, 17, 1

Torres, G., Winn, J. N., & Holman, M. J. 2008, ApJ, 677, 1324

Triaud, A. H. M. J., et al. 2013, A&A, 551, A80

Triaud, A. H. M. J., et al. 2015, MNRAS, 450, 2279

Turner, J. D., et al. 2016, MNRAS, 459, 789–819

van de Kamp, P. 1963, AJ, 68, 515

van de Kamp, P., & Lippincott, S. L. 1951, AJ, 56, 49

Vidal-Madjar, A., Lecavelier des Etangs, A., Désert, J. M., Ballester, G. E., Ferlet, R., Hébrard, G., & Mayor, M. 2003, Nature, 422, 143

Vissapragada, S., Knutson, H. A., dos Santos, L. A., Wang, L., & Dai, F. 2022, arXiv e-prints, arXiv:2201.09889

Vissapragada, S., et al. 2020, AJ, 159, 278

—. 2021, AJ, 162, 222

von Braun, K., et al. 2011, ApJ, 740, 49

Wang, L., & Dai, F. 2018, ApJ, 860, 175

West, A. A., et al. 2004, AJ, 128, 426

West, R. G., et al. 2019, MNRAS, 486, 5094

—. 2016, A&A, 585, A126

Wheatley, P. J., Louden, T., Bourrier, V., Ehrenreich, D., & Gillon, M. 2017, MNRAS, 465, L74

Wolszczan, A., & Frail, D. A. 1992, Nature, 355, 145

Wright, J. T., & Eastman, J. D. 2014, PASP, 126

Wright, N. J., Drake, J. J., Mamajek, E. E., & Henry, G. W. 2011, ApJ, 743, 48

Yan, F., & Henning, T. 2018, Nature Astronomy, 2, 714

Yee, S. W., Petigura, E. A., & von Braun, K. 2017, ApJ, 836, 77

Youngblood, A., et al. 2017, ApJ, 843, 31

Zhang, M., Cauley, P. W., Knutson, H. A., France, K., Kreidberg, L., Oklopčić, A., Redfield, S., & Shkolnik, E. L. 2022a, arXiv e-prints, arXiv:2204.02985

Zhang, M., Knutson, H. A., Wang, L., Dai, F., & Barragán, O. 2022b, AJ, 163, 67

Zhang, M., et al. 2022c, AJ, 163, 68

Zhang, M., Knutson, H. A., Wang, L., Dai, F., Oklopcic, A., & Hu, R. 2021, AJ, 161, 181

Zhu, W., & Dong, S. 2021, ARA&A, 59

Zilinskas, M., Miguel, Y., Mollière, P., & Tsai, S.-M. 2020, MNRAS, 494, 1490